ISSN 1347-3212

# 「プラズマプロセス酸化物微粒子合成」に関する研究

# Study on Plasma Synthesis of Oxide Nano-Particles



2006

独立行政法人物質・材料研究機構

物質研究所研究報告書第12号

AML/NIMS Reports No.12

# 目　次

# Study on Plasma Synthesis of Oxide Nano-Particles

## Abstract

Plasma Processing Group started in April 2003 and has aimed to synthesize functional materials by controlling the chemical reaction field through highly controlled plasma technology. Based on the development of plasma generation methods and numerical analysis, we have worked on the functionalization of nano-structured ceramic materials, such as the plasma synthesis of nano-scale particles of titanium oxide and diamond, the development of zinc oxide UV emitting materials with the help of plasma hydrogen doping, and the synthesis of oxide thin films by a pulse-modulated sputtering method. This report summarizes the research activities conducted in the-three-years-research term from April 2003 to March 2006.

Fe- and Eu-doped $TiO_2$ nanocrystals were synthesized via $Ar/O_2$ thermal plasma oxidation of liquid precursor mists. The use of mists ensured atomic level mixing of the elements and high supersaturation of the evaporated species upon plasma oxidation, which favored nanocrystal formation upon condensation. High concentration of Fe-doping, up to atomic ratio of $R_{Fe/Ti}$ =0.2, was attained without any precipitation of other phases. In $Eu^{3+}$ doped $TiO_2$ nanocrystals, enhanced (visible with naked eyes) pure red emission was observed from the nanocrystallites. (Chapter 2)

Pulse-modulated RF induction thermal plasma, which was developed in our group, was numerically characterized under transient nonequilibrium conditions. The results showed that the effects of changes in input power on the thermal nonequilibrium and the ionization nonequilibrium are most noticeable at the early stages of pulse on and off. (Chapter 3)

Growth of crystallized $TiO_2$ films on unheated plastic substrates was realized by originally developed dual magnetron sputtering apparatus. This thin film growth method drastically reduced the crystallization temperature of $TiO_2$ films. The low temperature crystallization of $TiO_2$ realized photo catalytic films on plastic substrates. (Chapter 4)

Nanocrystalline diamond particles with 200–500 nm in diameter have been prepared in a 13.56 MHz low pressure inductively coupled $CH_4/CO/H_2$ plasma. Electron energy loss spectroscopy revealed that $sp^2$-bonded carbons are identified around the 20–50 nm subgrains of nanocrystalline diamond particles. (Chapter 5)

An artificial graphite powder, mesocarbon microbeads (MCMB), powder, was treated in reactive thermal plasma atmospheres. The plasma-treatment led to the improvement of charge/discharge characteristics as anode of lithium-ion rechargeable battery. (Chapter 6)

Titanium trichloride solution, which is not moisture sensitive and easily manipulatable, was used as a staring material for $TiO_2$ preparation. Phase pure anatase, brookite, and rutile nanocrystallites were obtained under mild hydrothermal conditions. (Chapter 7)

Plasma Processing Group;
Takamasa ISHIGAKI, Masayuki KAMEI, Katsuyuki OKADA and Ji-Guang LI
National Institute for Materials Science, Advanced Materials Laboratory
1-1 Namiki, Tsukuba, Ibaraki 305-0044, Japan
Correspondence to: ISHIGAKI.Takamasa@nims.go.jp
TEL: +81-29-860-4659
FAX: +81-29-860-4701
URL: http://www.nims.go.jp/plasma/

# 第１章　研究概要および構成

## １．１　はじめに

本報告書は、独立行政法人物質・材料研究機構物質研究所のプラズマプロセスグループが「プラズマプロセス酸化物微粒子合成」を研究課題として、平成15年度から17年度まで３年間で行った研究の概要である。

平成15年４月に、新しくスタートしたプラズマプロセスグループは、材料合成プロセスの進行する化学反応場をプラズマにより精密に制御して新材料の創製をめざしてきた。独自のプラズマ発生法の開発を通してセラミックス材料の高機能化を進め、欠陥構造、サイズ、構成相を制御した酸化チタン、ナノクリスタルダイヤモンド等ナノサイズ粒子のプラズマ合成、パルス変調高周波熱プラズマ処理による酸化亜鉛発光材料の開発、パルス化スパッタリング法酸化物薄膜の合成を行った。プラズマ中の気相励起状態を積極的に利用して、通常環境下では合成困難な化学組成、形態をもった酸化チタン等酸化物セラミックスナノ粒子を合成してきた。さらに、ナノ構造体のサイズ、結晶構造、欠陥構造を高度に制御することにより、新しい応用分野を探索することを目的として研究をすすめた。

## １．２　研究概要

物質の材料化をすすめるためのブレークスルーとして、ナノメートルオーダーの材料組織制御の必要性が叫ばれている。プラズマ利用プロセスは、他の方法にない材料プロセッシングに重要な特徴を有しているので、合成プロセスが進行する化学反応場の制御性を高めることにより、ナノ構造が制御された材料創製が可能である。当グループでは、プラズマプロセッシングの高度化により、光機能など高機能性を有するナノサイズの高結晶性粒子合成をめざした。

新しいプラズマプロセッシングの特徴付け、反応装置設計へのフィードバックをおこない、酸化亜鉛、酸化チタン等のａナノクリスタル合成、ｂナノクリスタルの機能化、ｃ高機能ナノクリスタルの利用に不可欠な粒子修飾技術を開発した。

熱プラズマ利用プロセスは、材料プロセッシングに重要な特徴を有している。合成プロセスが進行する反応場の制御性を高めることにより、形態、結晶構造、化学組成において従来にない材料創製が可能である。第２章では、酸化チタンのナノ粒子合成を取り上げ、窒素、鉄、希土類元素のドーピングを試み、非平衡化学組成をもつ、高結晶性酸化チタンナノ粒子の一段プロセス合成を示した。また、第３章では、NIMSで世界に先駆け開発したプラズマ発生法、パルス変調RFプラズマの大きな特徴である非平衡性を、時間依存数値解析法、時間分解発光分光法によりしらべた結果を報告する。

第４章では、デュアルマグネトロンスパッタ法を用いて二酸化チタンの高結晶性薄膜の成膜プロセス温度の低温化をめざした。パルススパッタリング技術を独自の技術で高度化し、プラスチック等の耐熱温度の低い基体上に結晶化した酸化物機能薄膜を形成した。

第５章では、プロセシングプラズマの一つとして有望な低圧ICPよるナノクリスタルダイヤモンドの合成と構造評価を中心に述べる。

第６章では、第２章、３章で用いたのと同じ高周波熱プラズマにより、人造黒鉛末を処理して表面ナノ構造、化学組成を変化させた。プラズマ処理粉末をリチウムイオン電池の負極に応用して、充放電容量、初期充放電効率の向上を示した。

第７章では、プラズマプロセス以外での酸化チタンナノ粒子の相選択合成について報告する。マイルドな水熱合成反応により、純粋なルチル、ブルッカイト、アナターゼナノ粒子の選択合成条件を最適化した。

## １．３　研究グループの構成員

アソシエートディレクター

石垣隆正（平成15年４月～18年３月）

主幹研究員

亀井雅之（平成15年４月～18年３月）

主任研究員→主幹研究員

岡田勝行（平成15年４月～18年３月、

平成16年4月昇格）

研究員→主任研究員

李　継光（平成15年4月～18年3月、
平成17年4月昇格）

客員研究員

吉田豊信（平成15年4月～18年3月）

渡辺隆行（平成15年4月～18年3月）

守吉佑介（平成17年4月～18年3月）

ＪＳＰＳフェロー

Jiayang XU（平成15年4月～16年3月）

Rubin YE（平成15年4月～17年3月）

特別研究員

Seung-Min OH（平成15年4月～7月）

王　暁輝（平成15年8月～17年3月）

田中秀樹（平成16年4月）

Rubin YE（平成17年4月～18年3月）

佐藤仁俊（平成17年4月～18年3月）

外来研究員

田中秀樹（平成15年4月～16年3月）

見矢木崇平（平成15年4月～16年3月、
平成16年8月～17年3月）

田口広之（平成15年4月～17年3月）

神山弘志（平成15年4月～17年3月）

広瀬康一（平成15年4月～16年3月）

瀬戸山誠（平成15年4月～16年4月）

松村功徳（平成15年8月～18年3月）

Hubert LANGE（平成15年10～11月、
平成16年5～6月）

林和幸（平成15年11月～16年10月）

勝部篤（平成16年4月～17年3月）

小林法夫（平成16年4月～18年3月）

椎野修（平成17年3月～18年3月）

岩淵芳典（平成17年3月～18年3月）

吉川雅人（平成17年3月～18年3月）

池田征史（平成17年4月～18年3月）

川上裕二（平成17年4月～18年3月）

鎌田啓嗣（平成17年4月～18年3月）

村上貴章（平成17年4月～18年3月）

東良（平成17年5月～8月）

松井和彦（平成17年5月～8月）

鈴木了（平成17年8月～12月）

小井土由将（平成17年8月～12月）

Robert BÜCHEL（平成17年11月～18年3月）

飯島志行（平成17年11月～18年3月）

## 1．4　プラズマプロセス研究会

第1回　平成15年10月6日

**テーマ「熱プラズマを利用した
カーボンナノチューブ合成」**

Gervais SOUCY
（Univ. of Sherbrooke, Dept. of Chem. Eng.）

Hubert LANGE
（Warsaw Univ., Dept. Of Chem.）

第2回　平成16年6月10日

**テーマ「熱プラズマの計測・評価」**

Hubert LANGE
（Warsaw Univ., Dept. Of Chem.）

第3回　平成17年8月26日

**テーマ「熱プラズマの数値解析」**

渡辺隆行
（東京工業大学大学院原子核工学専攻）

第4回　平成18年3月29日

**テーマ「熱プラズマプロセシングの将来展望」**

吉田豊信
（東京大学大学院マテリアル工学専攻）

守吉佑介
（法政大学工学部物質化学科）

## 1．5　執筆担当

本報告書はプラズマプロセスグループ構成員が分担して執筆した。各担当区分を以下に示す。

第1章　石垣隆正

第2章　2．1　石垣隆正、2．2　李継光

第3章　3．1　石垣隆正、3．2　Rubin YE

第4章　亀井雅之

第5章　岡田勝行

第6章　石垣隆正

第7章　李継光

第8章　石垣隆正

## 1．6　謝辞

本研究は所内はじめ国内外多くの共同研究者の寄与により達成されたもので、深く感謝します。

# 第２章　高周波熱プラズマプロセスを利用したナノ粒子合成

## ２．１　反応性熱プラズマプロセスによるセラミックス材料の創製

熱プラズマ利用プロセスは、材料プロセッシングに重要な特徴を有しているので、合成プロセスが進行する反応場の制御性を高めることにより、形態、結晶構造、化学組成において従来にない材料創製が可能である[1)-4)]。著者らが開発してきた材料プロセスでは、高温熱源として利用されてきた熱プラズマから Chemistry を抽出して材料プロセスに利用することを主眼とした。

アーク放電プラズマ（通常熱プラズマと呼ばれる）の材料合成反応場としての特徴をあげると、次のようになる[5)]。①１万～１万５千度の超高温をもつ。大気圧近くの比較的高い圧力で発生するのでプラズマ密度が高く、軽い電子だけでなく、原子や分子など重い粒子温度も高く、平衡プラズマとみなすことができる（局所熱平衡状態）。②高濃度のラジカルなど活性化学種が含まれ、化学的反応性が高い。③プラズマ流が高温領域（電力供給領域）から離れるとき、その尾炎部で $10^{5\text{-}7}$ K/s で超急冷される。

熱プラズマの代表的な発生法としては直流アーク放電を発生するプラズマトーチと高周波（RF）による誘導熱プラズマがあげられる。RF 熱プラズマは、さらに、次のように材料プロセスに有利な特徴を有する。④ RF コイルを通して周波数・数 MHz、入力・数十 kW の高周波を供給すると、直径 30 ～ 50mm のプラズマ発生が可能であり、超高温領域の体積が大きい。⑤ RF 熱プラズマ中の軸方向の流速は数 m/s 以下低い。したがって、高温領域の滞留時間は 10 ～ 20ms であり、化学プロセスの進行に十分な長さをもっている。⑥ RF 熱プラズマ法は無電極放電法であるので、酸化、還元、反応性といった各種雰囲気のプラズマが発生でき、特異な化学反応場を提供する。

高周波熱プラズマ発生の様子を Fig.2.1 に示す。水冷構造２重水冷管のまわりに電力供給用の高周波コイルが巻かれている。紡錘形の明るい部分が熱プラズマの高温部分でその中に上部から原料供給プローブが挿入されている。ここでは粉末を供給しており、紡錘形下部に高温下にある粉末表面からの光放射が見える。

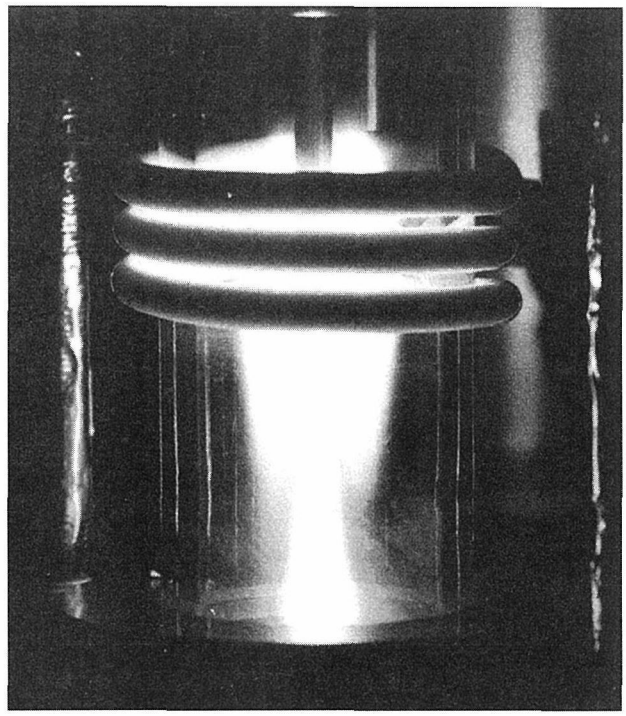

Fig.2.1 Generation of RF induction thermal plasma.

熱プラズマは非常に大きな熱量を提供する高温熱源であるので、Fig.2.2 に示したように、3,070℃という高融点をもつチタンカーバイドでもプラズマ中に供給すると瞬時に溶融して球状化される[6)]。数十 mm の大きさをもった不規則形状粒子を球状

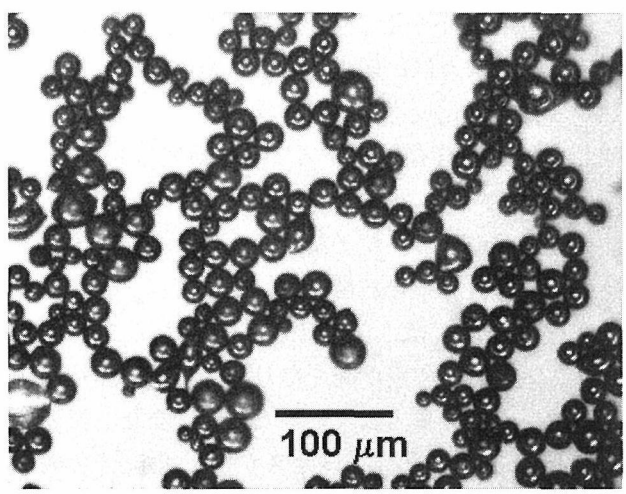


Fig.2.2 Spherical refractory TiC particles obtained through melting and spheroidization in RF induction thermal plasma.

化するプロセスは工業的に広く使われており、たとえば、１時間に30kg、すなわち１週間に１トンの高融点タングステン粉末の球状化が可能である[7]。すなわち、熱プラズマ材料プロセスは工業的に利用可能な素地を有しており、後で述べる高機能ナノ粒子合成も、その有効性さえ示すことができれば、短時間に工業的な利用に結びつくことが期待される。

伝統的な顔料としての用途に加え、光触媒、太陽電池、ガスセンサー、バイオセンサーなど新しい分野に応用されている。光触媒の分野では、窒素、遷移金属ドープ酸化チタンにおいて可視光応答性が発現することから、屋内環境への用途拡大等、光触媒の更なる高機能化への期待が高まっている。遷移金属ドープ酸化チタンは、近年、磁性半導体として利用する期待も高まっている。

物質の材料化をすすめるためのブレークスルーとして、その一つの形態がナノ粒子であるが、ナノ粒子の特性が必ずしも有効に引き出されていないのが現状である。著者らは、酸化物ナノ粒子の特性を有効に引き出すために、高度制御プラズマプロセスを用いて高結晶化、表面制御、非平衡組成導入、原子オーダーでの均質性をめざしている。セラミックス材料のナノ粒子合成は、従来、主として溶液プロセスを中心として進められてきた。発光特性を例にとると、溶液合成酸化物ナノ粒子の機能化を妨げていた大きな理由として、低結晶性、表面に結合した水酸基による消光、不完全な組成制御（ドーピング濃度、表面偏析）などがあげられる。

高周波誘導熱プラズマは、材料合成反応場としての高いポテンシャルを有しており、ナノ粒子の合成と任意元素のドーピングを一段階で行うことも可能である。我々は、炭化チタン、窒化チタン粉末の熱プラズマ酸化反応により、酸化チタン微粒子を合成した。酸素含有熱プラズマ中で粒径30-40μmの粒子は溶融する。溶融と同時に、発熱反応である酸化反応が進行し、粒子温度は上昇し、高濃度の蒸発種をプラズマ中に放散する。従って、この固体プリカーサー法では、気体原料を用いたときと比較して、気相過飽和度が高くなり、合成粒子の粒径がミクロン～ナノまで広くとれる[8)-14)]。また、気相からの凝縮とその急冷プロセスか続く微粒子合成では準安定相アナターゼが選択する[15)]。これに対し、プラズマ雰囲気の酸素圧を下げるとルチル相ナノ粒子が選択的に生成することを示した[12),14)]。また、窒化チタン粉末から合成した酸化チタンナノ粒子中には窒素がドープされ、可視光下での光触媒活性を示した[13]。

## References


1) 石垣隆正, *プラズマ・核融合学会誌*, **77**, 1088(2001).
2) 石垣隆正, 高温学会誌, **28**, 98(2002).
3) 石垣隆正, 大橋直樹, 羽田肇, 作田忠裕, *材料の科学と工学*, **40**, 2(2003).
4) 石垣隆正, 大橋直樹, *"反応場制御による新しい材料プロセッシング"*, 北澤宏一監修,, p.p.13-33, アイピーシー, (2004).
5) M.I. Boulos, P. Fauchais and E. Pfender *Thermal plasma: Fundamentals and Applications* Vol. 1, New York: Plenum Press, (1994)
6) Y.-L. Li and T. Ishigaki, *J. Am. Ceram. Soc.*, **84**, 1929 (2001).
7) Home page of TEKNA Plasma Systems Inc., Sherbrooke, Quebec, Canada, /www.tekna.com/.
8) Y.-L. Li and T. Ishigaki, *Chem. Mater.*, **13**, 1577 (2001).
9) Y.-L. Li and T. Ishigaki, *Chem. Phys. Lett.*, **367**, 561(2003).
10) T. Ishigaki, Y.-L. Li and E. Kataoka, *J. Am. Ceram. Soc.*, **86**, 1456(2003).
11) S.-M. Oh, J.-G. Li and T. Ishigaki, *J. Mater. Res.*, **20**, 529(2005).
12) S.-M. Oh and T. Ishigaki, *Thin Solid Films*, **457**, 186(2004).
13) Y.-L. Li and T. Ishigaki, *J. Phsy. Chem. B*, **108**, 15536(2004).


## ２．２　液体プリカーサーミストの熱プラズマ酸化反応による高機能酸化チタンナノ粒子の合成

### 2.2.1. Introduction

$TiO_2$ finds various aspects of usage in modern sciences and technologies. It remains one of the most promising photocatalysts up to date due to it higher efficiency, better stability, non-toxicity and availability. Considering its high transparency in the visible electromagnetic spectrum, $TiO_2$ is also being regarded as a good host lattice for rare-earth (RE) ions (such as $Eu^{3+}$) for applications in optoelectronic devices. As a photocatalyst, one major disadvantage of $TiO_2$ is that it can only be activated by irradiation with ultraviolet (UV) light, owing to its relatively wide bandgap (~3.2 eV). As the UV light accounts for only ~5% of the solar energy compared to visible light (~45%), any shift in its optical

response from UV to the visible spectral range will have a remarkable positive effect on the practical application of the material. There seem two general approaches to achieve visible light responses of $TiO_2$: substituting the Ti sites of $TiO_2$ lattice with metal cations,[1] mainly transition metals like $Fe^{3+}$, and doping $TiO_2$ with nonmetallic elements, typically nitrogen[2]. The synthesis of Fe-doped $TiO_2$ has been achieved by wet chemical routes, but either post annealing that exclusively results in phase segregation is necessary or the Fe/Ti ratio in the resultant powders significantly deviates from that of the starting solution.[3] N-doping is generally made by annealing pure $TiO_2$ powders under N-containing atmospheres (usually $NH_3$), but has drawbacks of non-uniform dopant distribution, as the nitriding reaction starts at particle surfaces. As for the $TiO_2$/RE system, sol-gel, hydrothermal, and reverse micelle techniques have been employed for its synthesis.[4,5] Effective doping, however, is still rather difficult to achieve in many cases, since the guest and host ions have different ionic sizes and especially different chemical properties, which frequently lead to sequential precipitation. As a result, the RE ions might be simply absorbed on the surfaces of the semiconductor particles, and hence the observed emissions are not due to the energy transferred from the host lattice but due to the direct absorptions by the RE activators themselves.

RF thermal plasma proves to be a powerful tool for synthesizing well-dispersed nanoparticles of good crystallinity within a very short period of time. Its extremely high processing temperature (up to $1.5\times10^4$ K), superfast quenching rate (~$10^{5\text{-}6}$ K/s) at the plasma tail, and its thermal non-equilibrium effects provide a unique reaction field for solid solution formation. We have also used atomized liquid precursors to feed the plasmas, which ensures instantaneous reactions of the liquid precursor with the plasma field and hence high-degree supersaturation of the evaporated species, favoring nanoparticle formation upon gas phase condensation. We demonstrate here the successful synthesis of Fe-,[6] N-,[7] and $Eu^{3+}$-doped[8] $TiO_2$ nanocrystals via Ar/$O_2$ thermal plasma oxidation of liquid precursors containing titanium tetra-*n*-butoxide and the dopant elements. The unique microstructures and novel functional properties of the products are also investigated.

### 2.2.2. Experimental

Fundamental conditions for the synthesis of nanocrystals are as follows: plate power, 25kW; central gas, 30L/min of Ar; sheath gas, 90L/min of mixtures of Ar and $O_2$; atomization gas, 5L/min of Ar; chamber pressure, 66.7kPa; precursor feeding rate, 3.5-4.0g/min. The titanium source is tetra-*n*-butoxide (TTBO) in all the cases. The liquid precursor for Fe-doped $TiO_2$ nanoparticles are organic solutions containing TTBO and ferrocene (Fe/Ti=0-20at%) and stabilized with diethanolamine (DEA, DEA/TTBO=1:1 in molar ratio); The liquid precursor for N-doped $TiO_2$ is organic solutions containing TTBO and DEA (DEA/TTBO=4 in molar ratio). DEA is employed here not only as a stabilizer for TTBO but also as the nitrogen source. On the other hand, the precursor for Eu-doped $TiO_2$ is a mixture of two solutions: (1) DEA-chelated TTBO (DEA/TTBO=4 in molar ratio) and (2) citric acid chelated $Eu(NO_3)_3$ aqueous solution (citric acid/Eu=2:1 in molar ratio).

### 2.2.3. Results and discussion

***2.2.3.1. Fe-doped $TiO_2$.*** Chemical analysis confirmed that the prescribed Fe/Ti molar ratios (*R*) in the precursor solutions have been kept to the final powders. XRD analysis (Fig.2.3) revealed that the resultant nanopowders exclusively contain anatase and rutile. At dopant concentrations up to *R*=5at%, the XRD patterns show normal peaks with symmetric shapes (Fig.2.3). Fe-doping dramatically promotes rutile formation, due to the oxygen vacancies created for charge compensation upon substituting $Fe^{3+}$ for $Ti^{4+}$ sites. Metastable anatase instead of thermodynamically stable rutile is formed as the major phase in the undoped sample, which is consistent with our predictions obtained through theoretical calculations based upon classical nucleation theory, that is, anatase preferentially nucleates from deeply undercooled $TiO_2$ melts while rutile from less deeply undercooled ones [6,9].

In the heavily doped samples (*R*=10 and 20at%), the diffraction peaks expect for (101), (111), and (002)

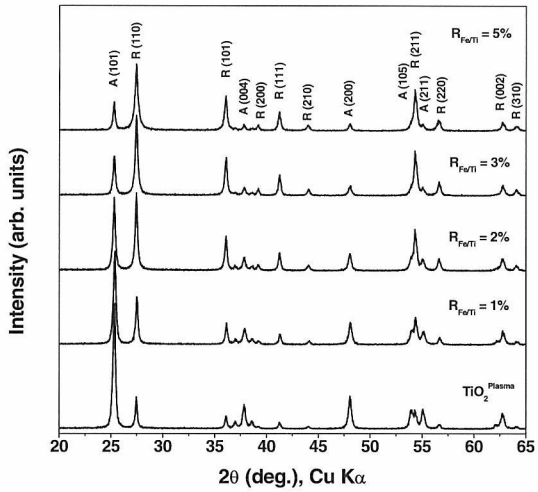


Fig.2.3 XRD patterns of the powders with *R* up to 5at%

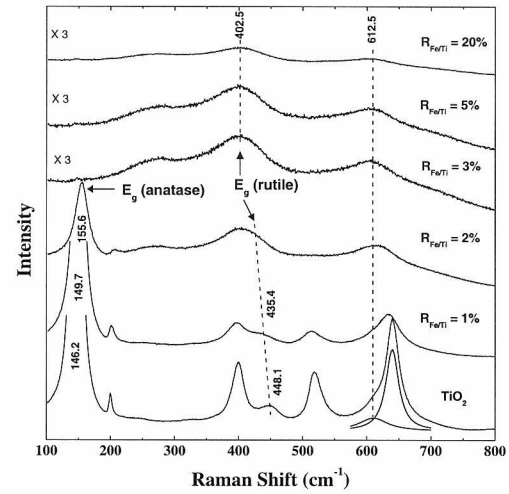


Fig.2.5 Raman spectra of the Fe-doped $TiO_2$ samples

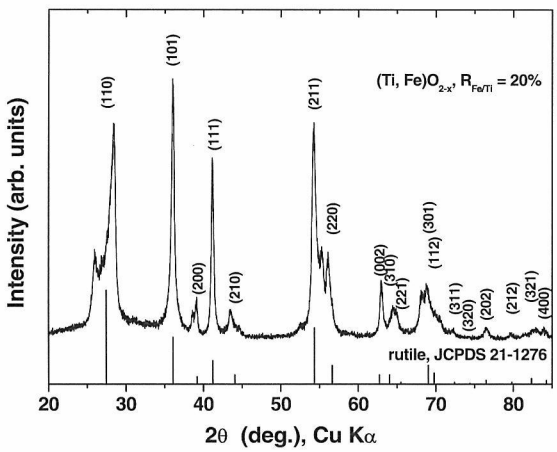


Fig.2.4 XRD pattern of the powder with *R*=20at%.

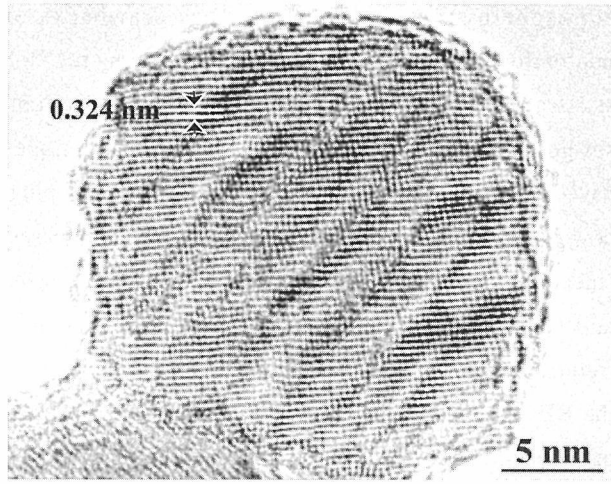


Fig.2.6 TEM image showing the clustering of oxygen vacancies

exhibit asymmetry, which was enhanced with increasing *R* (Fig.2.4). The asymmetric peaks, with (110) in particular, are significantly broadened and weakened, which reflects misalignment of the slabs in such a way that the *d*-spacing was not well defined in the [110] direction. Raman spectroscopy (Fig.2.5) indicates that the anatase $E_g$ mode at 146.2 $cm^{-1}$ shits right wards while the rutile $E_g$ mode at 448.1 $cm^{-1}$ left wards with increasing *R* up to 2at%, which indicates increasing amounts of oxygen vacancies in the crystal structure of $TiO_2$. At higher *R* values, the $E_g$ mode of rutile keeps constant at ~402.5 $cm^{-1}$, suggesting that the oxygen vacancy level in the rutile structure has reached its maximum.

TEM observations indicate that the surplus oxygen vacancies in the samples with *R* above 2at% cluster to form extended defect structure like crystallographic shear plane (Fig.2.6).

Iron doping lowers the energies for both indirect and direct transitions of $TiO_2$ (Fig.2.7), suggesting their potential use as photocatalysts under visible light illuminations.

Further analysis shows that all the Fe-doped nanopowders are paramagnetic at room temperature (Fig.2.8), which provides direct evidence that even as high as 20at% of Fe can be completely doped into $TiO_2$ via RF thermal plasma processing.

***2.2.3.2. N-doped $TiO_2$.*** For the N-doped $TiO_2$ samples, XRD analysis shows that they contain only anatase and rutile, and again, metastable anatase was formed as the major phase (>70 wt%), irrespective of the oxygen input rates in the plasma sheath. The anatase content tends to increase at a higher $O_2$ flow rate (Fig.2.9), which might be understood from the facts that (1) the increased addition of diatomic oxygen gas causes deeper undercooling of the $TiO_2$ melt at the plasma tail and therefore favors

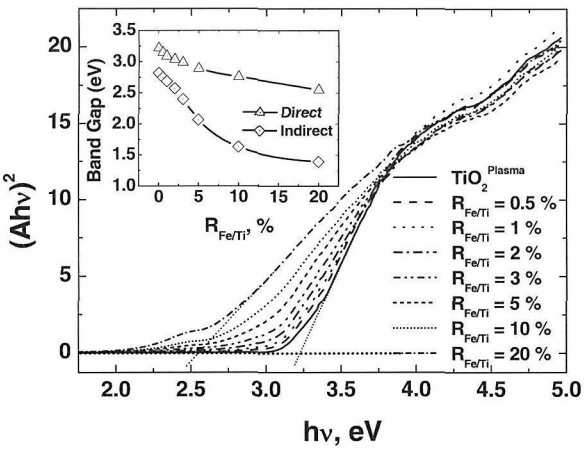


Fig.2.7 Bandgap narrowing of $TiO_2$ by $Fe^{3+}$ doping

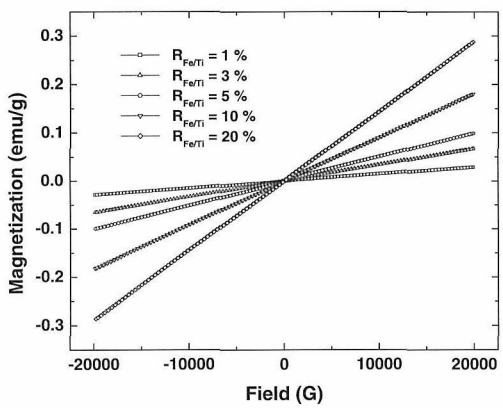


Fig.2.8 Magnetic properties of the Fe-doped $TiO_2$ powders measured at room temperature

anatase nucleation[6,9], and (2) a higher $O_2$ input reduces oxygen deficiencies in the $TiO_2$ gas clusters, beneficial to anatase formation upon gas phase condensation.[10,11] The nitrogen concentration tends to increase along with the anatase content (Fig.2.9), implying that nitrogen is readily doped into the anatase lattice. The powders show weak dependence on the $O_2$ input in the plasma sheath, and have average crystallite sizes of ~40 nm and specific surface areas of ~30-50 $m^2/g$. Fig.2.10 shows typical morphologies (SEM) of the plasma generated N-doped $TiO_2$ powders. Though particles having diameters bigger than 100 nm are present, most of the crystallites have sizes around 35 nm and are largely dispersed. These two distinctly different types of particle morphologies may arise from the different trajectories of the precursor mists

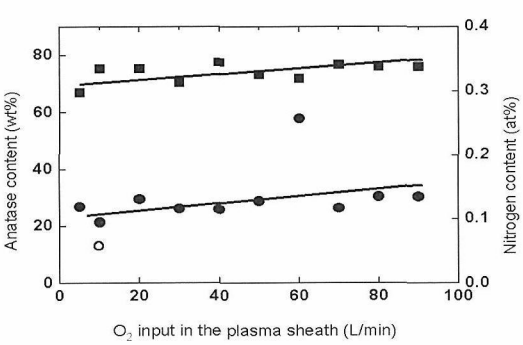


Fig.2.9 Anatase (filled square) and N (filled circle) contents of the powders, as a function of the $O_2$ input in the plasma sheath

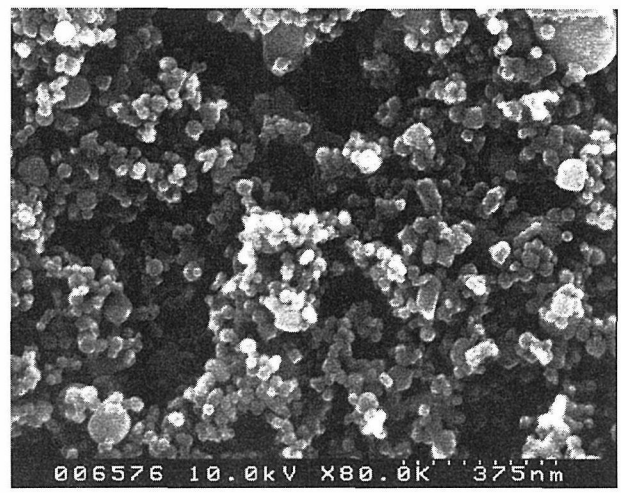


Fig.2.10 SEM micrograph showing morphology of the N-doped $TiO_2$ powder synthesized with 10L/min of $O_2$ input

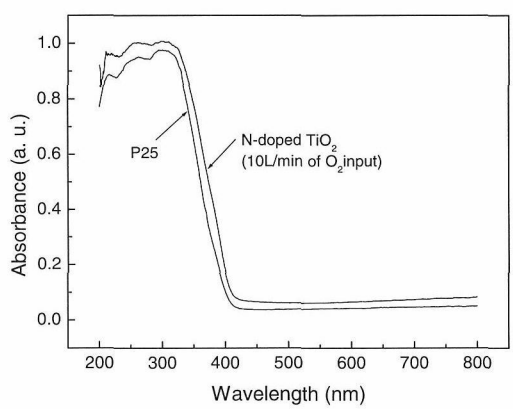


Fig.2.11 UV-Vis spectra of P25 and N-doped $TiO_2$

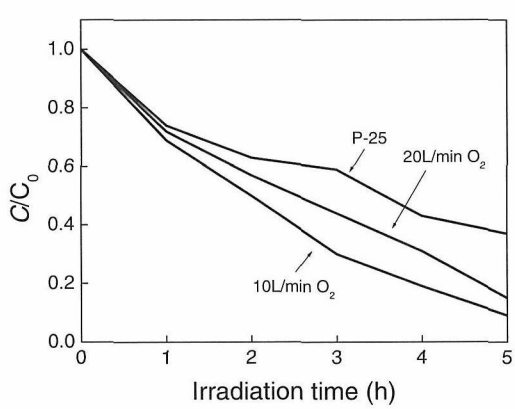


Fig.2.12 Bleaching of 100μM methyl orange solution

in the hot zone of the thermal plasma.

Figure.2.11 shows UV-Vis spectrum of the $TiO_2$ powder synthesized with 10 L/min of $O_2$ input in the plasma sheath, compared with that of the Degussa P25 powder. The P25 powder has a bandgap of ~3.04 eV, while the N-doped powder exhibits a narrowed one of ~3.00 eV, showing bandgap narrowing of the N-doped $TiO_2$. the N-doped $TiO_2$ powders exhibit higher efficiencies than Degussa P25, a model photocatalyst, in the bleaching of methyl orange solution (100μmol/L) under visible light (>400 nm) irradiation (Fig.2.12).

***2.2.3.3. Eu-doped $TiO_2$ luminescent nanocrystals.*** Eu-doped $TiO_2$ nanopowders with Eu/Ti up to 5at% have been made via 50Ar/40$O_2$ thermal plasma oxidation of liquid precursor mists, and their physical properties were investigated. XRD analysis (Fig.2.13) indicates that the solubility of $Eu^{3+}$ in the $TiO_2$ lattice is limited to about 0.5at%, above which $Eu_2Ti_2O_7$ pyrochlore was formed in the final products, mainly owing to the large size discrepancy ($Ti^{4+}$:0.0605nm, $Eu^{3+}$:0.0947nm).

Further analysis indicates that the crystallize sizes of anatase and rutile stay in the ranges 30-36nm and 64-83nm, respectively. Rutile content of the nanopowder, however, increases steadily at a higher Eu addition, due to the creation o f oxygen vacancies in the $TiO_2$ gas clusters by substitutional $Eu^{3+}$ doping (Fig.2.14).

Figure.2.15 shows UV-Vis diffuse reflectance spectra of the $TiO_2$:$Eu^{3+}$ nanopowders compared with pure $TiO_2$ and $Eu_2Ti_2O_7$ synthesized similarly. The pure $TiO_2$ sample exhibits an onset of absorption at 405 nm, corresponding to a bandgap of 3.06 eV. In addition to the absorption in the UV region, the pyrochlore powder shows additional absorptions at 395, 416, 467, and 538

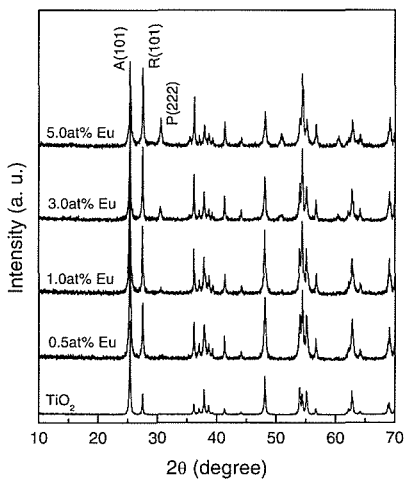


Fig.2.13 XRD patterns of Eu-doped $TiO_2$ nanopowders. A, R, and P denote anatase, rutile, and pyrochlore, respectively.

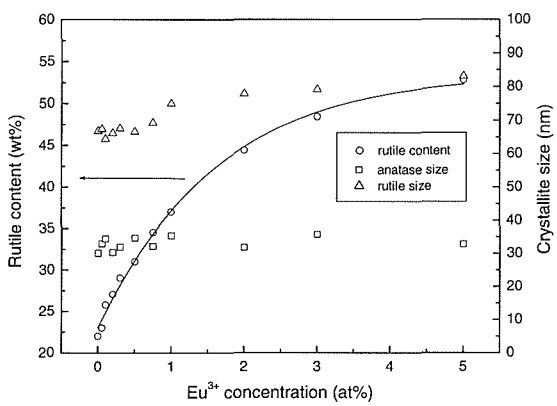


Fig.2.14 phase constituents and crystallite sizes of the resultant powders.

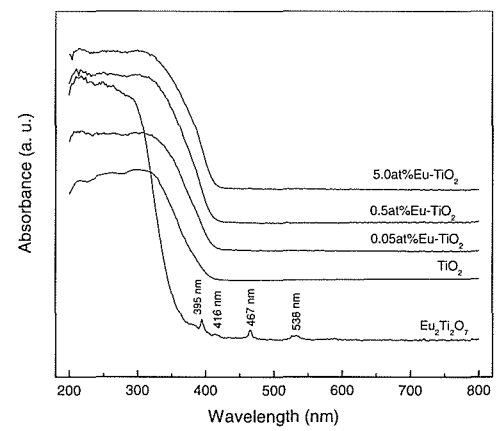


Fig.2.15 UV-Vis diffuse reflectance spectra of the plasma generated powders.

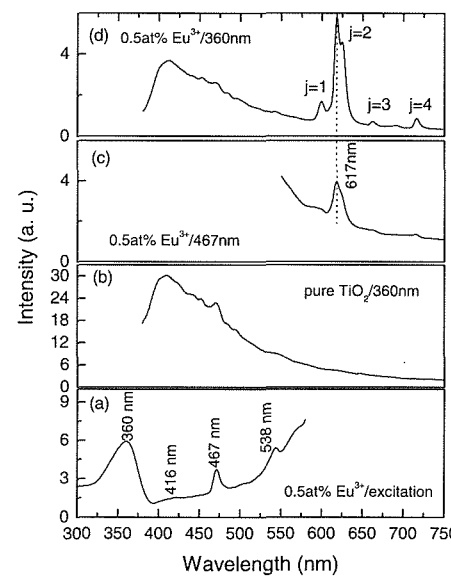


Fig.2.16 Excitation and emission spectra of the nanopowders.

nm, which are assignable to the intra-configurational $4f \rightarrow 4f$ transitions of $Eu^{3+}$ ions. These absorptions were not observed in the $TiO_2$:$Eu^{3+}$ nanopowders mainly due to the weakness of the peaks.

Figure.2.16(a) demonstrates excitation spectrum of the 0.5at% $Eu^{3+}$ doped $TiO_2$ nanopowder, measured by monitoring the 617 nm emission from the $^5D_0 \rightarrow {}^7F_2$ transition of $Eu^{3+}$ ions. The three peaks at 416, 467, and 538 nm, which show features similar to those observed in the UV-Vis spectrum of $Eu_2Ti_2O_7$, can be assigned to the $^7F_{0,1} \rightarrow {}^5D_3$, $^7F_{0,1} \rightarrow {}^5D_2$, and $^7F_{0,1} \rightarrow {}^5D_1$ transitions of the $Eu^{3+}$ions, respectively. The broad peak at 360 nm, whose position coincides well with the absorption band of pure $TiO_2$ (Fig.2.15), indicates that $Eu^{3+}$ ions can be effectively excited through the $TiO_2$ host lattice (notice that the right-hand tail of the 360 nm peak overlaps the left-hand tail of the 416 nm peak). When excited at 467 nm, a wavelength longer than the absorption edge of $TiO_2$ (405 nm), the $Eu^{3+}$-doped nanopowder exhibits characteristic emissions in the range 550-750 nm (Fig.2.16(c)), which are associated with the electronic transitions from the excited $^5D_0$ level to $^7F_j$ (j=1, 2, 3,4) levels of $Eu^{3+}$ activators arising from the absorption by the $Eu^{3+}$ ions themselves. Excited at a wavelength (360 nm) shorter than the absorption edge of $TiO_2$ (Fig.2.16(d)), the $Eu^{3+}$ doped powder shows luminescence from both the $TiO_2$ host and the $Eu^{3+}$ ions, but the $Eu^{3+}$ emission is clearly stronger that that from the host lattice (Fig.2.16(b)) and than that under 467 nm excitation (Fig.2.16(c)), suggesting an efficient nonradiative energy transfer from the $TiO_2$ host to $Eu^{3+}$ ions.

Luminescence behavior of the $TiO_2$:$Eu^{3+}$ powders was also studied with 325nm He-Cd laser excitation, and the results are shown in Fig. 17. It is the $^5D_0 \rightarrow {}^7F_2$ transition that gives a sharp red color when a 325 nm He-Cd laser beam impinged upon sample surfaces. The $Eu^{3+}$-doped samples exhibit emissions clearly different from those of $Eu_2O_3$ and $Eu_2Ti_2O_7$, in terms of peak positions and peak shapes, which provides direct evidence that the emissions from $TiO_2$:$Eu^{3+}$ arise from the $Eu^{3+}$ ions doped into the $TiO_2$ lattice and not from separated $Eu_2O_3$ or $Eu_2Ti_2O_7$ particles.

Figure.2.18 displays relative luminescence

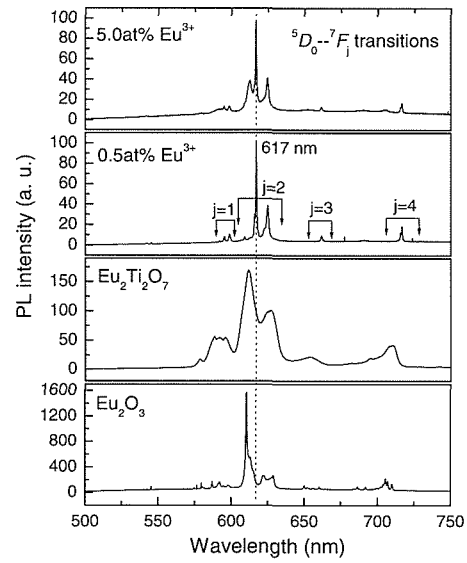


Fig.2.17 Emission spectra of the $TiO_2$:Eu nanopowders under 325 nm He-Cd laser excitation compared with those of $Eu_2Ti_2O_7$ and $Eu_2O_3$.

intensity of the nanopowders, as a function of the $Eu^{3+}$ concentration in the precursor solution. The PL intensity (monitored as the 617 nm emission) increases sharply and almost linearly with increasing the $Eu^{3+}$ content up to 0.5at% and then levels off. Such a phenomenon is primary due to the formation of $Eu_2Ti_2O_7$ pyrochlore arising from the limited solubility of $Eu^{3+}$ in the $TiO_2$ lattice. Further improvement in the luminescence intensity might be achieved by properly increasing the $Eu^{3+}$ content in the $TiO_2$ lattice.

### 2.2.4. Conclusions

Doping of $TiO_2$ with both metallic and non-metallic elements was achieved by $Ar/O_2$ thermal plasma oxidation of liquid precursor mists. For Fe-doped $TiO_2$, we identified for the first time the existence of saturation of oxygen vacancies and the formation of extended defect structures when the $Fe^{3+}$ content in the $TiO_2$ lattice exceeds about 2at%. N-doping was confirmed in the plasma generated $TiO_2$ powders, and due to their lowered band gap, the powders show higher efficiency than p25 in the bleaching of methyl orange solutions under visible light irradiations. As for the Eu-doped $TiO_2$ powders, efficient non-radiative energy transfer from the host lattice to $Eu^{3+}$ activators, which was rarely observed in the wet-chemically synthesized powders of the same system, was confirmed by combined studies of UV-Vis,

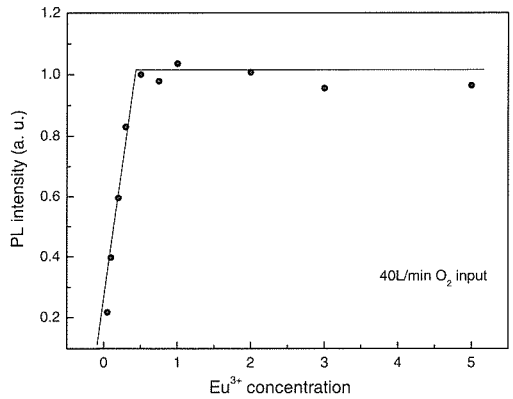


Fig.2.18 Relative intensities of the 617 nm emission, as a function of the $Eu^{3+}$ addition in the precursor solution.

excitation and PL spectroscopy, and as a result bright red emissions were observed from the powders either by directly exciting the $Eu^{3+}$ ions with light of energy lower than the band gap of $TiO_2$ or by directly exciting the $TiO_2$ host lattice.

## References


1) M.R. Hoffmann, S.T. Martin, W. Choi, D.W. Bahnemann - *Chem. Rev.* **95**, 69 (1995).
2) R. Asahi, T. Morikawa, T. Ohwaki, K. Aoki, Y. Taga – *Science* **293**, 269 (2001).
3) M. Hirano, T. Oji, M. Inagaki, *J. Am. Ceram. Soc.*, **87**, 35 (2004).
4) A. A. Bol, R. van Beek, A. Meijerink, *Chem Mater.*, **14**, 1121 (2002).
5) J. Ovenstone, P. J. Titler, R. Withnall, J. Silver, *J. Phys. Chem. B,* **105**, 7170 (2001).
6) X. H. Wang, J.-G. Li, H. Kamiyama, M. Katada, N. Ohashi, Y. Moriyoshi, T. Ishigaki, *J. Am. Chem. Soc.*,**127**, 10982 (2005).
7) J.-G. Li, H. Kamiyama, X. H. Wang, Y. Moriyoshi, T. Ishigaki, *J. Euro. Ceram. Soc.*,**26**, 423 (2006)
8) J.-G. Li, X. H. Wang, K. watanabe, T. Ishigaki, *J. Phys. Chem. B,* **110**, 1121 (2006).
9) Y.-L. Li, T. Ishigaki , *J. Cryst. Growth* **242**, 511 (2002).
10) S.-M. Oh, J.-G. Li, T. Ishigaki, *J. Mater. Res.*, **20**, 529 (2005).
11) Y.-L. Li, T. Ishigaki, *J. Phys. Chem. B,* **108**, 15536 (2004).

# 第３章　パルス変調熱プラズマを利用した材料プロセス

## ３．１　新しいプラズマ発生法―パルス変調RFプラズマ法－の開発と酸化亜鉛のUV発光高効率化

熱プラズマの有する熱的側面を押さえて、化学的効果をさらに顕在化させるために熱プラズマの発生をtime domainで制御する新しい発生法、パルス変調RFプラズマ法を開発した[1]。パルス変調RFプラズマ法は、ミリ秒単位でRF電力をハイレベル、ローレベルに変調して繰り返す。このような発生法が可能になった背景として、高出力インバーター電源の発達により、出力変調可能なハイパワーRF電源が入手できたことがあげられる[2]。その優れたスイッチング特性を利用して、高周波の周期であるマイクロ秒より十分に長い時間で、連続発生時の出力レベル（ハイレベル）と連続発生ではプラズマを維持できないほどに低い出力レベル（ローレベル）を繰り返すことにより、プラズマの総エネルギーを低減することが可能になった。

ローレベルのRF電力は、連続発生を維持できないほどに小さく、プラズマは一種の遷移状態になっている。ここで、パルス変調発生には、連続発生にはない新たな発生パラメーターが加わったことになる。ローレベルを減少されることにより、パルスオン、オフにともなうプラズマ温度の急激な変化はプラズマに擾乱をあたえ、プラズマへの非平衡性を導入する効果があり、高化学活性なラジカル濃度の上昇の兆候も認められた[3)-6)]。

酸化亜鉛は低圧電子線で発光する高効率蛍光体として知られており、真空蛍光管や電界発光ディスプレーとして使用されてきた。近年、酸化亜鉛には紫外発光素子への応用に対する期待が高まっている。また最近のZnOに関する理論的な検討から、特に、そのドナー準位の形成において、酸化亜鉛中に不純物として含まれる水素が非常に重要な役割を果たすことが指摘されている。この理論的な検討に先立ち、ZnOの紫外線発光効率の向上に水素ドープが極めて有効であるとことが見いだされた[7)]。ここでは、未処理のZnO単結晶では、結晶中の欠陥や不純物によって形成されたドナー準位やアクセプター準位を介した可視発光(1.5-3eV))が顕著に認められたが、これにマイクロ波で発生した水素プラズマを照射することによって、欠陥、あるいは、不純物が不活性化され、3.3eVの紫外発光効率が改善された。

このZnOへの水素ドープに際し、プラズマを利用した方法ではいくつかの問題が生じる。そのひとつはプラズマ自身からの輻射熱やラジカルが再結合する際の反応熱によって、試料に熱的なダメージが加わることである。特に、ZnOは欠陥を作りやすい化合物であり、水素を含む雰囲気中で加熱されると、気化蒸発が起こる可能性がある。そこで、パルス変調プラズマ法という新しいプラズマ発生技術をZnOへの水素ドーピング処理に利用した。

連続モードおよびパルス変調モードのプラズマ照射により、ZnO中への水素ドープを行った[8)-9)]。パルス変調したアルゴン－水素プラズマ照射による酸化亜鉛のフォトミネッセンスの変化を調べた。水素含有プラズマ照射により、可視域での発光が押さえられ、さらにパルス変調プラズマ照射では、380nmにピークをもつ紫外発光がさらに向上し、未処理試料の位15倍以上の発光が得られた。この試料は、RFコイルの下方75mmの位置でパルス変調モード照射した。この位置はプラズマフレームの中にあるにもかかわらず、高濃度の水素ラジカル照射が熱的ダメージなく行われたことを示している。この紫外発光には、表面から100nm以下の深さにとけ込んだ数十ppmの水素が影響していると思われる[10)]。水素は酸化亜鉛中の格子欠陥（発光中心あるいは非発光中心となっている）にはいり、輻射あるいは非輻射遷移を抑制するので、バンド端発光効率が上昇したと考えられる。

また、レーザーアブレーション法で得られた酸化亜鉛薄膜をこのように水素プラズマ処理することによりレーザー発振の励起エネルギーが小さくなることも見いだされた[11)]。本研究で得られた高効率紫外発光酸化亜鉛を発展させていくことにより、省エネルギー型高輝度ディスプレー、高感度シンチレーター、ＤＶＤピックアップ用レーザー、紫外Ｌ

ＥＤ、環境センサーなどへの応用が期待できる。

## References


1) T. Ishigaki, X. Fan, T. Sakuta, T. Banjo and Y. Shibuya, *Appl. Phys. Lett.*, **71**, 3787(1997).
2) T. Sakuta and T. Ishigaki, *Pure Appl. Chem.*, **71**, 1845(1999).
3) T. Sakuta, K.C. Paul, M. Katsuki and T. Ishigaki, *J. Appl. Phys.*, **85**, 1372(1999).
4) R. Ye, T. Ishigaki and M.I. Boulos, *J. Appl. Phys.*, **96**, 118 (2004).
5) R. Ye, T. Ishigaki and T. Sakuta, *Plasma Sources Sci. Technol.*, **14**, 387(2005).
6) R. Ye and T. Ishigaki, *J. Appl. Phys.*, **97**, 123306(2005).
7) T. Sekiguchi, N. Ohashi and Y. Terada, *Jpn. J. Appl. Phys.*, **36**, L289(1996).
8) N. Ohashi, T. Ishigaki, N. Okada, I. Sakaguchi, T. Sekiguchi and H. Haneda, *Appl. Phys. Lett.*, **80**, 2869(2002).
9) T. Ishigaki, N. Okada, N. Ohashi, H. Haneda and T. Sakuta, *Pure Appl. Chem.*, **74**, 435(2002).
10) N. Ohashi, T. Ishigaki, N. Okada, H. Taguchi, I. Sakaguchi, S. Hishita, T. Sekiguchi and H. Haneda, *J. Appl. Phys.*, **93**, 6386(2003).
11) Y.G. Wang, N. Ohashi, T. Ishigaki, Y. Wada, H. Taguchi, I. Sakaguchi, T. Ohgaki, and H. Haneda, 投稿中 .


## ３．２　材料合成プロセスに利用するパルス変調 RF 熱プラズマの特徴

### 3.2.1. Introduction

Synthesis and processing of materials have been attracting a great deal of attention as it enters the high-tech era of 21st century. The emphasis will be placed on the development of new materials by using promising technique routes which will conserve energy, be more productive, and be environment-friendly. Plasma technology is becoming an important role in achieving these goals in the field of materials processing.

Radio frequency (rf) inductively coupled thermal plasma is characterized by its high energy density (>10 000 K), large volume (30~50 mm), high quench rate ($10^5$~$10^6$ K/s), short processing time ($10^0$~$10^1$ ms), high concentrations of chemically reactive species ($10^{21}$~$10^{24}$ $m^{-3}$), and contamination-free (electrodeless). These features make it possible to facilitate some kinds of materials processing requiring extreme thermal and chemical conditions which are difficult to be realized using conventional ways. RF thermal plasma has been used in a wide variety of spectrums in materials processing ranging from synthesis of nanosize powders, deposition of thin films, surface modification of particulate materials, and spraying coatings [1-3]. In most industrial applications, rf plasma torches are operated in continuous mode, i.e., their power levels are fixed throughout the operation. In order to increase the application potential of rf plasmas in materials processing, pulse-modulated inductively coupled plasmas (PM-ICPs) under high-pressure and high electric power conditions have been developed by the cooperation between our group and the group in the University of Kanazawa [4,5]. The difference between the higher- and lower-power levels during the pulsed-power operation is large enough to change the equilibrium state in the plasmas. PM-ICPs are expected to offer a unique heat source with controllable concentrations of chemically reactive species and thermodynamic nonequilibrium for advanced materials processing [6-8]. Ar-$H_2$ PM-ICP has been found to be a promising tool for hydrogenation of ZnO to improve its ultraviolet emission efficiency [9-11], as shown in Fig.3.1.

Recently, experimental and theoretical studies have been carried out to shed light on some new phenomena arising from such pulsed-power plasmas [12-14]. We have analyzed the main mechanism responsible for the time-dependent behavior of PM-ICPs by detecting the atomic emission intensities and by evaluating the

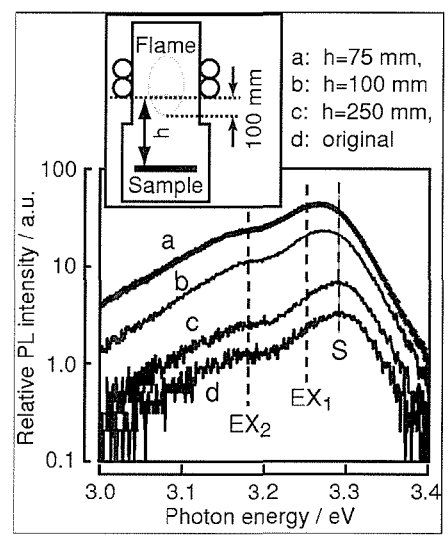


Fig.3.1 PL spectra of polycrystalline ZnO before (d) and after hydrogenation (a–c). Inset shows relative sample position in the reactor [10].

characteristic times of the particle transport processes. We have further determined the controlled operating ranges of the PM-ICPs under various operating conditions. On the other hand, we have conducted numerical analyses of the response of energy and momentum transfer in the PM-ICPs, as well as the effect of plasma turbulence on the transient behavior of the PM-ICPs. Furthermore, we investigated the transient behavior of thermal nonequilibrium in an Ar PM-ICP using a two-temperature model, showed how the electron and heavy particle temperatures changed with the input power.

### 3.2.2. Controlled generation of PM-ICPs

Ar-$H_2$ and Ar-$N_2$ nonequilibrium thermal plasmas were generated under well-controlled pulse-modulated power conditions using a voltage-control-type power source. The overshoot and undershoot of the coil current were considerably reduced by using an exponentially rising control signal [12]. Spectroscopic measurements of the radiation intensity of the Ar atomic spectral line (751.5 nm) indicated that the transient behavior of the plasma temperatures and the emission spectra were dependent on the operating conditions and the position in the plasma torch.

Analysis of the various transport processes of the plasmas enabled us to elucidate the transient behavior of the time-variation plasmas. It shows that the response time of the plasmas to the changes in input power was attributed to the particle transport processes. Theoretical analyses using an energy transfer model for rf plasmas [15,16] indicated that the on-delay time was mainly determined by the transition from a recombination-dominated process to an ionization-overwhelming one. The on-delay time decreased with increasing shimmer current level (SCL) because of the higher electron temperatures, and consequently the higher ionization frequencies at higher SCLs, as illustrated in Fig.3.2. The rise time was largely influenced by the characteristic time of ionization, which was estimated to be 0.2–1.1 ms and was in line with the measured rise times (0.56–0.84 ms for the Ar–$H_2$ plasma, 0.69–1.09 ms for the Ar–$N_2$ plasma). Although the emission started to increase earlier when the SCL was higher, its rise time was also affected by the exponentially rising control signal which had a time constant of 0.94 ms. The total on-delay and rise times, however, decreased with increasing SCL. As the plasma temperature increased, the plasma began to adjust its size and volume through radial convection, and this process determined the relaxation time needed to reach the new quasi-equilibrium. The decay time at the pulse-off stage was principally controlled by the recombination process, which had an estimated characteristic time of more than 1.4 ms and was in agreement with the experimental results (1.36–1.78 ms for Ar–$H_2$, 1.03–1.53 ms for Ar –$N_2$). The recombination rate decreased quickly with the temperature, resulting in longer fall times at smaller SCLs. The off-delay time, however, did not change much with the SCL because the plasma powers at the instance of pulse-off were at the same level for various SCLs.

It was observed that the plasmas became unstable and eventually diminished when the SCL was decreased to certain critical values. To control the generation of PM-ICPs, we experimentally determined the ranges of operating parameters— including the shimmer current level and the pulse-on and pulse-off times.

The ranges of pulse-on and pulse-off times within which well-controlled Ar-$H_2$ and Ar-$N_2$ plasmas could be generated at 17 kW and 100 kPa are shown in Fig.3.3. When SCL=60%, a 2-ms pulse-on time was too short for the Ar-$H_2$ plasma to be heated sufficiently at the higher

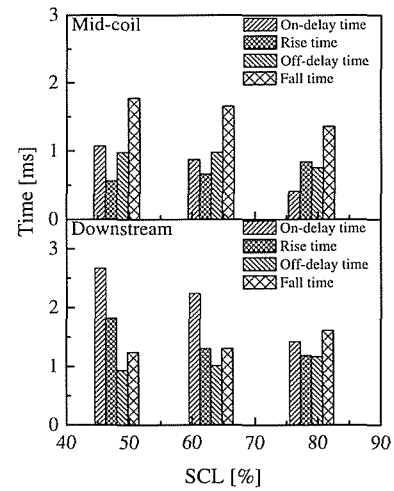


Fig.3.2 Characteristic times of Ar-$H_2$ PM-ICP for pulse on/off times of 10/5 ms with higher power level of 17 kW.

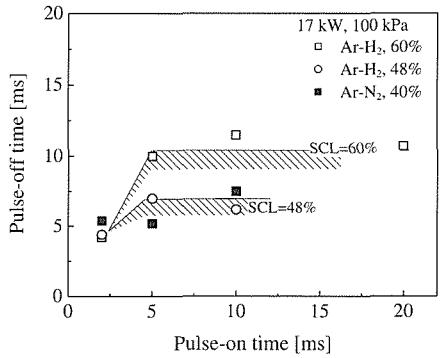


Fig.3.3 Controlled generation ranges of the Ar-$H_2$ and Ar-$N_2$ PM-ICPs.

power level, and the plasma could only be sustained within a pulse-off time of 4.2 ms. The critical pulse-off time increased to about 10 ms when the pulse-on time was increased to 5 ms, and it could not be further increased because after 5 ms the plasma properties were already stabilized. The operating range became smaller when the SCL was decreased: When the SCL was reduced to 48% the critical pulse-off time could not exceed 7 ms due to that the plasma was too cold to be recovered at the lower power levels. The critical SCLs for the Ar-$H_2$ and Ar-$N_2$ plasmas were determined. The Ar-$H_2$ plasma could be operated until the SCL went down to 48% at 17 kW and 100 kPa. This was equivalent to a power level of about 4 kW, a power too low for the plasma to operate continuously. The critical SCL for Ar-$N_2$ plasma could be reduced even further: It was only 40% and the low power level was less than 3 kW. The shaded areas in Fig.3.3 illustrate the ranges of pulse-on and pulse-off times within which the Ar-$H_2$ plasma could run stably without interruption at SCLs of 60% and 48%.

### 3.2.3. Transient behavior of turbulent rf plasma

A Renormalization Group (RNG) k-ε turbulence model [17] was employed to investigate the role of turbulence in the transient behavior of the radio frequency induction plasma discharge. Transient responses of energy, momentum and turbulence to step-like and pulsed power changes in an Ar-$H_2$ plasma with a hydrogen volumetric concentration of 10.9%, and a total gas flow rate of 104.0 slpm were studied. From the predicted results, we found that the plasma energy, momentum and turbulence responded differently to the changes in input power. A qualitative comparison made between the predicted temperatures and the images taken with a high-speed camera under the same operating conditions suggested that the turbulence model predicts the transient responses of plasma volume and temperature more accurately than the laminar model does [13].

Figure.3.4 indicates that the plasma temperature responded to the power change almost instantaneously. The plasma temperature and volume changed considerably in the first 5 ms. After that, their variations mainly occurred in the upstream and near-wall regions. The evolution of the axial velocity was quite similar to that of the temperature, indicating that the energy and momentum shared similar transport mechanisms in the

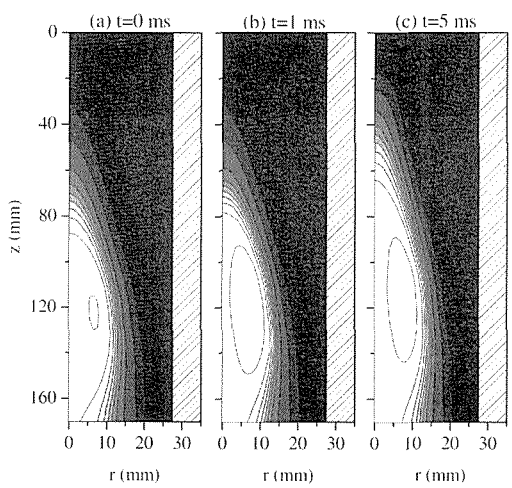


Fig.3.4 Time-dependent behavior of plasma temperature under step-like power change from 7.3 to 15.3 kW. The maximum temperature contour is 11000 K with a decrement of 1000 K.

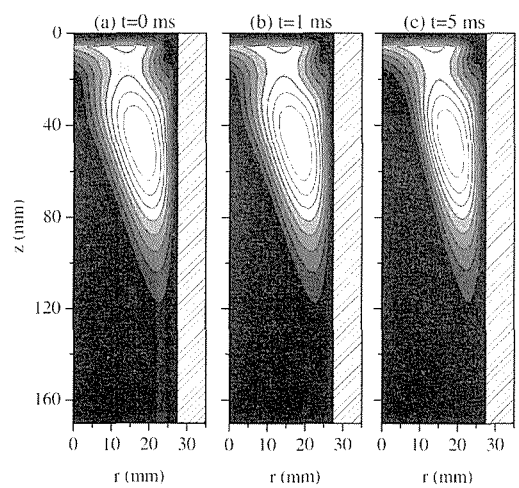


Fig.3.5 Time-dependent behavior of relative turbulent viscosity under step-like power change from 7.3 to 15.3 kW. The maximum contour value is 45 with a decrement of 5.

transient plasma. Fig.3.5 shows that, in the first 5 ms, the relative turbulent intensity only changed slightly in the fringes of the plasma, however in the triangle zone of the upstream and near the torch wall, the turbulence still could hardly 'feel' the change in power. The major variation in the turbulence took place after the power had been changed for more than 5 ms. The time for the turbulence to respond to the power change was apparently longer than those of the energy and momentum. As pointed out by Mostaghimi *et al.*, for a rf plasma torch, the relaxation of the energy was determined primarily by radial convection [18]. The relaxation of plasma velocity, strongly associated with the temperature, was also determined by radial convection. Although it can be shown that the relaxation of turbulence was also governed by convection, however both its characteristic length and velocity were different from those of the energy and momentum, owing to the fact that the major change in the turbulence occurred in the recirculation zone. The relaxation time for turbulence was determined by the time taken by the fluid particles traveling from the coil region to the recirculation region. The characteristic length and velocity were about $L_t$=50–100 mm, and $U_t$=1–10 m/s, resulting in a turbulence relaxation time of 5–100 ms.

### 3.2.4. Transient nonequilibrium phenomena in Ar PM-ICP

A time-dependent two-temperature model is developed to simulate the behavior of an argon radio frequency plasma under transient nonequilibrium conditions, with emphasis to understand the temporal and spatial evolution of the nonequilibrium phenomena in pulsed power plasmas [14].

The results show that the effects of changes in input power on the thermal nonequilibrium and the ionization nonequilibrium were most prominent at the early stages of pulse-on and -off. Fig.3.6 illustrates the temporal and spatial behavior of the degree of nonequilibrium in the plasma torch after pulse on. In the central region of the torch (r<5 mm), the degree of nonequilibrium remained quite small (varying by just a few percent) throughout the pulsation, suggesting that the equilibrium was hardly affected by the pulse-modulated operation and the plasma was in quasi-local thermal equilibrium in this region. However, the nonequilibrium situation on the outer side of the torch was significantly influenced. The profile of the degree of nonequilibrium varied noticeably in the first 0.5 ms at the early stages of pulse-off and -on. It took about 1 ms for the degree of nonequilibrium to reach its stable values. The temporal evolution of the ionization nonequilibrium did not keep pace with that of the thermal nonequilibrium, resulting in a slower and smoother relaxation process of the electron number density, as in Fig.3.7. In the first 0.1 ms after the pulse-on and -off, the variation in the electron number density was hardly seen owing to the longer time scales of the electron generation and transport. The electron number density had a noticeable overshoot at about 2 ms after the pulse-on, indicating that the plasma deviated significantly from ionization equilibrium and more chemically reactive species were generated in the PM-ICP. These features are

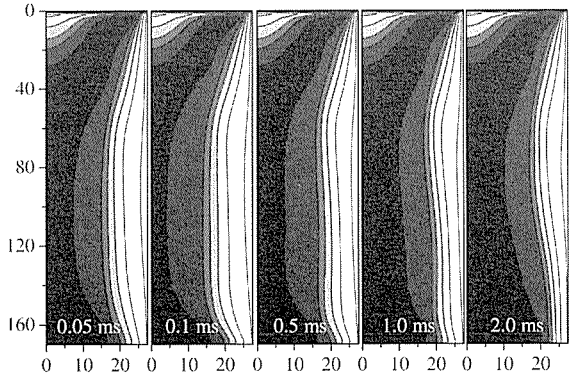


Fig.3.6 Time-dependent behavior of the degree of nonequilibrium $[(T_e-T_h)/T_e]$ after pulse on.

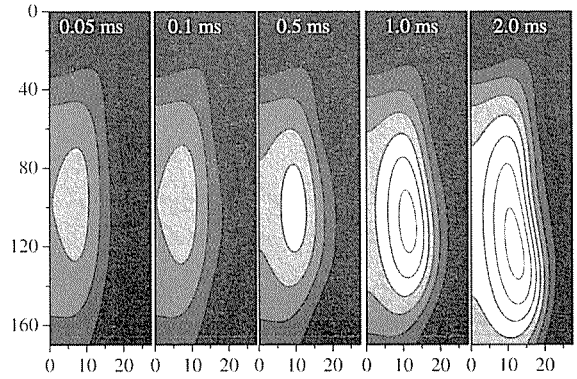


Fig.3.7 Time-dependent behavior of the electron density after pulse on. The maximum contour value is $8\times10^{21}$ $m^{-3}$ with a decrement of $1\times10^{21}$ $m^{-3}$.

very attractive to some materials processing. The effects of operating conditions on the transient behavior of the nonequilibrium situations under pulsed power conditions were also examined. It indicated that, for materials processing, a pulse duration between 2 and 10 ms was adequate for rf plasmas operated in pulse-modulated modes.

## References


1) E. Pfender, *Plasma Chem. Plasma Process.*, **19**, 1 (1999).
2) M. I. Boulos, *Pure Appl. Chem.*, **68**, 1007 (1996).
3) T. Yoshida, *Mater. Trans. JIM*, **45**, **1** (1990).
4) T. Ishigaki, X. Fan, T. Sakuta, T. Banjo, and Y. Shibuya, *Appl. Phys. Lett.*, **71**, 3787 (1997).
5) Y. Tanaka and T. Sakuta, *Plasma Sources Sci. Technol.*, **12**, 69 (2003).
6) T. Ishigaki, X. Fan, T. Sakuta, T. Banjo, and Y. Shibuya, *Appl. Phys. Lett.*, **71**, 3787 (1997).
7) Y. Tanaka and T. Sakuta, *Plasma Sources Sci. Technol.*, **12**, 69 (2003).
8) T. Sakuta and T. Ishigaki, *Pure Appl. Chem.*, **71**, 1845 (1999).
9) T. Ishigaki, N. Okada, N. Ohashi, H. Heneda, and T. Sakuta, *Pure Appl. Chem.*, **74**, 435 (2002).
10) N. Ohashi, T. Ishigaki, N. Okada, T. Sekiguchi, I. Sakaguchi, and H. Haneda, *Appl. Phys. Lett.*, *80*, 2869 (2002).
11) N. Ohashi, T. Ishigaki, N. Okada, H. Taguchi, I. Sakaguchi, S. Hishita, T. Sekiguchi, and H. Haneda, *J. Appl. Phys.*, **93**, 6386 (2003).
12) R. Ye, T. Ishigaki and T. Sakuta, *Plasma Sources Sci. Technol.*, **14**, 387 (2005).
13) R. Ye, Ishigaki, and M. I. Boulos, *J. Appl. Phys.*, **96**, 118 (2004).
14) R. Ye and T. Ishigaki, *J. Appl. Phys.*, **97**, 123306 (2005).
15) J. A. M. van der Mullen and J. Jonkers, *Spectrochimica Acta*, **54B**, 1017 (1999).
16) M. J. van de Sande, P. van Eck, A. Sola, A. Gamero, J. A. M. van der Mullen, *Spectrochimica Acta*, **58B**, 783 (2003).
17) V. Yakhot, S. A. Orszag, S. Thangam, T. B. Gatski, and C. G. Speziale, *Phys. Fluids*, **A4**, 1510 (1992).
18) J. Mostaghimi, K. C. Paul, and T. Sakuta, *J. Appl. Phys.*, **83**, 1898 (1998).

# 第４章　デュアルマグネトロンスパッタリング法による酸化物薄膜合成

## ４．１　はじめに

スパッタリング法は緻密で付着力の高い薄膜材料を大面積にコーティングする技術の代表例として広く用いられている。またスパッタリング法はプラズマプロセスであり、その高い化学的反応性を生かした各種薄膜形成のためのプロセス温度の低温化にも非常に有効である。このため多くの酸化物、窒化物等の機能薄膜の形成プロセスとしてスパッタリングが採用されている。

近年矩形パルス状の電力をスパッタリングのプロセスプラズマの駆動に採用することによりアーキングと呼ばれる異常放電を著しく低減させる試みがなされ、成功をおさめている[1,2]。これにより異常放電が障害となって電力投入を大きく出来なかった場合においても大きな電力を投入することが可能となり、特に反応性スパッタリング法において酸化物、窒化物等の絶縁性薄膜の形成における成膜速度の飛躍的（1 桁以上）向上が実現された。

大電力投入が実現されたため、スパッタリングプラズマの化学的反応性の向上およびそれに伴う薄膜形成のためのプロセス温度のさらなる低温化がこの手法に大いに期待された。しかしながら低温化はある程度達成されたものの、光触媒効果によるセルフクリーニング作用等が注目され、ガラス表面へのコーティングにより汚れないガラス等を形成するために必須な材料である二酸化チタン等の結晶薄膜を無過熱で基板上に形成することは出来なかった。

本研究ではこの成膜プロセス温度の低温化に特化して前述のパルススパッタリング技術を独自に高度化し、プラスチック等の耐熱温度の低い基体上にも結晶化した酸化物／窒化物機能薄膜を形成することを目的として実施した。

## ４．２　成膜設備概略

Fig.4.1 に本研究で用いたデュアルマグネトロンパルススパッタリング装置の外観および模式図を示す。90° の角度を成して配置した２基のマグネトロンを備えており、各マグネトロンには原料ターゲットが設置され、両極性パルス電力を２基のマグネトロン間に印加することによりスパッタリング成膜を実施する。各マグネトロンに設置した原料ターゲット表面は矩形パルス波の極性に従って陰極／陽極／陰極／陽極…と極性を変えてゆくバイポーラ型と呼ばれる放電モードを備えている。バイポーラ放電モードを適用することにより、両マグネトロン電極表面は常にスパッタリングによりクリーニングされた状態を保ち、通常の反応性スパッタリング法による絶縁薄膜形成の際に顕著な電極表面の絶縁膜被覆による異常放電の問題が発生しないことも大きな特徴であり、このため投入電力が大きくとれ、高成膜速度化や低プロセス温度化に有効とされる。

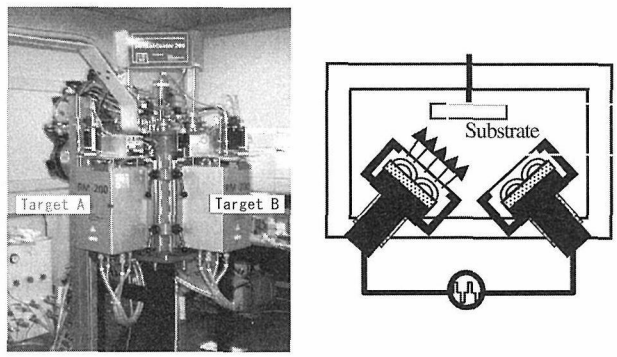

Fig.4.1 The picture and the schematic diagram of the sputtering apparatus.

本成膜装置はドイツフラウンホーファー研究所との共同開発によるものであるが、本研究においてはさらに独自の機構によってラジカル等の活性化学種の密度を上げる工夫を随所に施し、低プロセス温度下（無加熱）において結晶化した酸化物／窒化物薄膜を得ることを実現した。

## ４．３　二酸化チタン薄膜の無過熱結晶化

上記パルススパッタリング装置の性能を実証するために、ポリエチレンテレフタレート（PET）フィルム上への二酸化チタン光触媒機能薄膜の形成実験を試みた。二酸化チタン材料の光触媒活性は材料の結晶性に大きく依存し、結晶の品質の向上が活性の向上に直接結びつくことが報告されている。

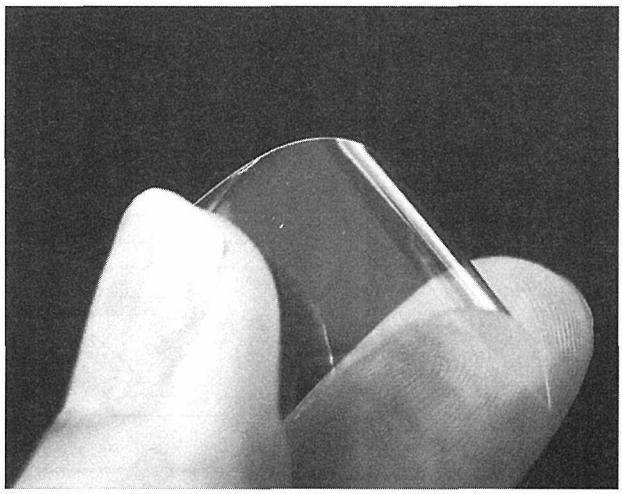

Fig.4.2 The picture of the crystallized $TiO_2$ film grown on a PET film.

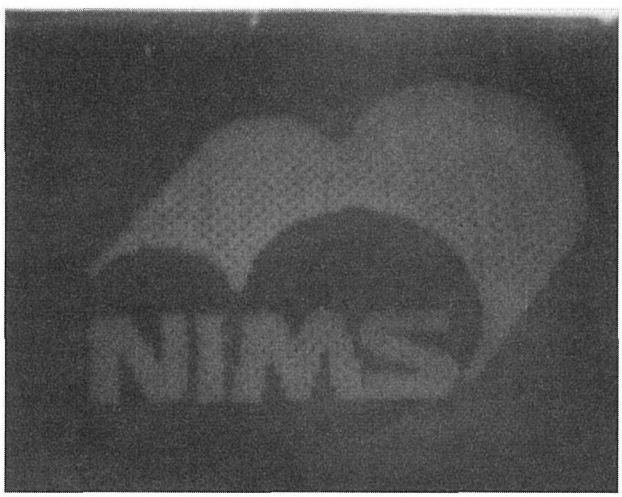


Fig.4.3 The NIMS LOGO obtained by the photocatalytic reaction of the crystallized $TiO_2$ film grown on a PET film.

二酸化チタン材料の結晶化薄膜を as-grown で得るためには、通常プロセス温度、この場合は成膜中の基板温度として 300℃以上が必要とされてきた。すなわち従来の成膜手法においては 150℃前後の耐熱性しか有しないプラスチック基板上に結晶化して光触媒活性を有する薄膜を形成することは不可能であった。

Fig.4.2 に PET 樹脂フィルム上に無加熱で作成した結晶化二酸化チタン薄膜の写真を示す。曲げても全く支障はなく、摩擦によっても極めて剥離しにくいため、ハードコーティングとしての使用も可能である。

Fig.4.3 に示したのは上記 PET 樹脂フィルム上に無加熱で作成した結晶化二酸化チタン薄膜の光触媒活性を用いて浮き上がらせた物質・材料研究機構のロゴマークである。0.1 モル / リットルの硝酸銀水溶液中にコーティング膜を浸し、その状態で紫外線を照射し、光触媒反応による銀イオンの還元反応によりパターンを形成した [3]。Fig.4.3 において明るく観測されるロゴの部分はマスクにより紫外光がさえぎられ、コーティング膜による光触媒反応が発現しなかった部分である。

2 基のマグネトロンにチタン金属原料ターゲットを搭載し、バイポーラモードにおいて投入パルス電力 3kW+3kW で成膜を実施した。この場合成膜速度としては 20 ～ 40 ナノメートル毎分の高速成膜が実現する。成膜時の雰囲気はアルゴンガスを 0.5Pa、反応性原料ガスの酸素はスパッタリングの放電モードがトランジェントモードとなり、高速に反応性スパッタリングが実施されるようプラズマ発光を光学的にモニターし、酸素供給を実施している高速応答方のピエゾバルブによってフィードバック制御を実施した。

基板には PET フィルムを用い、成膜時の基板加熱は実施していない。スパッタ成膜中にプラズマからの輻射等の影響により基板の温度は次第に上昇し、10 ～ 20 分後の成膜終了時点で基板の温度は 80 ～ 120℃に上昇する。従来の成膜手法においてはこの温度領域で得られるのは非晶質の二酸化チタン膜であったが、本研究で開発した技術を用いることにより、PET 樹脂の耐熱温度の範囲内で結晶化した二酸化チタン薄膜を得ることが可能になった [4]。

## 4．4　おわりに

本技術により加熱が不可能、あるいは著しく困難な大面積ガラスやプラスチック基板上へ二酸化チタン結晶膜を形成する道が拓かれた。本技術をスケールアップし、実際の大面積ガラスコーティング用のスパッタリング装置へ展開することにより、セルフクリーニング機能を持った窓ガラスの実現が期待でき、高層ビル窓ガラスのクリーニング作業の危険回避やコストの大幅削減につながる。またプラスチック等の材料に対しても光触媒作用を付与することが可能になるため、セルフクリーニング機能を持ったプラスチック材料を作製することが可能になり、そこから派生する多様な用途の開拓も期待される。

## References


1) P. Frach, K. Goedicke, C. Gottfried, H. Bartzsch: Surf. Coat. Tech., 142, (2001) 628.
2) S. Ohno, D. Sato, M. Kon, Y. Sato, M. Yoshikawa, P. Frach and Y. Shigesato: Jpn. J. Appl. Phys., 43, (2004) 8234.
3) S. Nishimoto. B. Ohtani, H. Kajiwara, T. Kagiya: J. Chem. Soc., Faraday Trans., 179, (1983) 2685.
4) 特許出願（出願番号 2004-152921 等、合計 7 件出願中）。

# 第５章　低圧誘導結合プラズマによるナノクリスタルダイヤモンド合成

## ５．１　はじめに

化学的気相成長法（CVD）やエッチングに代表されるプラズマプロセスにおいては、低圧（＜１Torr)、大面積（＞φ 12 インチ)、且つ高密度（＞$10^{12}$ $cm^{-3}$）プラズマが求められている[1,2]。それらの要求を満足するプラズマ源として最初に電子サイクロトロン共鳴（ECR）プラズマが開発され、引き続いてヘリコン波励起プラズマ、表面波励起プラズマが提案され活発な研究が行われてきた。一方、低圧誘導結合プラズマ（ICP）もまた低圧力で、しかも無磁場で高密度を実現できるプラズマ源として注目を集め精力的な研究が進められている[3,4]。また最近では、発想を変えて『必要な場所に必要な大きさのプラズマを生成』し、ミクロなスポット領域でプロセスを行う『マイクロプラズマ』が注目され、精力的に研究が進められている[5]。

一方、プラズマ CVD によるダイヤモンド合成に用いられるプラズマは、現在 10 ～ 100 Torr のマイクロ波プラズマ[6]及び大気圧付近の熱プラズマ[7]が一般的である。ECR プラズマが唯一 0.1 Torr 以下でのダイヤモンド合成に用いられているにすぎない[8]。Bozeman らは[9] ICP を用いて 4 Torr でのダイヤモンド合成を報告しているが、0.1 Torr 以下のいわゆる低圧 ICP でのダイヤモンドの合成については筆者らが最初に報告して以来[10-12]、Teii らによる報告例があるのみで[13]、合成手法・条件とも十分確立されていないのが現状である。従って、プロセシングプラズマの一つとして有望な低圧 ICP によるダイヤモンドの合成手法を確立し、成長条件の最適化を図ることは、将来のダイヤモンド薄膜の電子デバイス化等の観点からも極めて重要であると考えられる。

## ５．２　ナノクリスタルダイヤモンドとナノクリスタルエンジニアリング

炭素原子の $sp^3$ 結合からなるダイヤモンドは 90-100GPa の高硬度性と 0.02-0.03 の低摩擦係数・耐摩耗性を有する。また、ホウ素などのドーピングにより容易にｐ型半導体にもなる。ダイヤモンド薄膜を金属、セラミックス、半導体等にコーティングすることによって、これらの優れた特性を生かしたコーティング材料や電子デバイス材料への応用が可能である。これまでダイヤモンドの成膜は主に熱フィラメント法[14]、マイクロ波プラズマ CVD[6]で行われてきた。その結晶粒径はμｍのオーダーで表面の凹凸が大きいために摩擦係数が大きくなり、優れたトライボロジー特性は得られなかった。最近、従来の成膜条件とは異なる領域で結晶粒径が nm オーダーのナノクリスタルダイヤモンドが合成できることが明らかとなった。結晶粒径を nm オーダーに制御したナノクリスタルダイヤモンド薄膜では、高い硬度を維持してダイヤモンドとしての特長を維持しながら表面が平坦で低い摩擦係数を実現することができる。

nm オーダーに制御された超微小結晶を精緻に合成し、３次元構造化することにより、通常では、得られない超平坦・超硬度・超潤滑特性を発現させることができる。この技術の利用によりナノクリスタルダイヤモンドは、従来のバルクの性質を上回る超高硬度、超低摩擦、化学的、電気的特性などの発現が可能となる。μｍオーダーから nm オーダーの粒界を、さらに粒子間に化学結合の形成、或いは、マトリクッス中のナノクリスタルを形成することにより、急激に超硬度特性や表面平坦性を発現させる“ナノクリスタルエンジニアリング”という概念が提唱されている[15]。ナノクリスタルダイヤモンドに代表される超高硬度ナノクリスタルは、nm に制御された超薄膜のナノクリスタル多層構造形成により、摩擦・摩耗等の機械的特性、電気的特性の発現、並びにそれら表面の化学修飾による撥水性等が飛躍的に向上する。

本章では、低圧 ICP-CVD によるナノクリスタルダイヤモンドの合成と構造評価を中心に述べ、その応用分野についても簡単にレビューする。

## ５．３　プラズマ CVD によるナノクリスタルダイヤモンドの合成

プラズマ CVD によるナノクリスタルダイヤモン

ドの合成に関する研究においては、マイクロ波プラズマ CVD が最も一般的に用いられている。ナノクリスタルダイヤモンドの合成条件として、通常の多結晶ダイヤモンドを合成する場合よりも高 $CH_4$ 濃度で成長させる方法[16-18]と、Gruen らが提唱した $H_2$ の代わりに Ar 等の希ガスプラズマ中で成長させる方法[19,20]がある。いずれの手法においても合成されたナノクリスタルダイヤモンドは、結晶自形を持たない粒径数 nm から数十 nm の微結晶体である。最近、Butler らは基板前処理として水素終端のカーボン膜を堆積させたあとナノダイヤモンド粒子を種付けすることにより $10^{12}$ 個／$cm^2$ を越える核発生密度を得て、厚さ 100nm から 5$\mu$m の連続自立膜の合成に成功し、極めて優れた熱伝導率（2.5-12W/cmK）を達成した[21]。

これまでにマイクロ波プラズマ以外にも、dc プラズマ[22]、熱フィラメント[23]、マグネトロンスパッタリング[24]、rf プラズマ[25-27]がナノクリスタルダイヤモンドの合成に用いられてきた。

## 5．4　低圧誘導結合プラズマ CVD によるナノクリスタルダイヤモンドの合成と構造評価

Fig.5.1 に示す低圧 ICP-CVD システム[10-12]においては、螺旋状に 3 回巻かれたアンテナに 13.56 MHz、1 kW の高周波電力を印加することにより

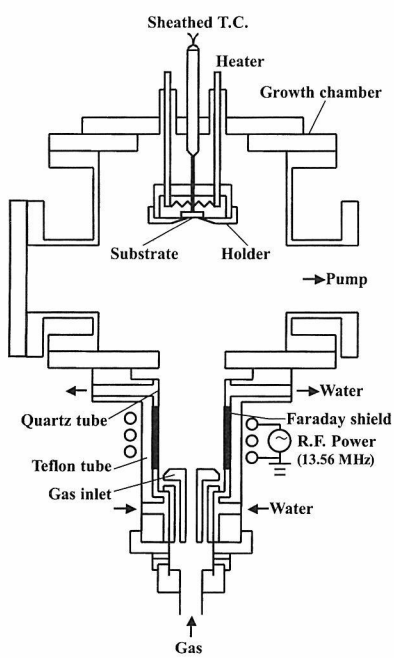


Fig.5.1　Schematic diagram of the low pressure ICP-CVD system.

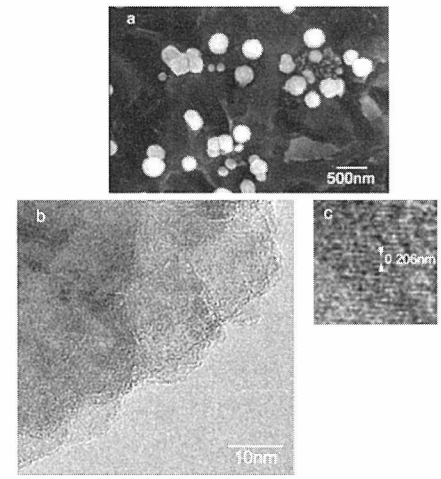


Fig.5.2(a)　SEM image of nanocrystalline diamond particles, (b) high-resolution TEM image of an outer part of nanocrystalline diamond particle, and (c) enlargement of the left-hand side of (b).

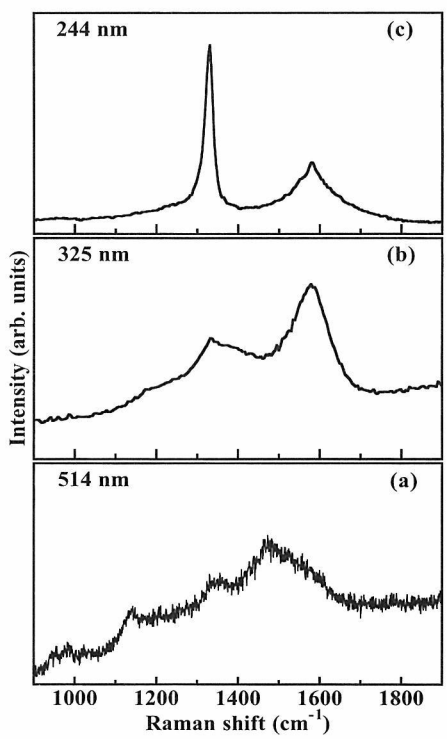


Fig.5.3　Raman spectra of nanocrystalline diamond particles with different excitation wavelength: (a) 514.5 nm, (b) 325 nm, and (c) 244 nm.

誘導結合プラズマを発生させている。圧力 45-50 mTorr の $CH_4/CO/H_2$ 系低圧 ICP により合成されたナノクリスタルダイヤモンドは Fig.5.2(a) に示すように、粒径 200-500 nm の球状の粒子であり、それぞれの粒子は Fig.5.2(b) のように数十 nm のサブグレインからなっている[12]。

ラマン分光法はダイヤモンドの $sp^3$ 結合、グラファイトやアモルファスカーボンの $sp^2$ 結合を振

動分光学的に評価する最も一般的な方法である。ナノクリスタルダイヤモンドのような微結晶構造の場合、Fig.5.3 に示すように、514.5 nm 励起ラマンスペクトルにおいては $sp^3$ 結合炭素ネットワークに対応する 1150 $cm^{-1}$ 付近のピークは現れるが、1332 $cm^{-1}$ のダイヤモンドピークは明瞭には現れない[28]。これは $sp^2$ 結合炭素の $\pi$ - $\pi^*$ 遷移による共鳴ラマン効果により $sp^2$ 結合に起因するピークのみが増強され、ダイヤモンドピークに重畳してしまうためである[28]。それに対して 325 nm 励起のラマンスペクトルにおいては 1332 $cm^{-1}$ のダイヤモンドピークが明瞭に現れ、同時に $sp^2$ 結合炭素に起因する 1580 $cm^{-1}$ 付近の G ピークも著しく増強される。更に波長の短い 244 nm 励起のラマンスペクトルにおいては 1332 $cm^{-1}$ のダイヤモンドピークのみが増強され、G ピークは減少する。これらの 325 nm 及び 244 nm の紫外光励起ラマンスペクトルの変化は、$sp^2$ 結合炭素の $\pi$ - $\pi^*$ 遷移による共鳴ラマン効果の抑制、$sp^3$ 結合炭素の $\sigma$ - $\sigma^*$ 遷移の共鳴効果により説明することができる[29]。

さらに、電子エネルギー損失分光法（EELS）によりナノクリスタルダイヤモンドのサブグレインの $sp^2/sp^3$ 結合の分布を評価した[30]。Fig.5.4 に図 30(b) に対応するナノクリスタルダイヤモンドの EELS スペクトルを示す。スペクトルには、290 eV に $\sigma^*$ に起因する明瞭なピークと 285 eV 付近に $\pi^*$ に起因する微かなピークが現れる。スペクトル形状はダイヤモンドの標準的な EELS スペクトルにほぼ一致することから、$\sigma^*$ ピークは $sp^3$ 結合、$\pi^*$ ピークは $sp^2$ 結合にそれぞれ起因するものであると考えられる。従って、$\pi^*$ 及び $\sigma^*$ ピークのエネルギー位置にフィルターをかけることにより、$sp^2/sp^3$ 結合の分布（マッピング）を得ることができる。Fig.5.2(b) に対応する EELS の $\pi^*$ イメージ、$\sigma^*$ イメージを Fig.5.5(a),(b) にそれぞれ示す。$\pi^*$ イメージの強度はサブグレインの粒界で強くなっているのに対して、$\sigma^*$ イメージの強度はサブグレイン内で強くなっている。従って、$sp^2$ 結合がサブグレインの粒界に局在していることがわかる。また、その $sp^2$ 結合の幅は約 1 nm と見積もられる。

最後に原料ガスにおける CO 添加効果について考察を加える。$CH_4/H_2$ に添加された CO はプラズマ中で電子衝撃解離（$CO + e \rightarrow C + O + e$）により、原子状酸素（O）が生成する。生成した O は主として $H_2$ 及び $CH_4$ との反応により消滅し、結果として OH ラジカルの増加をもたらす[31]。同時に原子状水素、$CH_3$ ラジカルも生成される。さらに OH ラジカルは逐次反応により、原子状水素、$CH_3$ ラジカルを生成する[31]。OH ラジカル及び原子状水素はダイヤモンド成長に必要な表面での水素引き抜き反応を促進して成長のラジカルサイトを作り、一方 $CH_3$ ラジカルはダイヤモンド成長の前駆体ラジカルとなる。従って、CO 添加により生成した OH ラジカルがダイヤモンド成長条件下における非ダイヤモンド炭素の除去に効果的な役割を果たし、同時に表面での水素引き抜き反応を促進して、ダイヤモンド成長に有利な条件を作り出しているものと考えられ

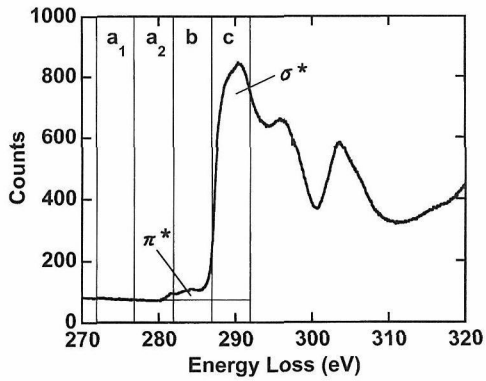


Fig.5.4 EEL spectrum corresponding to Fig.5.2(b). **a**$_1$, **a**$_2$, **b**, and **c** indicate the four energy windows; 272-277 eV, 277-282 eV, 282-287 eV, and 287-292 eV, respectively.

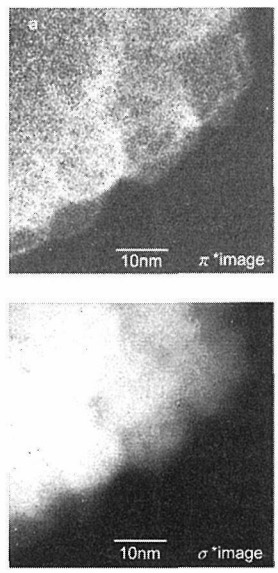


Fig.5.5(a) $\pi^*$ image corresponding to Fig.5.2(b), and (b) $\sigma^*$ image corresponding to Fig.5.2(b).

る。

## 5．5　ナノクリスタルダイヤモンドの応用分野

ナノクリスタルダイヤモンドに代表される共有結合性微細構造物質は最近の20年間、ダイヤモンドの気相合成に続くフラーレン、カーボンナノチューブの合成手法の確立により、科学的、基礎的な側面と電子デバイス等への応用の観点から極めて大きな注目を集め、ナノテクノロジーを支える重要な基盤材料の一つとなっている[32-34]。特にアモルファスナノ構造カーボン膜は電子放出材料、冷陰極材料、硬質低摩擦コーティング材料等への応用が精力的に進められてきた。

一方、ナノクリスタルダイヤモンド膜もまた低摩擦係数を持ち、且つ電子放出電位が低いことから大いに注目を集めてきた。通常のμmサイズの多結晶ダイヤモンドに比べて、ナノクリスタルダイヤモンドの約5-100 nmという小さなグレインサイズがその優れたトライボロジー特性及び電界放出特性をもたらしている[35]。前者の超硬度、低摩擦係数を利用したMEMS(Micro Electro Mechanical System)用材料への応用、超硬度、耐腐食性、透明性を生かしたガラス・光学部品へのコーティング、金型工具へのコーティング、生体材料へのコーティング、バイオケミカルデバイス等への応用が提案されている[36-37]。後者の優れた電界放出特性を利用するものとしては、電界放出材料への応用であり、さらに半導体材料として、窒素を不純物としてドーピングしたn型ナノクリスタルダイヤモンド薄膜も報告されている[38]。Table 5.1にナノクリスタルダイヤモンド（NCD）の主な特性とそれらを活かした期待される応用例、及び単結晶ダイヤモンド（SCD）/マイクロクリスタルダイヤモンド（MCD）との比較をまとめておく[39]。

低圧ICPによるナノクリスタルダイヤモンドの合成の過程において、部分的ではあるがFig.5.6に示すような粒径数nmの“ダイヤモンドナノボール”が合成されることを見出した。これらの数nmのサイズでは量子効果の発現が十分期待され、ダイヤモンドのワイドバンドギャップを利用した紫外発光材料、或いは、最近Prawerが提案しているナノクリスタルダイヤモンド粒子を用いた量子ドットコンピュータへの応用[40]が考えられる。

## 5．6　おわりに

本研究では、低圧ICPによりこれまで十分に確立されていなかった低圧領域でのダイヤモンド合成を試み、ナノクリスタルダイヤモンド粒子の合成に成功した。紫外光励起ラマン分光法及びEELSによる構造解析により、結晶粒界に約1nmの幅で$sp^2$結合が局在していることが明らかとなった。それらの情報は、各種材料への応用の際必要となってくるnmオーダーの結晶粒界の制御を行う上で重要な知見を与えてくれるものと考えられる。

Table 5.1 Some properties of nanocrystalline diamond films.[39]

| Properties | SCD/MCD | NCD | Potential application |
|---|---|---|---|
| Electric properties | | | |
| Band gap (eV) | 5.5 | 2-5.5 | electric devices |
| Electron affinity | negative | negative | |
| Onset of field emission (V/μm) | 160 | 3-4 | field emission display |
| Resistivity (Ωcm) | $>10^{10}$ | $>10^{6}$ | |
| Optical properties | | | |
| Transmission | UV to far IR | 78-84% transmittance beyond 700 nm | optical coatings |
| Refractive index @ 633 nm | 2.41 | 2.27-2.35 | IR windows |
| Mechanical properties | | | |
| Hardness (GPa) | ～100 | >90 | wear resistant, protective coatings |
| Young's modulus (GPa) | 1054 | ～1000 | |
| Coefficient of friction | <0.1 | 0.1-0.01 | MEMS/NEMS |
| Structural properties | | | |
| Bonding character | 100% $sp^3$-C | >90%$sp^3$-C | |
| Grain size (nm) | - | 2-100 | |
| Surface roughness (nm) | - | 2-50 | |
| Thermal conductivity (W/cm K) | 20 | 12 | |

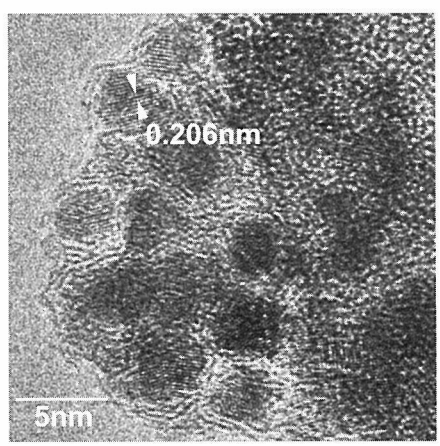


Fig.5.6 High-resolution TEM image of “Diamond Nanoballs”.

## 謝辞

本研究を遂行する上で、EELS 測定においては物質研究所の木本浩司博士に全面的なご協力を頂いた。また、同研究所の小松正二郎博士、松本精一郎博士にも有益な議論、助言を頂いたことに併せて感謝いたします。

## References

1) M. A. Lieberman and A. J. Lichtenberg, *Principles of Plasma Discharges and Materials Processing* ( John Wiley & Sons, New York, 1994).

2) 菅井秀郎、応用物理 **63**, 559 (1994).

3) J. Amorim, H. S. Maciel, and J. P. Sudano, J. Vac. Sci. Technol. **B9**, 362(1991).

4) J. Hopwood, Plasma Sources Sci. Technol. **1**, 109(1992).

5) 橘邦英、第 65 回応用物理学会学術講演会講演予稿集 2p-N-3 (2004).

6) M. Kamo, Y. Sato, S. Matsumoto, and N. Setaka, J. Cryst. Growth **62**, 642 (1983).

7) S. Matsumoto, M. Hino, and T. Kobayashi, Appl. Phys. Lett. **51**, 737 (1987).

8) H. Kawarada, K. Mar, and A. Hiraki, Jpn. J. Appl. Phys. **26**, L1032 (1987).

9) S. P. Bozeman, D. A. Tucker, B. R. Stoner, J. T. Glass, and W. M. Hooke, Appl. Phys. Lett. **66**, 3579 (1995).

10) K. Okada, S. Komatsu, T. Ishigaki, and S. Matsumoto, in *Chemical Vapor Deposition of Refractory Metals and Ceramics III,* W. Y. Lee, B. M. Gallois, andM. A. Pickering, Eds., Mat. Res. Soc. Symp. Proc. **363**, Pittsburgh, PA, p. 157, 1995.

11) K. Okada, S. Komatsu, T. Ishigaki, and S. Matsumoto, Proc. 12th Inter. Symp. Plasma Chem., Minnesota, p.2261, 1995.

12) K. Okada, S. Komatsu, and S. Matsumoto, J. Mater. Res. **14,** 578 (1999).

13) K. Teii and T. Yoshida, J. Appl. Phys. **85,** 1864 (1999).

14) S. Matsumoto, Y. Sato, M. Kamo, and N. Setaka, Jpn. J. Appl. Phys. **21**, L183 (1982).

15) 古賀義紀　編、「省エネルギー化のための超硬度ナノクリスタルエンジニアリングに関する調査」報告書(14 年度新エネ研第 0626001 号)

16) R. Erz, W. Dotter, D. Jung, and H. Ehrhardt, Diamond Relat. Mater. **2,** 449 (1993).

17) J. Lee, B. Hong, R. Messier, and R. W. Collins, Appl. Phys. Lett. **69,** 1716 (1996).

18) T. Sharda, M. M. Rahaman, Y. Nukaya, T. Soga, T. Jimbo, and M. Umeno, Diamond Relat. Mater. **10,** 561 (2001).

19) D. M. Gruen, S. Lui, A. R. Krauss, J. Luo, and X. Pan, Appl. Phys. Lett. **64,** 1502 (1994).

20) D. Zhou, T. G. McCauley, L. C. Qin, A. R. Krauss, and D. M. Gruen, J. Appl. Phys. **83,** 540 (1998).

21) J. Philip, P. Hess, T. Feygelson, J. E. Butler, S. Chattopadhyay, K. H. Chen,and L. C. Chen, J. Appl. Phys. **93,** 2164 (2003).

22) V. I. Konov, A. A. Smolin, V. G. Ralchenko, S. M. Pimenov, and E. D. Obraztsova, Diamond Relat. Mater. **4,** 1073 (1995).

23) A. V. Khomich, V. I. Polyakov, P. I. Perov, V. P. Varnin, and I. G. Terenmetskaya, Mater. Res. Soc. Symp. Proc. **423,** 723 (1996).

24) S. N. Kundu, M. Basu, A. B. Maity, S. Chaudhuri, and A. K. Pal, Mater. Lett. **31,** 303 (1997).

25) D. V. Fedoseev, V. L. Bukhovets, I. G. Varshavskaya, and Y. N. Tolmachev, Russ. J. Phys. Chem. **70,** 1594 (1996).

26) G. Amaratunga, A. Putnis, K. Clay, and W. Milne, Appl. Phys. Lett. **55,** 634 (1989).

27) G. A. J. Amaratunga, S. R. P. Silva, and D. A. McKenzie, J. Appl. Phys. **70,** 5374 (1991).

28) K. Okada, H. Kanda, S. Komatsu, and S. Matsumoto, J. Appl. Phys. **88,** 1674 (2000).

29) J. Wagner, M. Ramsteiner, Ch. Wild, and P. Koidl, Phys. Rev. **B40,** 1817 (1989).

30) K. Okada, K. Kimoto, S. Komatsu, and S. Matsumoto, J. Appl. Phys. **93,** 3120 (2003).

31) D. L. Baulch, C. J. Cobos, R. A. Cox, C. Esser, P. Frank, Th. Just, J. A. Kerr, M. J. Pilling, J. Troe, and R. W. Walker, J. Phys. Chem. Ref. Data **21**, 411 (1992).

32) J. Robertson, Prog. Solid State Chem. **21,** 199 (1991).

33) M. P. Siegal, W. I. Milne, and J. E. Jaskie, Eds., *Covalently Bonded Disordered Thin-Film Materials*, Mater. Res. Soc. Symp. Proc. Vol. 498, Pittsburgh, PA, 1998.

34) D. M. Gruen, Annu. Rev. Mater. Sci. **29**, 211 (1999).

35) J. E. Butler, D. S. Y. Hsu, B. H. Houston, X. Lui, J. Vignola, T. Feygelson, J. Wang, and C. T. –C. Nyguen, 8th Inter. Conf. New Diamond Sci. Tech., Melbourne, p. 116, 2002.

36) J. A. Carlisle, J. Birrell, J. E. Gerbi, O. Auciello, J. M. Gibson, and D. M. Gruen, 8th Inter. Conf. New Diamond Sci. Tech., Melbourne, p. 129, 2002.

37) G. M. Swain, A. B. Anderson, J. C. Angus, MRS Bull. p.56, 1998.

38) P. Hollman, O. Wanstrand and S. Hogmark, Diamond and Related Materials, **7,** 1471 (1998).

39) T. Sharda and S. Bhattacharyya, *Encyclopedia of Nanoscience and Nanotechnology,* **2,** 337 (2004).

40) S. Prawer, Proc. Inter. Symp. Advan. Mater. (ISAM 2003), Tsukuba, 2003.

# 第６章　反応性熱プラズマを利用した炭素粉末の高機能化

## ６．１　はじめに

炭素粉末のように大気圧下では溶融しない物質を熱プラズマ中に供給したときも、化学的な効果が顕著にあらわれた。近年モバイル電子機器の電源として多く使われているリチウムイオン二次電池の負極には、いろいろな炭素粉末が用いられてきた。現在、リチウムイオン二次電池は、自動車搭載電源、電力貯蔵などの用途にも使用することが見込まれている。これらの用途では、より高電流密度の使用が想定され、高い充放電効率、電極表面の安定性が重要な課題になる。炭素材料をリチウムイオン二次電池の負極材料として用いるときには、その表面特性制御が重要である。初回充電時には、炭素負極表面に保護皮膜（Solid Electrolyte Interphase [SEI]）を形成するために電力が消費され、充電した電気量のうち取り出すことのできない部分（不可逆容量）となる。この保護皮膜は黒鉛表面と電解液の反応によって形成されるため、炭素材料の表面特性に依存する。新しい電極表面修飾法は、リチウムイオン二次電池の利用拡大に大いに寄与することが期待される。

## ６．２　球状フェノール樹脂のプラズマ炭化反応により得た多孔質炭素粉末

熱プラズマ中に、球状フェノール樹脂粉末（平均粒径 25μm）を供給してプラズマ処理を行うと、プラズマ加熱による炭素化の進行により、炭素含有量は 99wt.% 以上にまで大きくなった[1]。Fig.6.1 に粒子断面のＳＥＭ写真を示す。プラズマ処理粉末の粒子内部は多孔性であり、通常の熱処理炭素粒子が緻密な構造をとるのは大きく異なる内部構造であった。多孔度は中心付近で特に高く、粒子表面に向かって小さくなっている。また、粒子の中心付近と表面近傍では結晶性も異なり、電子線回折および顕微ラマン分光法で調べた結果はともに、表面近傍で結晶性が高くなることを示した。この炭素粉末のリチウム二次電池負極材としての特性は、充放電効率におとるものの、グラファイトの理論容量を上回る容量を示すものも見られた。

高分子を焼成して得られる炭素材料には、原料由来の水素や酸素などが残存しており、表面には、水酸基、カルボニル基、あるいはカルボキシル基といった官能基が残存している。従って、炭素材料のリチウム二次電池負極材料としての特性は、このような残存異種原子や表面の状態により大きな影響を得ると考えられる。フェノール樹脂を約 1,000℃で炭化した球状グラッシーカーボン粉末（平均粒径、14 μm）の高周波熱プラズマ処理では、プラズマ組成に対応した表面組成、表面モルフォロジーの変化がはっきりと見られた[2]。リチウムイオン二次電池の負極として放電容量は原料グラッシーカー

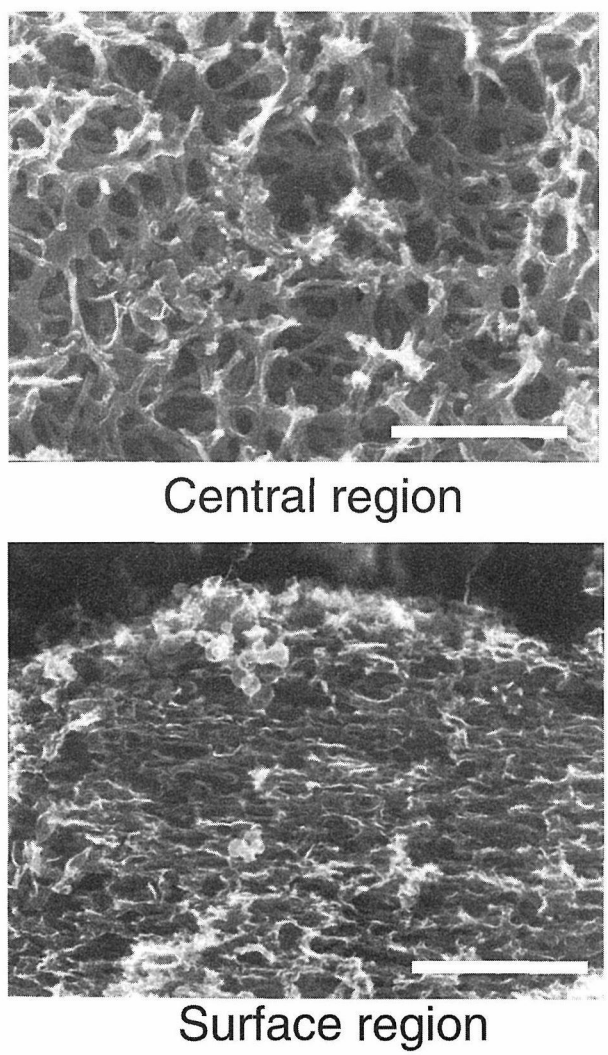


Fig.6.1 Cross-sections of plasma-synthesized carbon powders from phenoric resin (Bars in figures correspond to 500nm).

ボン粉末と比較して増加しており、特に、アルゴン-窒素プラズマ処理試料では原料の約2.5倍の容量が得られた[3]。また、充放電を繰り返したときのサイクル特性も良好であった。

## 6．3　メソカーボンマイクロビーズ粉末のプラズマ処理

代表的な人造黒鉛として知られているメソカーボンマイクロビーズ（MCMB）粉末は、粒径10μm程度の球状粒子からなる。黒鉛化度がもともと高いので、プラズマ中に供給して加熱してもそのバルク構造は変化しない。粒子はグラファイトナノ構造の積層によるラメラ構造をもっているが、プラズマの化学作用（制御した酸化作用）により、グラファイト積層方向に垂直なグラファイト端面の粒子表面露出が増加する[3]。また、プラズマ中の窒素、酸素などヘテロ原子により、数百nmの表面層で化学組成が修飾される。その結果、充放電容量・効率の増加など電気化学特性の向上、電解質溶液との反応による安定界面相の形成による安全性の改良などが可能になった[4]。さらに、MCMBをイオウ、フッ素を含む反応性熱プラズマで処理した黒鉛粉末の処理前後の表面構造、化学組成の変化、およびその電気化学特性への影響を検討した。特に、MCMBをイオウ、フッ素を含む反応性熱プラズマで処理すると、黒鉛粉末の処理前後の表面構造、化学組成が大いに変化し、その負極特性が大いに向上する[5),6)]。　Fig.6.2に、原料MCMB粒子、プラズマ処理粒子のＳＥＭ写真を示す。原料粒子は、黒鉛構造の積層を示すラメラ状表面形態を見せている。一方、エッチング効果の高いフッ素を含むプラズマで処理した粒子表面は多孔形状となった。X線回折法によると、プラズマ処理前後、高結晶性炭素粉末の構造は変化しなかった。ラマンスペクトルは表面の結晶性の違いを示し、プラズマ処理により粒子表面が乱層構造化したことがわかった。イオウ、フッ素の炭素粒子に溶解、さらに、表面形態に対応したBET比表面積の増加が認められ、プラズマ処理による多様な表面改質が確認できた。

プラズマ処理MCMB粉末をリチウムイオン電池の負極に応用すると、放電容量が最大13％増加し、初期充放電効率も向上した。電極－電解液界面制御法の異なったアプローチとして、イオウを含む電解液を用いるとSEIの厚みが変化し、充放電特性が向上するという報告もあるので、負極特性の向上にはイオウおよびフッ素の溶解が有効であり、SEI生成反応や電気化学特性

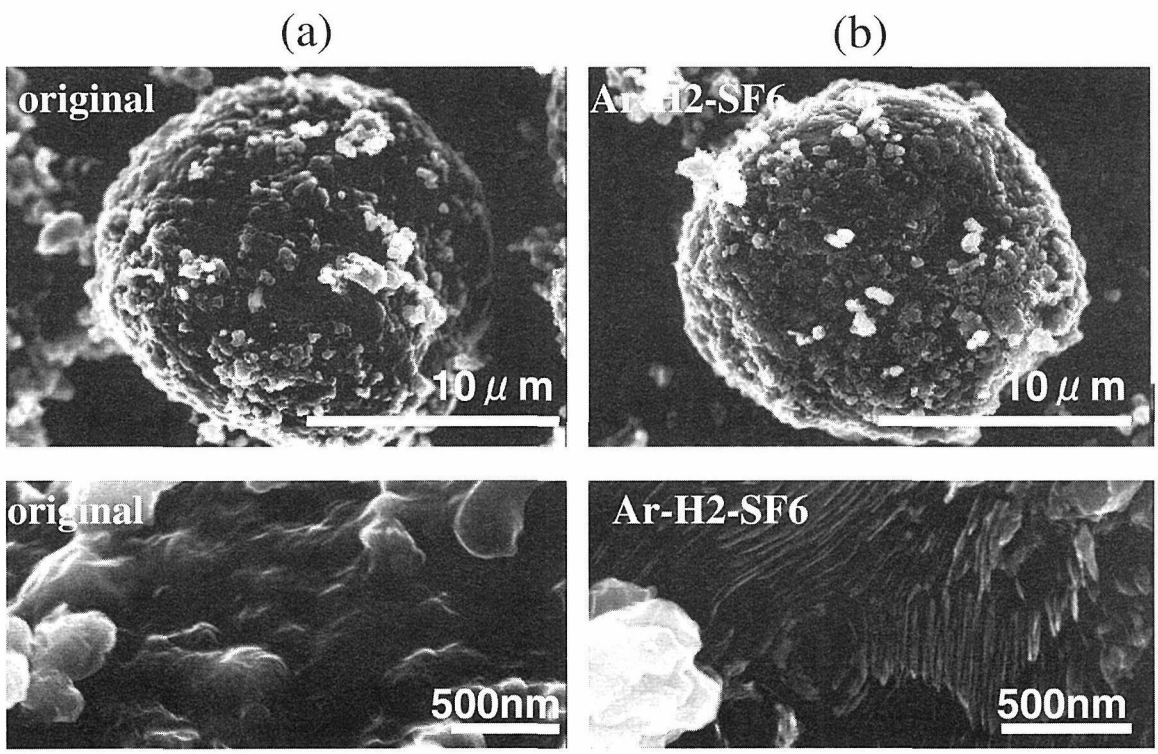


Fig.6.2 Surface morphology in MCMB particles; (a) original powder, (b) Ar-$H_2$-$SF_6$ plasma-treated powder.

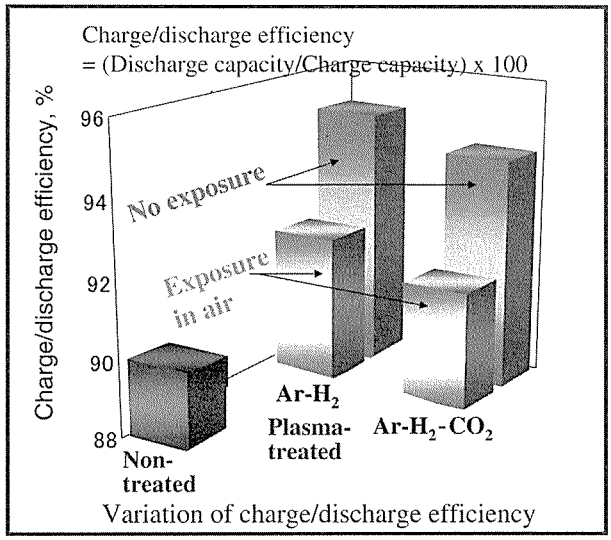


Fig.6.3 Change of charge/discharge efficiency for various plasma compositions and post-plasma treatment.

に影響していることが示唆された。さらに、炭素粒子表面への水蒸気の吸着を抑制することにより、充放電容量・効率の増加など電気化学特性の向上(Fig.6.3)、電解質溶液との反応で形成される安定界面相に起因する安全性の改良などがもたらされた[7]。

## References


1) 丸山哲, 栗原雅人, 石垣隆正, 渡邊賢司, 滝澤利雄, 守吉佑介, *日本化学会誌*, **2002**, 27.
2) 丸山哲, 栗原雅人, 石垣隆正, 菱田俊一, 佐藤洋一郎, 無機マテリアル, **8**, 37 (2001).
3) M. Kurihara, S. Maruyama, K. Oh'e and T. Ishigaki, *Chem. Lett.*, **27**, 715(1998).
4) H. Tanaka, T. Osawa, Y. Moriyoshi, M. Kurihara, S. Maruyama, T. Ishigaki and H. Kanda, *Thin Solid Films*, **435**, 205 (2003).
5) H. Tanaka, T. Osawa, Y. Moriyoshi, M. Kurihara, S. Maruyama, and T. Ishigaki, *Thin Solid Films*, **457**, 209(2004).
6) J.-Y. Xu, H. Tanaka, M. Kurihara, S. Maruyama, Y. Moriyoshi, and T. Ishigaki, *J. Power Sources*, **133**, 260(2004).
7) H. Tanaka, J.-Y. Xu, M. Kurihara, S. Maruyama, N. Ohashi, Y. Moriyoshi, T. Ishigaki, *Carbon*, **42**, 3229(2004).

# 第７章　溶液プロセスを利用した酸化チタンナノ粒子合成

$TiO_2$ has three naturally occurring crystalline modifications: anatase, brookite, and rutile. All the three crystal structures are built up of $TiO_6$ octahedra, but in different ways. In rutile (tetragonal), two opposing edges of each octahedron are shared to form linear chains along the [001] direction, and the $TiO_6$ chains are linked to each other via corner connection. Anatase (tetragonal) has no corner sharing, but has four edges shared per octahedron. In brookite (orthorhombic), on the other hand, the octahedra share 3 edges and also corners.[1)]

Anatase and rutile are the common polymorphs of synthetic $TiO_2$ while brookite is the most difficult to obtain in its pure form. Actually brookite was reported to be a high-pressure phase and was classically obtained from aqueous or organic media as large crystals via hydrothermal treatment at high temperature (such as 300°C). Even under such hydrothermal conditions, particular amounts of alkaline ions seem indispensable.[2,3)] The properties of $TiO_2$ are closely related to its crystal structure, which makes phase selective synthesis one of the most important issues in the practical application of the material.

Previous work on $TiO_2$ synthesis almost exclusively started with titanium (IV) compounds, namely tetrachloride ($TiCl_4$) and alkoxides, which are highly sensitive to atmospheric moisture and therefore requires special precautions. We have used titanium trichloride ($TiCl_3$) solution, which is not moisture sensitive and easily manipulatable, as a staring material for $TiO_2$ preparation, and phase pure anatase, brookite, and rutile nanocrystallites were obtained under mild hydrothermal conditions (180°C, up to 3h).

The synthesis of $TiO_2$ from Ti(III) salts requires oxidation reactions, and the oxidants used here are ammonium peroxodisulfate ($(NH_4)_2S_2O_8$), hydrogen peroxide ($H_2O_2$), perchloric acid ($HClO_4$) and nitric acid ($HNO_3$). In all the cases, the $TiCl_3$/oxidant molar ratio was kept at 1, while total volume of the reaction system was set at 80 mL. Whenever necessary, ammonia water or urea was used as a pH adjustor. The hydrothermal treatment was performed without stirring at 180°C for 3 h. Two categories of results were obtained with this redox-hydrothermal strategy: (1) only the anatase polymorph was obtained with ammonium peroxodisulfate as the oxidant, irrespective of solution pH and concentration of the titanium trichloride solution, (2) almost identical results were obtained when hydrogen peroxide, perchloric acid, and nitric acid were employed as the oxidants. In this case, anatase, brookite, and rutile can all be obtained in their phase pure form, through carefully controlling the reaction kinetics by varying the solution pH and reactant concentration.

Figure.7.1 shows TEM morphologies of the anatase particles obtained with $(NH_4)_2S_2O_8$ as the oxidant. Spherical-shaped particles with worm-hole structures were formed under a high $TiCl_3$ concentration of 0.9 mol/L (pH<0, Fig.7.1a). The particles were composed of nanocrystallites sized up to ~4 nm. The powder has a high specific surface area of 297$m^2$/g. With decreased $TiCl_3$ concentration, more discrete but bigger (though <10nm) anatase nanocrystallites were formed (0.15 mol/L, pH=0.75, Fig.7.1b, specific surface area: 134$m^2$/g). The redox reaction between $Ti^{3+}$ and $S_2O_8^{2-}$ ions generates $Ti^{4+}$ and $SO_4^{2-}$. $Ti^{4+}$ undergoes strong hydrolysis in an aqueous solution to form $[Ti(OH)_xX_y^m(H_2O)_{6-x-y}]^{4-x-my}$ (X: a complexing ligand, *m*: valence

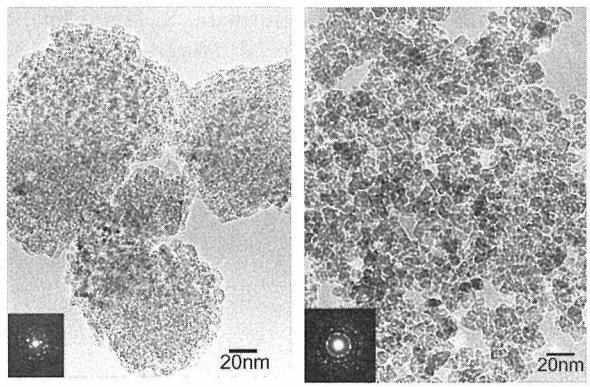


(a)　(b)

Fig.7.1 Morphologies of the anatase particles (TEM)

of X) species due to its high charge/radius ratio. $TiO_2$ nanoparticles are formed via olation and oxolation of the further hydrolyzed species. $SO_4^{2-}$ plays at least two roles here: (1) strongly complexing the hydrolyzed titanium species (due to its high minus charge). Its big ligand field was believed to alter the orientation of $[Ti(OH)_xX_y{}^m(H_2O)_{6-x-y}]^{4-x-my}$, favoring anatase formation, (2) strongly absorbed onto surfaces of the positively charged $TiO_2$ particles, retarding the particle growth via mass diffusion and hence yielding finer crystallites at higher $SO_4^{2-}$ concentrations (Fig.7.1a).

Figure.7.2 shows typical morphologies of the anatase, rutile, and brookite nanocrystals obtained with $H_2O_2$ as the oxidant. Notice the distinctly different particle shapes: rounded for anatase, rod-like for rutile, while plate-like for brookite. Further analysis indicates that the rutile nanorods are grown along the [001] direction (*c*-axis). A thorough investigation has been made to elaborate the correlations between processing parameters and phase structure of the final products. It was identified that anatase is easily formed under high $[TiCl_3]$ and high pH conditions, rutile under highly acidic conditions, while brookite intermediate $[TiCl_3]$ and pH conditions. The Phase selection of $TiO_2$ polymorphs largely depends upon reaction kinetics, which is influenced by processing parameters, that is, the solution pH and $[TiCl_3]$ here.

From the view point of $TiO_2$ crystal structure, as mentioned earlier, anatase has 4 edges shared per octahedron, brookite has 3, while rutile 2. The formation of one edge sharing requires two dehydration reactions among the $[Ti(OH)_xX_y{}^m(H_2O)_{6-x-y}]^{4-x-my}$ species, while one corner sharing needs only one dehydration reaction. Based upon these facts, the effects of solution pH and $[TiCl_3]$ are discussed as follows:

- the effects of pH (fixed $[Ti^{3+}]$)

(1) The higher the pH, the more OH in $[Ti(OH)_xX_y{}^m(H_2O)_{6-x-y}]^{4-x-my}$, and therefore more chance of edge sharing, favoring anatase. Oppositely, lower pH favors rutile. Brookite is midway in crystal structure between anatase and rutile, which needs intermediate pH to stabilize.

(2) under high pH conditions, rapid aggregation of $[Ti(OH)_xX_y{}^m(H_2O)_{6-x-y}]^{4-x-my}$ favors metastable anatase; very slow hydrolysis (under low pH) favors stable rutile, which might be formed via dissolution/recrystallization or direct precipitation. In this context, intermediate reaction rate (under intermediate pH) stabilizes the brookite polymorph.

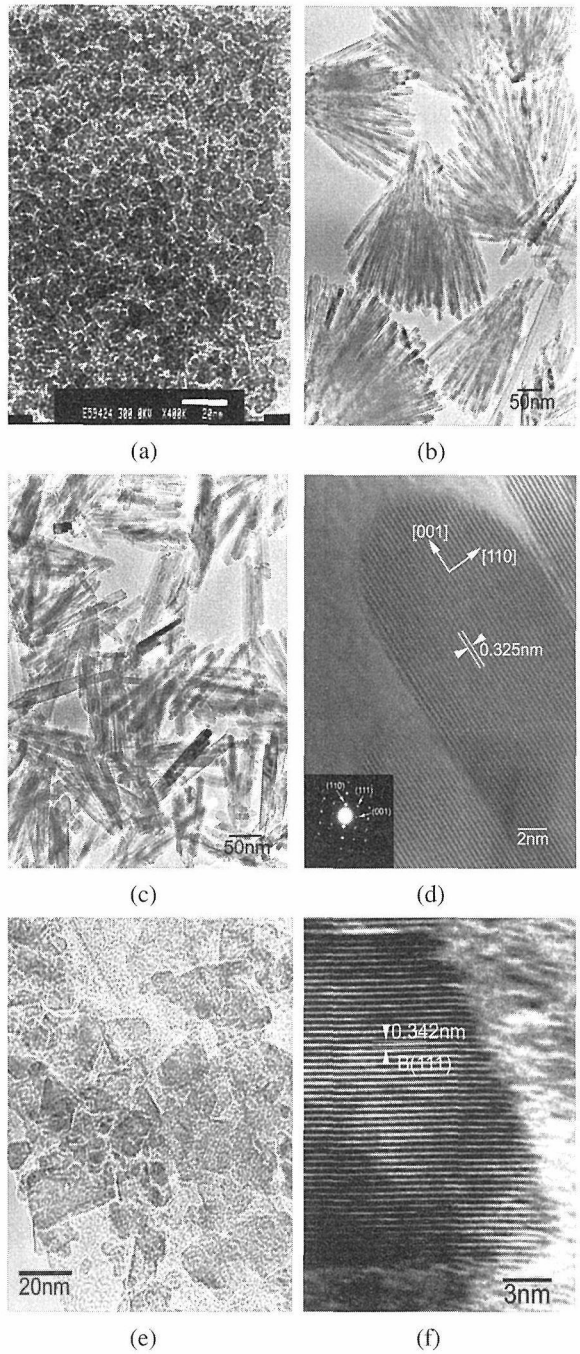


Fig.7.2 Morphologies of the anatase (a), rutile (b,c,d) and brookite (d, e) nanocrystallites. Synthesis conditions are (a): $[TiCl_3]$=0.0625 mol/L, pH=9.0; (b): $[TiCl_3]$=0.9 mol/L, pH<0; (c): $[TiCl_3]$=0.0625 mol/L, pH=0.44; (e): $[TiCl_3]$=0.0625 mol/L, pH=1.32. The powders of (a), (b), (c), and (e) have specific surface areas of 187, 47, 67, and 84$m^2$/g, respectively. (d) and (f) are lattice images of (c) and (e), respectively.

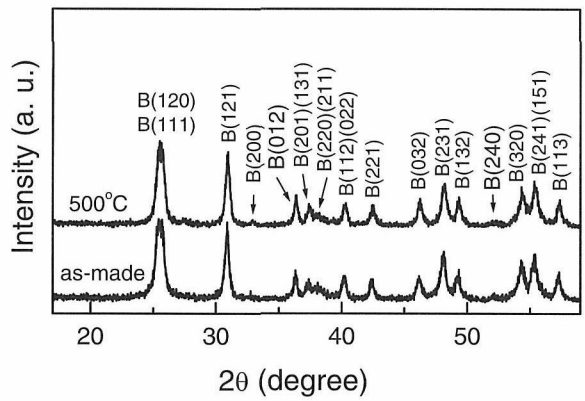


Fig.7.3 XRD patterns of the as-made brookite powder and that annealed in air at 500°C for 2 h.

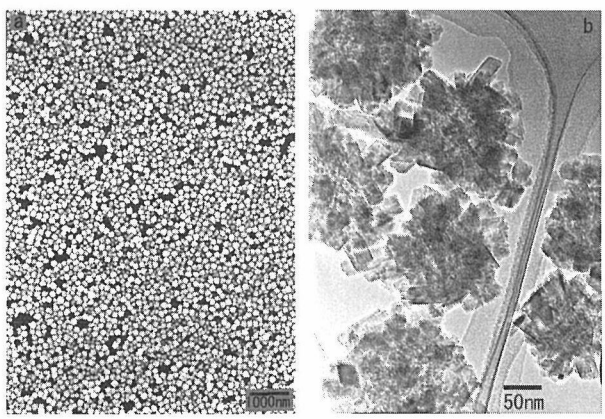


Fig.7.4 SEM (a) and TEM (b) micrographs showing morphologies of the brookite particles obtained via reacting a mixed solution of $TiCl_3$ and urea in open air.

• the effects of $[Ti^{3+}]$ (fixed pH)

Higher $[Ti^{3+}]$ promotes the rapid aggregation of $[Ti(OH)_xX_y^m(H_2O)_{6-x-y}]^{4-x-my}$, enhancing anatase formation. Under extremely low $[Ti^{3+}]$, the growth/nucleation ratio of crystals will decrease. Anatase is more stable at sizes <11 nm,[4] and hence brookite crystals below this critical size of ~11 nm might transform to anatase. Therefore the brookite phase tends to form under intermediate $[Ti^{3+}]$ conditions.

The speculation, that is, it is the reaction kinetics and not pressure is crucial to brookite formation, was supported by our experimental results obtained under ambient pressure. By reacting in open air a mixed solution of $TiCl_3$ (0.015mol/L) and urea (0.5mol/L) at 90°C for 2 h, phase pure brookite (Fig.7.3) of high particle uniformity was obtained directly (Fig.7.4a).[5] Here the atmospheric oxygen serves as the oxidant for $Ti^{3+}$ ions. Again, the primary brookite nanocrystallites exhibit a plate-like morphology (Fig.7.4b). The brookite phase was found stable against annealing up to about 500°C, and above which a direct transition to rutile occurs.[6]

## References


1) A. F. Wells, *Structural Inorganic Chemistry*. Oxford: Clarendon Press, 1975.

2) Y. Zheng, E. Shi, S. Cui, W. Li, and X. Hu, *J. Am. Ceram. Soc.*, **83** [10] 2634 (2000).

3) H. Kominami, M. Kohno, and Y. Kera, *J. Mater. Chem.*, **10**, 1151 (2000).

4) H. Zhang and J.-F. Banfield, *J. Phys. Chem. B*, **104**, 3481 (2000).

5) J.-G. Li, C. Tang, D. Li, and T. Ishigaki, *J. Am. Ceram. Soc.*, **87** [7] 1358 (2004).

6) J.-G. Li and T. Ishigaki, *Acta Mater.*, **52**, 5143 (2004).

# 第８章　残された問題と将来への展望

物質の材料化をすすめるためのブレークスルーとして、その一つの形態がナノ粒子であるが、ナノ粒子の特性が必ずしも有効に引き出されていないのが現状である。本研究では、酸化物ナノ粒子の特性を有効に引き出すために、高度制御プラズマプロセスを用いて高結晶化、表面制御、非平衡組成導入、原子オーダーでの均質性をめざした。セラミックス材料のナノ粒子合成は、従来、主として溶液プロセスを中心として進められてきた。発光特性を例にとると、溶液合成酸化物ナノ粒子の機能化を妨げていた大きな理由として、低結晶性、表面に結合した水酸基による消光、不完全な組成制御（ドーピング濃度、表面偏析）などがあげられる。また、表面水酸基の存在は溶媒中への分散に大きな影響を与えることも知られている。

本研究では新たな試みとして、熱プラズマ中に液体原料の大きさ約 10μm のミスト（霧状液滴）を供給し、高い過飽和度をもつ気相からナノ粒子を合成した。熱プラズマのもつ１万度以上の高温、高化学反応性、内在する急冷プロセスを材料プロセスに有効に利用して、非平衡な形態、結晶構造、化学組成をもつナノ粒子を合成可能なことを示した。均質な混合金属液体プリカーサーを用いるので、賦活原子が表面偏析ではなく粒子内部に固溶し、原子オーダーで均質な高結晶性ナノ粒子が、一段プロセスで合成できた。また、高温域での核生成・成長を経て得られる熱プラズマ合成酸化チタンナノ粒子表面では、表面水酸基の濃度を極端に減らすことも可能である。

次のステップとして、酸化チタンナノ粒子を材料科学的見地から評価するとともに、構造体化して多機能性の付与するところまで一貫して行い、発展性の高い研究をめざすことが重要である。そのために、ナノ粒子の溶媒あるいは樹脂中への完全分散をキーワードとして展開をめざす。

プラズマ合成ナノ粒子を構造体化するためには、酸化チタンナノ粒子を高度分散した液滴を利用してインクジェット法によるマイクロパターン形成を試みる。この方法では、最近、金ナノ粒子を含む溶媒の噴射により 100nm を切る太さでパターン形成が行われ、LSI 用電極に応用可能なレベルに到達している。これに対し、表面特性のより複雑なセラミックスナノ粒子の分散はより複雑な問題を解決する必要がある。また、ナノ粒子を樹脂中に高密度に分散させる技術を考案し、粒子濃度と特性の関係を明らかにすることにより、ナノ粒子の応用範囲拡大につながる画期的な成果となることが期待される。

パルス波形の電力で駆動されるデュアルマグネトロンスパッタリング装置を用い、二酸化チタン薄膜が結晶化に要するプロセス温度を著しく下げることに成功した。この技術により無加熱のガラス基板、プラスチック基板上にアナターゼ構造に結晶化した光触媒活性を有する二酸化チタン薄膜を形成することができた。本技術をスケールアップし、実際の大面積ガラスコーティング用のスパッタリング装置へ展開することにより、汚れない窓ガラスの実現が期待でき、クリーニング作業の危険回避やクリーニングコストの大幅削減につながる。またプラスチック等の加熱に耐えない材料に対しても光触媒作用を付与することが可能になるため汚れないプラスチック材料から派生する多様な用途の開拓が期待される。

ナノクリスタルダイヤモンドは超硬度、低摩擦係数、優れた電界放出特性を有し、MEMS デバイス、バイオケミカルデバイス、各種コーティング材料、電界放出材料等への応用が考えられ、ナノテクノロジーを支える重要な基盤材料の一つになる可能性も高い。残された課題としては、ナノクリスタルダイヤモンド粒子の径を均一にする合成条件を見出し、物性や機能性の面でより応用の可能性の高い数 nm のナノクリスタルダイヤモンド粒子を合成することが挙げられる。低圧力であるが故の低核発生密度、低成長速度を克服して、デバイスへの応用に不可欠なナノクリスタルダイヤモンド連続膜の合成条件の最適化が必要となってくる。さらに、安定発生に成功し、特異な電子温度・密度を示している VHF プラズマのナノクリスタルダイヤ合成への適用も検討していく。

# 第９章　研究成果

## ９．１　オリジナル論文

1)

*J. Appl. Phys.*, **93**(5), 3120-3122 (2003)

**$Sp^2$ bonding distributions in nanocrystalline diamond particles by electron energy loss spectroscopy**

**K. Okada, K. Kimoto, S. Komatsu and S. Matsumoto**

Advanced Materials Laboratory, National Institute for Materials Science

Nanocrystalline diamond particles with 200 500 nm in diameter have been prepared in a 13.56 MHz low pressure inductively coupled $CH_4/CO/H_2$ plasma. The chemical bonding map was investigated by electron energy loss spectroscopy (EELS). The EEL spectrum shows a peak at 290 eV due to $\sigma$ states and the energy loss near-edge structure is similar to that of diamond. A slight peak appears at ~285 eV corresponding to $\pi^*$ states. The mapping of $sp^2$ states by $\pi^*$ peak reveals that $sp^2$-bonded carbons are identified around the 20–50 nm subgrains of nanocrystalline diamond particles at approximately 1 nm resolution.

2)

*Chem. Phys. Lett.*, **367**(5-6), 561-565 (2003)

**Core–shell micron-scale composites of titanium oxide and carbide formed through controlled thermal-plasma oxidation**

**Y.-L. Li and T. Ishigaki**

Advanced Materials Laboratory, National Institute for Materials Science

Core–shell structured micron-scale spheres of titanium oxide and carbide were prepared by the controlled in-flight oxidation of a powder of irregularly shaped titanium-carbide particles in an argon –oxygen thermal plasma. Mono-dispersed core–shell particles with rutile shells and TiC cores were formed by an intermediate-rate input of oxygen to the plasma gas. The partial oxidation of the TiC particles in the liquid phase was accompanied by spheroidization of the surface oxide melt, thus giving rise to a core–shell composite under rapid quenching. $TiO_2$–TiC core–shell composites have potential as new materials for roles such as light-scattering media, photo-catalysts, and electro-rheor ogicalfluids.

3)

*Mater. Sci. Eng. A*, **345**(1-2), 301-308 (2003)

**Incongruent vaporization of titanium carbide in thermal plasma**

**Y.-L. Li and T. Ishigaki**

Advanced Materials Laboratory, National Institute for Materials

Vaporization of TiC at the plasma high temperatures (4000–10 000 K) has been investigated by structural and compositional characterizations of the vapor-condensed products formed by Ar–$H_2$ and Ar–He heating followed by a thermodynamic calculation. An incongruent vaporization of TiC with preferential vaporization of titanium has been observed at higher temperatures, which is contrary to the behavior at lower temperatures observed previously. X-ray diffraction and chemical analysis revealed a significant reduction of carbon and correspondingly, a decrease of lattice parameters in the vapor-condensed product with respect to the starting TiC materials. The vapor-condensed products have a composition of $TiC_x$ ($x$=0.38–0.58) and the lattice parameters are in range of $a_0$=4.28420–4.30780 Å, depending on processing conditions. A calculation of equilibrium vaporization using Langmuir model shows that TiC vaporizes incongruently to Ti at high temperatures between 3150 and 4700 K, in agreement with the present experimental observations.

4)

*J. Mater.Res.***18**(5), 1149-1156 (2003)

**Monodispersed $Sc_2O_3$ precursor particles via homogeneous precipitation: Synthesis, thermal decomposition, and the effects of supporting anions on powder properties**

**J.-G. Li, T. Ikegami, T. Mori and Y. Yajima**

Advanced Materials Laboratory, National Institute for Materials Science

Monodispersed $Sc_2O_3$ precursor particles were synthesized by the urea-based homogeneous precipitation method, with an investigation into the effects of supporting anions ($NO_3^-$, $Cl^-$, and $SO_4^{2-}$) on powder properties. Characterizations of the powders were achieved by elemental analysis, x-ray diffractometry, Fourier transform infrared, differential thermal analysis/thermogravimetry, high-resolution scanning electron microscopy, and the Brunauer– mmett–Teller method. Unlike other rare earths, $Sc^{3+}$ does not precipitate as basic carbonate but instead forms hydrated $\gamma$–ScOOH from either nitrate or chloride solution. Particles of the hydrated $\gamma$–ScOOH are pumpkin-shaped (approximately 1.0 μm) and are made up of thin-platelike crystallites emanating from a common axis. The presence of complexing $SO_4^{2-}$ changes the reaction chemistry toward $Sc_2O_3$ powders, leading to basic sulfate [$Sc(OH)_{1.6}(SO_4)_{0.7} \cdot H_2O$] precursor particles having hexagonal morphology (approximately 10 μm in diameter and 0.5 μm in thickness). The hydrated $\gamma$–ScOOH directly converts to $Sc_2O_3$ by calcination at 400 °C or above, while the basic sulfate transforms to oxide at temperatures ≥900 °C via an amorphous state and a $Sc_2(SO_4)_3$ intermediate. The effect of $SO_4^{2-}$ on powder morphologies and reaction chemistry is discussed. Nanocrystalline $Sc_2O_3$ powders comprising monodispersed particles were obtained via thermal decomposition of the precursors.

5)

*J. Appl. Phys.***93**(10), 6386-6392 (2003)

**Passivation of active recombination centers in ZnO by hydrogen doping**

**N. Ohashi, T. Ishigaki, N. Okada, H. Taguchi, I. Sakaguchi, S. Hishita, T. Sekiguchi, and H. Haneda**

Advanced Materials Laboratory, National Institute for Materials Science

The effect of hydrogen doping on luminescence properties of ZnO was investigated. Hydrogen was incorporated in the ZnO crystal by irradiation with an inductively coupled plasma (ICP), in particular, the pulse modulated mode operation of ICP, and the luminescence spectra and hydrogen concentration of the resultant samples were analyzed. A hydrogenated region of 20–100 nm was formed at the sample surface by the irradiation and the concentration of hydrogen was $10^{17}$–$10^{18}cm^{-3}$. Hydrogen doping improved the ultraviolet emission efficiency of all the samples, and the degree of improvement depended on the initial state (impurity concentration) of the original samples. The most significant improvements were recorded for the sample lightly contaminated with Cu, Al, and Li. The correlation between impurity concentration and hydrogen doping effects is discussed from the viewpoint of charge transfer between hydrogen and the other impurities.

6)

*J. Am. Ceram. Soc.,* **86**(9), 1493-1499 (2003)

**Wet-chemical routes leading to scandia nanopowders**

**J.-G. Li, T. Ikegami, T. Mori and Y. Yajima**

Advanced Materials Laboratory, National Institute for Materials Science

Two wet-chemical routes have been used to synthesize $Sc_2O_3$ nanopowders from nitrate solutions employing ammonia water (AW) and ammonium hydrogen carbonate (AHC) as the precipitants. The precursors and the resultant oxides are characterized by elemental analysis, X-ray diffractometry, differential thermal analysis/thermogravimetry, high-resolution scanning electron microscopy, and Brunauer-Emmett-Teller analysis. Crystalline $\gamma$-$ScOOH \cdot nH_2O$ ($n \approx 0.5$) is the only phase obtained by the AW method. This phase dehydrates to $Sc_2O_3$ at ~400°C, yielding hard aggregated nanocrystalline $Sc_2O_3$ powders. Three types of precursors have been synthesized by the AHC method, depending on the AHC/$Sc^{3+}$ molar ratio (***R***): amorphous basic carbonate [$Sc(OH)CO_3 \cdot H_2O$]

at $R \leq 3$, crystalline double carbonate $[(NH_4)Sc(CO_3)_2 \cdot H_2O]$ at $R \geq 4$, and a mixture of the two phases at $3 < R < 4$. Among these precursors, only the basic carbonate shows spherical particle morphology, ultrafine particle size (~50 nm), and weak agglomeration. $Sc_2O_3$ nanopowders (~28 nm) with high surface area (~49 $m^2/g$) have been prepared by calcining the basic carbonate at 700°C for 2 h.

7)

*J. Appl. Phys.*, **93**(12), 8867-8875 (2003)

**Nonequilibrated situations of pulse modulated Ar–$H_2$ and Ar–$N_2$ thermal plasmas at atmospheric pressure**

**K. C. Paul[1], T. Ishigaki[2], J. Mostaghimi[3] and T. Sakuta[4]**

[1]Ushio Inc., R and D Center, Gotenba Laboratory, [2]National Institute for Materials Science, [3]Department of Mechanical and Industrial Engineering, University of Toronto, [4]Electrical and Computer Engineering, Faculty of Engineering, Kanazawa University

Atmospheric pressure inductively coupled thermal plasmas with pulsing mode are generated for 104 slpm standard liters per minute total flow rate of Ar–$H_2$ and Ar–$N_2$ mixtures (Ar 94% molar concentration) inside a torch of 55 mm inner diameter. The inverter-type power source of 22 kW maximum output supplied coil current of 1 MHz fundamental frequency at 17.3 kW level, and the coil current is modulated by an external pulsed signal to produce the desired pulse modulated plasmas. Spectroscopic measurements are carried out for the temporal radiation intensity and coil current intensity. In addition, a time-dependent, two-dimensional model, which works with coil current input, is solved by using the same coil current profile measured in the experiment. Experimental and theoretical results for 67% duty factor with 10 ms on-time are compared. The theoretical predictions are found comparable with the experimental findings although the theoretical time-dependent response is seen slower, especially over the time just after on-pulsation. An estimation of electron temperature helps to describe this discrepancy fairly adequately. Experimentally the shimmer current level is found to vary with gas composition as well as with on- and off-time of pulsing signal. Both the experimental and theoretical findings suggest that plasma responds slowly at any axial positions below midcoil compared to that at midcoil level.

8)

*J. Mater. Res.*,**18**(5), 1239-1246 (2003)

**Low-temperature preparation of dense 10 mol%-$Y_2O_3$-doped $CeO_2$ ceramics using powders synthesized via carbonate coprecipitation**

**Y. Wang[1], T. Mori[1], J.-G. Li[2], T. Ikegami[2], and Y. Yajima[2]**

[1]Eco-materials Research Center, National Institute for Materials Science, [2]Advanced Materials Laboratory, National Institute for Materials Science

A carbonate coprecipitation method was used for the facile synthesis of highly reactive 10 mol%-$Y_2O_3$-doped $CeO_2$ (20YDC) nanopowders, employing nitrates as the starting salts and ammonium hydrogen carbonate (AHC) as the precipitant. The AHC/$RE^{3+}$ (RE = Ce + Y) molar ratio ($R$) and the reaction temperature ($T$) significantly affect the final yield and precursor properties, including chemical composition and particle morphology. Suitable processing conditions are $T$ = 60 °C and $R$ = 2.5 to 10, under which precipitation is complete, and the resultant precursors show ultrafine particle size, spherical particle shape, and good dispersion. The thus-processed precursors are basic carbonates with an approximate formula of $Ce_{0.8}Y_{0.2}(OH)CO_3 \cdot 2H_2O$, which directly yield oxide solid solutions upon thermal decomposition at a very low temperature of approximately 400 °C. The 20YDC solid-solution powders calcined at 700 °C show excellent reactivity and were densified to >99% of theoretical via pressureless sintering at a very low temperature of 950 °C for 6 h.

9)

*J. Mater. Res.*, **18**(8), 1816-1822 (2003)

**Fabrication of transparent $Sc_2O_3$ ceramics with powders thermally pyrolyzed from sulfate**

**J.-G. Li, T. Ikegami and T. Mori**

Advanced Materials Laboratory, National Institute for Materials Science

Scandia ($Sc_2O_3$) is a ceramic material that shows interesting thermal and optical properties, but is difficult to grow as single crystals. As an alternative, in this work we fabricated polycrystalline $Sc_2O_3$ transparent ceramics via vacuum sintering, using powders thermally pyrolyzed at 1200 ° C from a scandium sulfate salt, $Sc_2(SO_4)_3 \cdot 7.8H_2O$, that we prepared. Characterization of the powders was achieved by differential thermal analysis/thermogravimetry, x-ray diffractometry, Brunauer-Emmett-Teller analysis, and field-emission scanning electron microscopy. Sintering behaviors of the $Sc_2O_3$ powders were studied in air via dilatometry. The sulfate salt transforms to oxide at temperatures ≥1000 °C, and the best pyrolysis temperature for transparent ceramics fabrication is 1200 °C, at which the resultant $Sc_2O_3$ powder is good in dispersion, ultrafine in particle size (~80 nm), and almost free from residual sulfur. Transparent ceramics were fabricated from this powder via vacuum sintering at 1625 °C or above. The ceramics sintered at 1700 °C for 4 h exhibit an in-line transmittance of approximately 56-58% in the visible light region at a sample thickness of 1.0 mm.

10)

*J. Electrochem. Soc.*, **150**(6), A665-A673 (2003)

**Electrolytic properties and nanostructural features in the $La_2O_3$-$CeO_2$ system**

**T. Mori[1], J. Drennan[2], Y. Wang[1], J.-H. Lee[3], J.-G. Li[4] and T. Ikegami[4]**

[1]Ecomaterials Center, National Institute for Materials Science, [2]Centre for Microscopy and Microanalysis, The University of Queensland, [3]School of Materials Science and Engineering, Seoul National University, [4]Advanced Materials Laboratory, National Institute for Materials Science

Doped ceria ($CeO_2$) compounds are fluorite-type oxides which show oxide ionic conductivity higher than yttria-stabilized zirconia in oxidizing atmosphere. As a consequence of this, considerable interest has been shown in applications of these materials for low or intermediate temperature operation of solid-oxide fuel cells (SOFCs). In this study, the effective index was suggested to maximize the ionic conductivity in $La_2O_3$-$CeO_2$ based oxides. The index considers the fluorite structure, and combines the expected oxygen vacancy level with the ionic radius mismatch between host and dopant cations. Using this approach, the ionic conductivity of this system has been optimized and tested under operating conditions of SOFCs. $La_xCe_{1-x}O_{2-\delta}$ ($x$ = 0.125, 0.15, 0.175, and 0.20), $(La_xSr_{1-x})_{0.175}Ce_{0.825}O_{2-\delta}$ ($x$ = 0.1, 0.2, and 0.4), and $(La_{1-x}Sr_{0.2}Ba_x)_{0.175}Ce_{0.825}O_{2-\delta}$ ($x$ = 0.03, 0.05, and 0.07) were prepared and characterized as the specimens with low, intermediate, and high index, respectively. The ionic conductivity was increased with increasing suggested index. The transmission electron microscopy analysis suggested that partial substitution of alkaline earth elements in place of La into Ce site contributes to a decrease of microdomain size and an improvement of conductivity. $(La_{0.75}Sr_{0.2}Ba_{0.05})_{0.175}Ce_{0.825}O_{1.891}$ with high index and small microdomains exhibited the highest conductivity, wide ionic domain, and good performance in SOFCs.

11)

*Sci. Technol. Advan. Mater.*, **4**, 213-220 (2003)

**Influence of nano-structural feature on electrolytic properties in $Y_2O_3$ doped $CeO_2$ system**

**T. Mori[1], J. Drennan[2], Y. Wang[1], G. Auchterlonie[2], J.-G. Li[3] and A. Yago[2]**

[1]Ecomaterials Center, National Institute for Materials Science, [2]Centre for Microscopy and Microanalysis, The University of Queensland, [3]Advanced Materials Laboratory, National Institute for Materials Science

Doped ceria ($CeO_2$) compounds are fluorite type oxides which show oxide ionic conductivity higher than yttria stabilized zirconia, in oxidizing atmosphere. As a consequence of this, considerable interest has been shown in application of these materials for 'low temperature operation (500–

650 °C)' of solid oxide fuel cells (SOFCs). In this study, $Y_xCe_{1-x}O_{2-\delta}$ ($x$=0.05, 0.1, 0.15, 0.2 and 0.25) fine powders were prepared using a carbonate co-precipitation method. The relationship between electrolytic properties and nano-structural features in the sintered bodies was examined. The micro-structures of $Y_{0.05}Ce_{0.95}O_{1.975}$, $Y_{0.15}Ce_{0.85}O_{1.925}$ and $Y_{0.25}Ce_{0.75}O_{1.875}$ as representative three specimens have been investigated in more detail with transmission electron microscopy (TEM). The big diffuse scattering was observed in the background of electron diffraction pattern recorded from $Y_{0.15}Ce_{0.85}O_{1.925}$ and $Y_{0.25}Ce_{0.75}O_{1.875}$ sintered bodies. This means that the coherent micro-domain with ordered structure is in the micro-structure. While $Y_{0.25}Ce_{0.75}O_{1.875}$ sintered body with low conductivity and high activation energy has big micro-domains, the micro-domain size in $Y_{0.15}Ce_{0.85}O_{1.925}$ with high conductivity and low activation energy was much smaller than that of $Y_{0.25}Ce_{0.75}O_{1.875}$. TEM observation gives us message that the size of coherent micro-domain with ordered structure would closely relate to the electrolytic properties such as conductivity and activation energy in the specimens. It was concluded that a control of micro-domain size in nano-scale in $Y_2O_3$ doped $CeO_2$ system was a key for development of high quality solid electrolyte in fuel cell application.

**12)**

*Sci. Technol. Advan. Mater.*, **4**, 229-238 (2003)

**Low-temperature fabrication and electrical property of 10 mol% $Sm_2O_3$-doped $CeO_2$ ceramics**

**Y. Wang[1], T. Mori[1], J.-G. Li[2] and Y. Yajima[2]**

[1]Eco-materials Research Center, National Institute for Materials Science, [2]Advanced Materials Laboratory, National Institute for Materials Science

Ten mol% $Sm_2O_3$-doped $CeO_2$ solid-solution (20SDC) powders have been synthesized via carbonate coprecipitation using ammonium hydrogen carbonate (AHC) and urea as the precipitants, respectively. Characterizations were achieved by elemental analysis, X-ray diffractometry, differential thermal analysis/thermogravimetry, and FESEM. An amorphous hydroxyl carbonate precursor $(Ce,Sm)(OH)CO_3 \cdot 2H_2O$ having nanosized (~10 nm) spherical particles was formed with AHC, while a mixture of crystalline $(Ce,Sm)_2(CO_3)_2(OH)_2 \cdot H_2O$ and $(Ce,Sm)_2O(CO_3)_2 \cdot H_2O$ phases exhibiting irregular particle morphologies was obtained with urea. Both the precursors convert to oxide solid solutions without any phase detected corresponding to $Sm_2O_3$ during calcination. The oxide powder processed via the AHC method can be sintered to >99% of the theoretical at a low temperature of 1200 °C, due to the good dispersion and ultrafine size (~15 nm) of the particles, while that from the urea method can only reach ~67.2% dense at the same temperature. Electrical conductivity of the densified ceramic was measured in air in the range 400–700 °C by the DC three-point method, and an activation energy of ~60.5 kJ/mol was derived from the experimental data.

**13)**

*J. Am. Ceram. Soc.*, **86**(6), 915-921 (2003)

**10-mol%-$Gd_2O_3$-doped $CeO_2$ solid solutions via carbonate coprecipitation: A comparative study**

**J.-G. Li, T. Ikegami, Y. Wang and T. Mori**

Advanced Materials Laboratory, National Institute for Materials Science

10mol% $Gd_2O_3$-doped $CeO_2$ solid solutions (20GDC) have been synthesized via carbonate coprecipitation using ammonium bicarbonate (AHC) and urea as the precipitants. The precursors and the resultant oxide powders were characterized via chemical analysis, X-ray diffractometry (XRD), Brunauer–Emmett–Teller (BET) analysis, and high-resolution scanning electron microscopy (HRSEM). Sinterabilities of the 20GDC oxides in air were studied by constant-rate-of-heating (CRH) sintering and the conventional ramp-and-holding sintering methods. The precursor processed by both methods is hydroxyl carbonate but shows quite different particle morphologies in the two cases. Highly sinterable 20GDC oxides that can be densified to >99% of the theoretical at 1050°C within 4 h have been obtained via the AHC method.

14)

*Thin Solid Films*, **442**, 32-35 (2003)

**Pulse mode effects on crystallization temperature of titanium dioxide films in pulse magnetron sputtering**

**T. Miyagi[1,2], M. Kamei[1], T. Ogawa[1,3], T. Mitsuhashi[1], A. Yamazaki[1,2] and T. Sato[3]**

[1]Advanced Materials Laboratory, National Institute for Materials Science, [2]Department of Resource and Environmental Engineering, School of Science and Engineering, Waseda University, [3]Department of Applied Physics and Physico-Informatics, Faculty of Science and Technology, Keio-Gijuku University

Pulse mode effects on the crystallization temperature and photocatalytic properties of $TiO_2$ films were investigated. $TiO_2$ films were deposited on silica glass substrates using a pulse magnetron sputtering apparatus in the unipolar and the bipolar pulse modes. X-Ray diffraction showed that in the bipolar pulse mode the rutile phase $TiO_2$ film grew at lower substrate temperature compared with the unipolar pulse mode. The photocatalytic activities obtained from the photoreduction of Ag ions at the surface of $TiO_2$ films indicated that the anatase phase $TiO_2$ films grown in the bipolar pulse mode had higher photocatalytic activity compared with those grown in the unipolar pulse mode. This suggests that the bipolar pulse mode is an effective technique to achieve higher photocatalytic activity of $TiO_2$ film.

15)

*Thin Solid Films*, **435**(1/2), 205-210 (2003)

**Improvement of electrochemical properties of MCMB powders through reactive ICP modification**

**H. Tanaka[1] , T. Osawa[1] , Y. Moriyoshi[1] , M. Kurihara[2] , S. Maruyama[2] , T. Ishigaki[3] , H. Kanda[3]**

[1]Department of Materials Science, Hosei University, [2]Research and Development Center, TDK Corporation, [3]Advanced Materials Laboratory, National Institute for Materials Science

Mesocarbon microbeads (MCMB) powders were treated in Ar-$H_2$ , Ar-$N_2$ , Ar-$H_2$-$CO_2$ , and Ar-$N_2$-$CO_2$ RF inductively coupled plasmas (ICP). Plasma treatment modified the surface morphology, structure, and chemical composition of the powders. The surface of the Ar-N plasma-treated particles was covered with a fine condensate, while the surface of Ar-$N_2$-$CO_2$ plasma treated particles became rough and had no condensate. The discharge capacity and first charge/ discharge efficiency of the plasma-treated MCMB powders was higher than those of the original one. Plasma modification of MCMB gave rise to an improvement of the electrochemical properties making it suitable for use as the anode of a lithium-ion rechargeable battery.

16)

*Thin Solid Films*, **435**(1/2), 252-258 (2003)

**Effect of additives on photocatalytic activity of titanium dioxide powders synthesized by thermal plasma**

**S.-M. Oh[1,2], S.-S. Kim[1], J.-E. Lee[1] , T. Ishigaki[2] , D.-W. Park[1]**

[1]Inha University, Department of Chemical Engineering, [2]Advanced Materials Laboratory, National Institute for Materials Science

$TiO_2$ nanopowder was synthesized from titanium tetrachloride in a thermal plasma reactor. To improve photocatalytic activity, silicon tetrachloride and iron (III) acetylacetonate were added to the plasma reactor. The photocatalytic activity of prepared pure $TiO_2$ (T-powder), Si-doped $TiO_2$ (ST) and Fe-doped $TiO_2$ (FT) powder was evaluated by photodegradation of acetaldehyde. Decomposition efficiency of T-powder under UV-light was increased with the content of anatase. A small amount of Si-dopant improved the photocatalytic activity, while excessive Si-dopant over 2% decreased the photocatalytic activity of ST-powder because of the reduction of active sites on the catalyst. FT-powder was tested for the photocatalytic activity under visible light and UV-light. Decomposition efficiency increased with the addition of Fe-dopant because of suppression of electron-holes recombination. However, excessive Fe-dopant by over 15% inhibited the crystallization of anatase

and acted as recombination center, leading to decrease the decomposition efficiency.

**17)**

*Appl. Phys. Lett.*,**83**(9), 1782–1784 (2003)

**Superior Schottky electrode of $RuO_2$ for deep level transient spectroscopy on anatase $TiO_2$**

**T. Miyagi, M. Kamei, T. Mitsuhashi, and A. Yamazaki**

Advanced Materials Laboratory, National Institute for Materials Science

An anatase $TiO_2$ film was epitaxially grown on a conductive Nb-doped single-crystalline $SrTiO_3$ (100) substrate by metalorganic chemical vapor deposition. $RuO_2$ Schottky electrode was fabricated on the epitaxial anatase film by reactive dc magnetron sputtering. The dark I–V and capacitance–voltage characteristics indicated the good rectification and thermal stability of the $RuO_2$/anatase junction. This $RuO_2$/anatase junction enables the stable measurements of deep level transient spectroscopy in the high-temperature region and is a promising Schottky electrode to examine the origins of deep levels in the band gap of anatase.

**18)**

*J. Am. Ceram. Soc.*, **86**(9), 1456-1463 (2003)

**Phase formation and microstructure of titanium oxides and composites produced by thermal plasma oxidation of titanium carbide**

**T. Ishigaki*[1], Y.-L. Li[1] and E. Kataoka[2]**

[1]Advanced Materials Laboratory, National Institute for Materials Science, [2]Showa Carbot Supermetals K. K.

The phase formation and microstructure of titanium oxides and composites produced by Ar–$O_2$ thermal plasma oxidation of titanium carbide powders were investigated in detail by X-ray diffraction (XRD) and transmission electron microscopy (TEM). Relationships between the phase compositions and microstructures of the oxides were established by combined structural and phase analyses, in correlation with synthesis conditions and phase formation mechanisms. It is revealed that vapor condensation favored the formation of anatase, which existed as smaller particles, while liquid/solid oxidation favored the formation of rutile, which appeared as larger particles or composites. A higher oxygen input in the plasma gases (Ar + $O_2$) enhanced the formation of anatase due to impeded oxidation and evaporation. A small amount of $Ti_4O_7$ and $Ti_3O_5$ was detected in the larger particles coexisting with rutile or TiC. These suboxides were formed as intermediates in solid oxidation of TiC or precipitated from the Ti-C-O melt during cooling. Furthermore, extensive cracks, dislocations and stresses were observed in the monolithic rutile and composites, in association with the rapid quenching in this high-temperature in-flight oxidation process

**19)**

*Jpn. J. Appl. Phys., Part 1*, **42**, 7025-7028 (2003)

**Comparative study of $TiO_2$ anatase epitaxial thin films grown by magnetron sputtering and metalorganic chemical vapor deposition**

**M. Kamei,[1] T. Miyagi,[1,2] T. Ogawa,[1,3] T. Mitsuhashi,[1] A. Yamazaki,[1,2] and T. Sato[3]**

[1]Advanced Materials Laboratory, National Institute for Materials Science, [2]Department of Resource and Environmental Engineering, School of Science and Engineering, Waseda University, [3]Department of Applied Physics and Physico-Informatics, Faculty of Science and Technology, Keio-Gijuku University

Thin films of $TiO_2$ anatase structure were heteroepitaxially grown on $SrTiO_3$(001) single crystalline substrates by direct current magnetron sputtering (DCSP) and metalorganic chemical vapor deposition (MOCVD). The DCSP-grown films always showed larger lattice constants than those of the MOCVD-grown films. The RBS measurements revealed a difference in the depth profiles of the misfit dislocations in the films, which was considered to be the origin of the larger lattice constants in the DCSP-grown films. A striking difference was also present in the photoluminescence

characteristics in MOCVD-grown films and DCSP-grown films; the photoluminescence peak originating from the self-trapping excitons observed in MOCVD-films disappeared in DCSP-films.

**20)**

*J. Vacuum Sci.Technol. A*, **21**(6), 1988-1992 (2003)

**Ion energy distributions and the density of $CH_3$ radicals in a low pressure inductively coupled $CH_4/H_2$ plasma used for nanocrystalline diamond deposition**

**K. Okada, S. Komatsu and S. Matsumoto**

Advanced Materials Laboratory, National Institute for Materials Science

Ion energy distributions (IEDs) and the density of $CH_3$ radicals ($n$) in a 13.56 MHz radio frequency (rf) low pressure inductively coupled $CH_4/H_2$ plasma used for nanocrystalline diamond deposition have been investigated with a quadrupole mass spectrometer. The energy distributions of positive ions were measured in a $CH_4/H_2$ plasma with 50 mTorr of the gas pressure at 500 W of the plasma input power, and were compared with those of an Ar plasma. We have found that the IEDs of $Ar^+$, $CH_4^+$, and $C_2H_5^+$ have a nearly monoenergetic peak, and a hump due to a small degree of capacitive coupling. The plasma potentials obtained from the peaks are consistent with the previously reported values measured with a Langmuir probe. On the other hand, the IEDs of $H^+$, $H_2^+$, and $H_3^+$ have a clear asymmetric double peak due to the modulation of rf driven glow discharge. The $n$ monotonously increases with increasing pressure. The $n$ indicates that $CH_3$ radicals are main precursors for the growth of nanocrystalline diamond. The estimated sticking coefficient of the $CH_3$ radical is comparable with the reported value.

**21)**

*Key Eng. Mater.*, **253**, 255-262 (2003)

**Synthesis of intra-particulate composite of $TiO_2$-TiC by thermal plasma oxidation of titanium carbide**

**T. Ishigaki and Y.-L. Li**

Advanced Materials Laboratory, National Institute for Materials Science

$TiO_2$-TiC composite particles have been synthesized by a controlled oxidation of TiC powders in an oxygen-argon thermal plasma. The composite particles generated by this process are featured by a core-shell structure consisting of TiC inclusions and rutile shells, appearing as mono-disperse spherical particles. Local pores or hollow structures are present in the particles, and may be generated by the evolution of $CO/CO_2$ gases at the oxygen front. The composite particles were formed by a liquid oxidation reaction that started at the particle surface with the oxidation front moving inwards the particles until the particles were quenched. The formation of the composite structure can be feasibly controlled by the oxygen input in the plasma sheath gases at a moderate oxygen flow rate. Because of the important functional properties of titanium oxide, such as the high photo-electronic conductivity and photo-catalysis activity, its composite with the refractory titanium carbide, which has a high thermal conductivity and high hardness, may generate new properties in this novel composite.

**22)**

*Electrochemistry*, **71**(12), 1078-1080 (2003)

**Influence of post-processing atmosphere on electrochemical properties of thermal plasma treated graphite particles**

**M. Kurihara[1], S. Maruyama[1], H. Tanaka[2], Y. Moriyoshi[2] and T. Ishigaki[3]**

[1]R&D Center, TDK Corporation,[2]Department of Materials Science, Hosei University, [3]Advanced Materials Laboratory, National Institute for Materials Science

A kind of artificial graphite particles, so called as mesocarbon microbeads (MCMB) particles was

treated in Ar-$H_2$ plasma atmosphere to create the functional surface, and to improve electrochemical properties of graphite particles. The electrochemical properties of plasma-treated MCMB particles and the influence of post-processing atmosphere on electrochemical properties were investigated as anode of lithium-ion rechargeable battery. The modification of surface morphology and structure by $H_2$ plasma treatment, and the protection of adsorbing species on the surface by controlling post-processing atmosphere of dry Ar lead to the improvement of the first charge/discharge efficiency and the reversible capacity.

**23)**

*粉体および粉末冶金*, **51**(2), 71-80 (2004)

**熱プラズマ法と機械的粉砕法により処理したMCMB粉末のリチウムイオン二次電池用負極材料特性**

田中　秀樹[1,3]、栗原　雅人[2]、丸山　哲[2]、大澤　達也[3]、守吉　佑介[3]、石垣　隆正[1]
[1]（独）物質・材料研究機構　物質研究所、[2]TDK（株）開発研究所、[3]法政大学工学部物質化学科

Mesocarbon microbeads (MCMB) powders, a kind of synthesized graphite powder, are treated in induction thermal plasmas of high temperature exceeding 10,000K and various reactive atmospheres. The plasma-treated powders are compared with mechanical-milled powders in a ball mill. The plasma-treatment and the mechanical-milling do not give rise to the further graphitization. The surface morphology of plasma-treated powders varies depending on plasma treatment atmospheres. The crystallinity difference in the surface region is revealed by Raman spectroscopy. Electrochemical measurements as anode for lithium-ion rechargeable battery are performed in non-aqueous solvents containing 1 M $LiClO_4$. Discharge capacity of the plasma-treated powders is larger than that of original MCMB powder. Especially, the first discharge/charge efficiency of the MCMB powders treated in the atmosphere containing $CO_2$ is higher than that of original MCMB powder. The mechanical-milled powder with the same surface area as plasma-treated powder possesses the lowered first discharge/charge efficiency and discharge capacity. The thermal decomposition reaction of lithiated graphite anodes is also investigated by differential scanning calorimetry (DSC). In DSC, the heat generation, which is associated with the formation of solid electrolyte interphase (SEI), depends on surface area of MCMB powders.

**24)**

*Thin Solid Films*, **457** (1), 186-191(2004)

**Preparation of pure rutile and anatase $TiO_2$ nanopowders using RF thermal plasma**

**S.-M. Oh and T. Ishigaki***
Advanced Materials Laboratory, National Institute for Materials Science

We synthesized pure rutile and anatase nanopowders using in-flight oxidation of titanium nitride powder in an r.f. thermal plasma reactor. The mechanism of the in-flight oxidation of TiN powder was elucidated, and the effects of oxygen and hydrogen input concentrations on phase composition and morphology were investigated. The characteristics of the synthesized powder were evaluated using X-ray diffraction, optical microscopy, scanning electron microscopy and Raman scattering spectroscopy. The phase composition depended mainly on the ambient oxygen concentration. At high oxygen concentrations, the anatase content increased to over 93%. Introducing hydrogen promoted the formation of oxygen-deficient rutile nanopowder, and pure rutile nanopowder averaging 50 nm in diameter was produced with excess hydrogen. The synthesized powder had good photocatalytic activity in the decomposition of aqueous methylene blue under visible light.

25)

*Thin Solid Films,* **457**(1), 209-216 (2004)

**Improvement of the anode performance of graphite particles through surface modification in RF thermal plasma**

**H. Tanaka[1,2], T. Osawa[1,2], Y. Moriyoshi[2], M. Kurihara[3], S. Maruyama[3] and T. Ishigaki[1]**

[1]Advanced Materials Laboratory, National Institute for Materials Science, [2]Department of Materials Science, Hosei University, [3]Device and Development Center, TDK Corp.

Mesocarbon microbeads (MCMB) powders, which are known to be highly crystallized carbon materials and have a mean particle size of 11 μm, were treated in RF thermal plasma. Through the plasma treatment, the surface morphology, structure, and chemical composition of the powder were modified. The plasma-induced modification made the surface of MCMB particles disordered, and gave rise to an improvement in the thermal stability and electrochemical properties of the powders, such as the discharge capacity and first charge/discharge efficiency. It also made the powders suitable for further use as an anode in lithium-ion rechargeable batteries. Powders obtained without air exposure showed further improvement in anode performance.

26)

*J. Power Sources,* **133** (2), 260-262 (2004)

**Influence of active surface on electrochemical properties of mesocarbon microbeads powders**

**J. Xu[1] H. Tanaka[1,2], M. Kurihara[3], S. Maruyama[3], Y. Moriyoshi[2] and T. Ishigaki[1]**

[1] National Institute for Materials Science, Advanced Materials Laboratory, [2] Department of Materials Science, Hosei University, [3] Device Development Center, TDK Corporation

Mesocarbon microbeads (MCMB) powders were treated in Ar–$H_2$–$SF_6$ radio frequency inductively coupled thermal plasma. The structure, chemical composition and related electrochemical property changes have been studied. The results demonstrated that the active surface area has a great influence on the electrochemical properties of MCMB powder, and the specific irreversible capacity loss decays non-linearly with the increase of active surface area.

27)

*J. Appl. Phys.,* **96**(1), 118-126 (2004)

**Modeling of an induction plasma under transient turbulent flow conditions**

**R. Ye[1], T. Ishigaki[1] and M. I. Boulos[2]**

[1]National Institute for Materials Science, Advanced Materials Laboratory, [2]Department of Chemical Engineering, University of Sherbrooke

A renormalization group (RNG) $k$-ε turbulence model was employed to investigate the role of turbulence for the transient behavior of the radio frequency induction plasma discharge. Time-dependent conservation equations for the plasma and turbulence under local thermal equilibrium (LTE) conditions were solved numerically in two-dimensional, axisymmetric coordinates. Responses of energy, momentum, and turbulence to steplike and pulsed power changes in an Ar-$H_2$ plasma with a hydrogen volume concentration of 10.9%, and a total gas flow rate of 104.0 slpm were studied. The corresponding Reynolds number at the inlet of the discharge cavity was 2667. The turbulence model was validated qualitatively by comparing the predicted results with experimental observations under pulsed power conditions. It is found the transient behavior of the plasma energy and momentum are mainly governed by radial convection, while that of the turbulence is primarily determined by axial convection. These gave rise to a 5–10 ms delay in the response of the turbulence lagging behind the temperature field, for sudden power changes, under current operating conditions. A comparison between the results predicted using the RNG $k$-ε turbulence model and those obtained using the laminar model indicates the presence of turbulence leads to a longer relaxation time of plasma. Under pulsed power conditions, the plasma temperature responds to power changes almost instantaneously, and it is always in a transient state. In contrast, variation in the relative turbulent viscosity is insignificant and it is concluded that the turbulence is in

a quasisteady state when the period of a pulse is between 10 and 15 ms. By comparing the predicted results with images obtained using a high-speed camera (0.67 ms/frame) under the same operating conditions, we found that the turbulence model predicted a more accurate transient behavior in terms of plasma volume and temperature than the laminar model does.

**28)**

*J. Electrochem. Soc.* **151**(8), H169-H173 (2004)

**Effect of postdeposition annealing on luminescence from zinc oxide patterns prepared by the electroless deposition process**

**N. Saito[1], H. Haneda[1], T. Sekiguchi[2], T. Ishigaki[1], and K. Koumoto[3]**

[1]Advanced Materials Laboratory, National Institute for Materials Science, [2]Nanomaterials Laboratory, National Institute for Materials Science, [3]Graduate School of Engineering, Nagoya University

ZnO micropatterns were synthesized site-selectively on self-assembled monolayer templates in an aqueous solution of zinc nitrate and dimethylamine-borane at 55°C by an electroless deposition process. The effects of postdeposition annealing on the luminescence properties were investigated. For the as-grown samples, broad visible-light emission (500-800 nm) was mainly observed. When the sample was annealed above 150°C, the intensity of the visible light luminescence decreases and the ultraviolet exciton emission (377 nm) was exhibited. The UV intensity peaked at 300°C. The change of the luminescence coincided with the decrease in the amount of $H_2O$ in ZnO, which was analyzed using thermal desorption spectroscopy and infrared spectroscopy. Patterned monochromatic UV cathodoluminescence imaging was demonstrated for microlines of the ZnO pattern for the sample annealed at 300°C.

**29)**

*J. Phys. Chem B.*,**108**(40), 15536-15542 (2004)

**Controlled one-step synthesis of nanocrystalline anatase and rutile $TiO_2$ powders by in-flight thermal plasma oxidation**

**Y.-L. Li and T. Ishigaki**

Advanced Materials Laboratory, National Institute for Materials Science

Highly crystallized $TiO_2$ nanocrystallites (10-50 nm in size) with controlled phase structures (anatase and rutile) were synthesized using a one-step process. Flying TiC micrometer-size powder was oxidized in Ar-$O_2$ and Ar-$H_2$-$CO_2$ plasmas with various configurations used for injecting oxygen into the reaction system. The oxide nanocrystallites formed were characterized by X-ray diffractometry, Raman spectroscopy, and high-resolution transmission electron microscopy. The $TiO_2$ nanocrystallites formed in the Ar-$O_2$ plasma consisted of isolated single-crystal particles of anatase with spherical shapes and rutile grains crystallized in a hexagonal morphology. The fraction of anatase increased greatly with the oxygen flow rate in the Ar-$O_2$ plasma. On the other hand, oxidation of the carbide in the Ar-$H_2$-$CO_2$ plasma gave exclusively pure rutile nanocrystallites, regardless of the $CO_2$ concentration. Injecting oxygen at the plasma tail greatly reduced the size of the nanocrystallites. These results suggest that both the size and the phase compositions of nanocrystalline $TiO_2$ can be controlled using this thermal plasma oxidation process.

30)

*Solid State Ionics*, **172**(1-4), 231-233 (2004)

**Influence of Ar-$H_2$-$SF_6$ plasma on the surface structure and electrochemical properties of mesocarbon microbeads**

**J.-Y. Xu[1], H. Tanaka[2], M. Kurihara[3], S. Maruyama[3], Y. Moriyoshi[2] and T. Ishigaki[1]**

[1]Advanced Materials Laboratory, National Institute for Materials Science, [2]Department of Materials Science, Hosei University, [3]Device Development Center, TDK Corp.

The influence of Ar-$H_2$-$SF_6$ plasma on the surface structure and electrochemical properties of mesocarbon microbeads (MCMB) was studied by treating MCMB with Ar-$H_2$-$SF_6$ radio-frequency inductively coupled thermal plasma. The results demonstrated that the plasma-induced surface modifications depend on the plasma conditions, especially the plasma pressure, and that the electrochemical properties of plasma-treated MCMB depend on the rate of $SF_6$ flow.

31)

*Plasma Chem. Plasma Process.*, **24**(4), 555-571 (2004)

**In-flight spheroidization of alumina powders in Ar–$H_2$ and Ar–$N_2$ induction plasmas**

**R. Ye[1,2], T. Ishigaki[2], J. Jurewicz[1], P. Proulx[1] and M. I. Boulos[1]**

[1]Department of Chemical Engineering, University of Sherbrooke, [2]Advanced Materials Laboratory, National Institute for Materials Science

In-flight spheroidization of alumina powders in Ar–$H_2$ ($H_2$–7.6%, vol/vol) and Ar–$N_2$ ($N_2$–13.0%, vol/vol) RF induction plasmas was investigated numerically and experimentally. The mathematical model for the plasma flows incorporates the k-ε turbulence model, and that for particles is the Particle-Source-in-Cell (PSI-Cell) model. Experimental results demonstrate that spheroidized alumina particles are produced in both Ar–$H_2$ and Ar–$N_2$ RF plasmas, with different particle size distributions and crystal phases. Agreement between the predicted and measured particle size distributions is satisfactory under high particle feed rate conditions, while the results obtained for the Ar–$H_2$ plasma are better than those for the Ar–$N_2$ plasma. The discrepancy occurring in low feed rate conditions suggests that particle evaporation is an important factor affecting the plasma–particle heat transfer.

32)

*Carbon*, **42**(15), 3229-3235 (2004)

**Anomalous improvement of the electrochemical properties of mesocarbon microbeads by Ar-$H_2$-$SF_6$ thermal plasma treatment**

**H. Tanaka[1,3], J.-Y. Xu[1], M. Kurihara[2], S. Maruyama[2], N. Ohashi[1], Y. Moriyoshi[3] and T. Ishigaki[1]**

[1]Advanced Materials Laboratory, National Institute for Materials Science, [2]Device Development Center, TDK Corp., [3]Department of Materials Chemistry, Hosei University

Highly graphitized mesocarbon microbead (MCMB) powders, which consist of spherical artificial graphite particles, were treated in Ar-H2-SF6 radio-frequency inductively coupled thermal plasma. The results of X-ray diffractometry, scanning electron microscopy, Fourier transform infrared spectroscopy, Raman spectroscopy, X-ray photoelectron spectroscopy, and element analysis showed that the plasma treatment greatly affected the surface structure and chemical composition of the MCMB powders. Sulfur and fluorine could be incorporated into the particle by treating them with plasma containing SF6, and this plasma modification improved the electrochemical properties of the powders. A lithium-ion rechargeable cell with a negative electrode of plasma-treated powder had a discharge capacity as much as 13% greater than that of a cell with a negative electrode of untreated powder, while its irreversible capacity loss (ICL) was as much as 9% less. The specific ICL calculated by dividing the ICL by surface area decreased as the BET surface area increased. Furthermore, a new plateau near 2V was added to the discharge curve by treating the MCMB powder with SF6 plasma but not by treating it with Ar-$H_2$, Ar-$N_2$, Ar$H_2$-$CO_2$, or Ar$N_2$-$CO_2$ plasmas. The

incorporation of sulfur and fluorine should be a key factor for the improvement of negative electrode characteristics.

**33)**

*粉体および粉末冶金*、**51**(10), 741-748 (2004)

**ZrC(O)-$Al_2O_3$ 複合セラミックスの常圧焼結挙動**

佐藤　仁俊[1]、石垣　隆正[2]、神谷　秀博[3]、守吉　佑介[4]

[1] 東海高熱工業㈱、[2] (独) 物質・材料研究機構物質研究所、[3] 東京農工大学大学院共生科学技術研究部、[4] 法政大学工学部物質化学科

Oxide carbide composites have excellent mechanical properties. However, the composites have not been so extensively applied to industrial use because of the difficulty in pressureless sintering of them. In our work, improvement of pressureless sintering of ZrC-$Al_2O_3$ composites is shown. Heating of bare green compact in an argon atmosphere gives a relatively low density of sintered bodies. The charge of lattice constant of the ZrC phase, and chemical composition of sintered bodies indicate the incorporation of oxygen into ZrC during firing. The oxygen-containing phase is chemically denoted as ZrC(O), in which oxygen atoms are dissolved into the ZrC of the NaCl type crystal structure. The incorporation is related to alumina evaporation during firing, that hinderes densification. We examine preserving of particle size of ZrC powder during mixing and the alumina encapsulation of specimens during firing to prevent evaporation of specimens and proceed the sintering. Addition of MgO leads to further improvement of sintered density, i.e., the relative density of ZrC25-$Al_2O_3$ 75 vol% composite exceeded 98%. We discuss the pressureless sintering behavior of ZrC(O)-$Al_2O_3$ composites comparing it with that of TiC(O)-$Al_2O_3$ composites as we previously reported.

**34)**

*Trans. Mater. Res. Soc. Jpn.*,**29**(8), 3395-3398 (2004)

**Influence of Water Adsorption on Electrochemical Performance of Plasma Modified MCMB Powders**

**H. Tanaka[1,3], Y. Moriyoshi[1], M. Kurihara[2], S. Maruyama[2] and T. Ishigaki[3]**

[1]Hosei University, Department of Materials Science, [2]TDK Corp,. R&D Center, [3]National Institute for Materials Science, Advanced Materials Laboratory

Mesocarbon Microbeads (MCMB) powders, which are known to be highly crystallized carbon materials and have a mean particle size of 11μm, were treated in RF thermal plasmas. Through the plasma treatment, the surface morphology, structure, and chemical composition of the powder were modified. The plasma-induced modification made the surface of MCMB particles disordered, i.e. the improvements in the thermal stability and electrochemical properties of the powders, such as the discharge capacity and first discharge/charge efficiency as an anode in lithium-ion rechargeable batteries. Powder obtained without air exposure showed further improvement in electrochemical performance as anode materials.

**35)**

*Trans. Mater. Res. Soc. Jpn.*, **29**(8), 3415-3418 (2004)

**Titanium dioxide nano-particles through thermal plasma oxidation of titanium nitride powders**

**T. Ishigaki[1], S.-M. Oh[1,2] and D.-W. Park[2]**

[1]Advanced Materials Laboratory, National Institute for Materials Science, [2] Department of Chemical Engineering, Inha University

Titanium dioxide nano-particles were synthesized by in-flight oxidation of micron-scale titanium nitride powders using inductive thermal plasma. The reaction was carried out initially by surface oxidation of titanium nitride, leading to core-shell composites with oxidized shells and titanium

nitride cores, followed by the gas phase synthesis of nano-sized titanium dioxide from vaporized species. At deficient oxygen content, the black colored shell was mainly made up of rutile and nano-sized powders solidified from vapor species co-existing with anatase and rutile. With an increasing oxygen flow rate, the micron sized composites were rapidly oxidized, simultaneously enhancing vaporization and size reduction. Spherical anatase crystals were obtained under excessive oxygen input conditions.

**36)**

*Jpn. J. Appl. Phys. Part 1*, **43**(2), 775-776 (2004)

**Photocatalytic property and deep levels of Nb-doped anatase $TiO_2$ film grown by metalorganic chemical vapor depostion**

**T. Miyagi,[1,2] M. Kamei,[1] I. Sakaguchi,[1] T. Mitsuhashi[1] and A. Yamazaki[1,2]**

[1]Advanced Materials Laboratory, National Institute for Materials Science, [2]Department of Resource and Environmental Engineering, School of Science and Engineering, Waseda University

A Nb-doped anatase $TiO_2$ (Nb: 5 at%) film was grown on a $SrTiO_3$(001) substrate by metalorganic chemical vapor deposition. Deep level transient spectroscopy analysis revealed that this film possessed two kinds of deep levels due to the Nb ions, which were found to exist at 0.32 eV and 0.67 eV below the bottom of the conduction band. The photocatalytic activity of this film was low compared with that of the undoped anatase film, suggesting that the deep levels acted as recombination centers of photoexcited electron-hole pairs.

**37)**

*Chem. Phys. Lett.*, **390**, 399-402 (2004)

**Charge separation at the rutile / anatase interface: a dominant factor of photocatalytic activity**

**T. Miyagi[1,2], M. Kamei[1], T. Mitsuhashi[1], T. Ishigaki[1] and A. Yamazaki[1,2]**

[1]Advanced Materials Laboratory, National Institute for Materials Science, [2]Department of Resource and Environmental Engineering, School of Science and Engineering, Waseda University

Epitaxial and polycrystalline anatase .lms were grown by pulse-powered magnetron sputtering. The photoreduction of Ag ions showed the di.erence in the distribution of the photocatalytic active sites in these .lms. The polycrystalline anatase .lm was covered with an Ag layer. In contrast, discrete Ag particles were interspatially deposited on the epitaxial anatase .lm. Evaluation of the epitaxial .lm by micro-Raman spectrometry revealed that the rutile coexisted at only the site where the Ag particle was precipitated. These results suggest that the rutile/anatase interface is the active site for photocatalysis and is one of the dominant factors of the photocatalytic activity.

**38)**

*Trans. Maater. Res. Soc. Jpn.*, **29**(8), 3423-3425 (2004)

**Comparative study of $TiO_2$ anatase epitaxial and polycrystalline thin films grown by magnetron sputtering**

**M. Kamei,[1,2] T. Miyagi,[1,2] T. Ogawa,[3] T. Mitsuhashi,[1,2] A. Yamazaki,[1,2] T. Sato[4] and T. Ishigaki[1]**

[1]Advanced Materials Laboratory, National Institute for Materials Science, [2]Department of Resource and Environmental Engineering, School of Science and Engineering, Waseda University, [3] School of Engineering, The University of Tokyo, [4]Faculty of Science and Technology, Keio-Gijuku University

Comparative study of Epitaxial and polycrystalline anatase $TiO_2$ films grown by magnetron sputtering has been performed in order to clarify the photocatalytic behavior of anatase material. Only the polycrystalline anatase film showed a well-defined photocatalytic activity and the epitaxial films (<001> and <204> oriented) hardly showed photocatalytic behavior despite the better crystalline quality compared with that of the polycrystalline film. It was revealed that the anisotropy in the effective mass and the surface roughness could be excluded from the major factor for

determining photocatalytic activity in this system. Since the major discrepancy between the epitaxial films and polycrystalline films is the existence of the grain boundaries, further study focusing on the grain boundary effects should be performed for the elucidation of the dominant factor for photocatalytic activity in this system.

**39)**

*Trans. Mater. Res. Soc. Jpn.*, **29**(8), 3427-3430 (2004)

**Preparation of nanocrystalline diamond in a low pressure inductivity coupled plasma**

**K. Okada, K. Kimoto, S. Komatsu and S. Matsumoto**

Advanced Materials Laboratory, National Institute for Materials Science

A 13.56 MHz low pressure inductivity coupled $CH_4/CO/H_2$ plasma has been applied to prepare nanocrystalline diamond particles with several hundred nm in diameter. The low loss region of electron energy loss spectra exhibits a bulk plasmon peak at 33 eV and a surface plasmon peak at 23 eV. The plasma diagnostics with a Langmuir probe reveals that the electron impact dissociation of CO brings about the decrease in electron density leading to the simultaneous increase in electron temperature and plasma potential.

**40)**

*J. Phys. Chem. B*, **108**(1), 205-211 (2004)

**Condensation of $sp^3$-bonded boron nitride through a highly nonequilibrium fluid state**

**S. Komatsu[1], K. Kurashima[1], Y. Shimizu[2], Y. Moriyoshi[3], M. Shiratani[4] and K. Okada[1]**

[1]Advanced Materials laboratory, National Institute for Materials Science, [2]National Institute for Advanced Industrial Science and Technology, Tsukuba Central1, [3]College of Engineering, Department of Materials Science, [4]Hosei University, Department of Electronics, Graduate School of Information Science and Electrical Engineering, Kyushu University

Exceptionally highly crystalline $sp^3$-bonded boron nitride showing Kikuchi lines in transmission electron diffraction was formed by pulsed laser vaporization deposition assisted with synchronously pulsated reactive plasma. Transmission electron microscopic observations indicated that a fluid-state precursor material was generated by the high-power nanosecond laser at 193 nm. Other $sp^2$- and $sp^3$-hybridized nanostructures with exceptionally wide variations in density, reflecting the original large density fluctuations, suggested that the precursor material was formed in the vicinity of the thermodynamic critical point (CP). These results as well as the exceptionally fast growth rates indicated a new mode of crystal growth, namely, the direct condensation of nonequilibrium-phase crystals from the fluid state near the CP.

**41)**

*J. Phys. Chem. B*, **108**(17), 5182-5184 (2004)

**Electron field emission from self-organized micro-emitters of $sp^3$-bonded 5H boron nitride with very high current density at low electric field**

**S. Komatsu[1], A. Okudo[2], D. Kazami[2], D. Golberg[1], Y.-B. Li[1], Y. Moriyoshi[2], M. Shiratani[3] and K. Okada[1]**

[1]Advanced Materials Laboratory, National Institute for Materials Science, [2]College of Engineering, Department of Materials Science, Hosei University, [3]Department of Electronics, Graduate School of Information Science and Electrical Engineering

Electron field emission with high current density ~0.9 A/cm$^2$ at a low electric field of 8.6 V/μm was achieved by self-organized cone-shaped emitters with dimensions on the order of ~10 μm made of $sp^3$-bonded 5H boron nitride, which was grown by plasma-assisted chemical vapor deposition with the assistance of 193 nm laser irradiation of the surface. The work function of this material proved to be ~5 eV, whereas the geometrical field enhancement factor amounts to ~$10^6$ cm$^{-1}$. The

known robustness of $sp^3$-bonded BN with its excellent electron emission characteristics and the self-organization of emitter shaped structures may provide new applications for electron emitting devices.

**42)**

*J. Mater. Res.* **19**(3), 733-736 (2004)

**Solution-based processing of $Sc_2O_3$ nanopowders yielding transparent ceramics**

**J.-G. Li, T. Ikegami and T. Mori**

Advanced Materials Laboratory, National Institute for Materials Science

A basic sulfate precursor [$Sc(OH)SO_4 \cdot 2H_2O$] for well-sinterable $Sc_2O_3$ powders was precipitated from mixed solutions of scandium nitrate [$Sc(NO_3)_3$] and ammonium sulfate [$(NH_4)_2SO_4$] at room temperature and which was subsequently converted to $Sc_2O_3$ via dehydroxylization and desulfurization at temperatures ≥900 °C. With the reactive powders synthesized in this work, polycrystalline $Sc_2O_3$ ceramics showing high inline transmittances of approximately 70% in the visible wavelength region (corresponding to ~90% of the theoretical value of single crystals) have been fabricated via vacuum sintering at a relatively low temperature of 1700 °C.

**43)**

*Acta Materialia*, **52**(8), 2221-2228 (2004)

**Low temperature processing of dense samarium-doped $CeO_2$ ceramics: sintering and grain growth behaviors**

**J.-G. Li[1], T. Ikegami[1] and T. Mori[2]**

[1]Advanced Materials Laboratory, National Institute for Materials Science, [2]Ecomaterials Research Center, National Institute for Materials Science

Samarium-doped $CeO_2$ is a leading electrolyte for applications in solid oxide fuel cells (SOFCs), which requires a typical sintering temperature of 1400 1600 °C. By synthesizing reactive powders via carbonate precipitation, fully dense $CeO_2$ ceramics doped with 0 20 at.% of samarium have been fabricated in this work via pressureless sintering at a significantly lowered temperature of 1000 °C. The resultant ceramics show ultrafine grain sizes of ~0.15–0.75 μm, depending upon the dopant concentration. Sintering studies indicated that samarium doping retards both densification and grain growth but increases the rate ratios of the two in the intermediate stage of sintering. Subsequent investigations on the grain growth in the fully densified ceramics also showed the suppressing effects of dopant, which tend to saturate at 10 at.% of samarium. The activation energy for grain growth increased from ~186 to ~254 kJ/mol by raising the samarium concentration from 5 to 20 at.%.

**44)**

*J. Am. Ceram. Soc.*, **87**(3), 517-519 (2004)

**Morphology change of undoped and sulfate-ion-doped yttria powders during firing**

**T. Ikegami,[1] J.-G. Li[1], I. Sakaguchi[1] and K. Hirota[2]**

[1]Advanced Materials Laboratory, National Institute for Materials Science, [2]Department of Molecular Science and Technology, Doshisha University

Morphologic changes that occurred during firing in undoped and sulfate-ion-doped yttria powders were examined in the present study. Clear scanning electron microscopy (SEM) images of uncoated insulators were achieved and charging of electrons was avoided by observing small samples, throughout which most of the electrons of the incident beam penetrated. SEM observation and firing of the samples were repeated several times. Searching the observed areas or particles started at low magnification, with the aid of photographs taken earlier. The sulfate-ion dopant inhibited volume diffusion and/or grain-boundary diffusion, and then particle growth of the sulfate-ion-doped yttria proceeded by surface diffusion or evaporation–condensation along with pore growth, which resulted

in collapse of the agglomerates of primary particles. Although most of the other particles exhibited slight pore growth along with particle growth at temperatures as low as 800°C, a hardening of the agglomerated particles, because of pore elimination by volume diffusion and/or grain-boundary diffusion, occurred at temperatures >850°C

**45)**

*J. Ceram. Soc. Jpn.*, **112**(5), S41-S45 (2004)

**Low-temperature synthesis of 10 mol% $Gd_2O_3$-doped $CeO_2$ ceramics and its characterization**

**Y. Wang[1], T. Mori[1], J. Drennan[2], J.-G. Li[3] and Y. Yajima[3]**

[1]Eco-materials Research Center, National Institute for Materials Science, [2] Centre for Microscopy and Microanalysis, The University of Qeensland, [3] Advanced Materials Laboratory, National Institute for Materials Science

10 mol% $Gd_2O_3$-doped $CeO_2$ solid-solution (20GDC) powders have been synthesized via carbonate coprecipitation using nitrates as the starting salts and ammonium hydrogen carbonate (AHC) as the precipitant. Characterizations were achieved by elemental analysis, XRD, DTA/TG, and FESEM. The thus-processed precursor is an amorphous hydroxyl carbonate with an approximate formula of $Ce_{0.8}Gd_{0.2}(OH)(CO_3)$ $2H_2O$, which directly yield oxide solid-solutions upon thermal decomposition at a very low temperature of approximately 430°C without any phase detected corresponding to $Gd_2O_3$. The 20GDC oxide powder calcined at 700°C shows excellent reactivity and were densified to >99% of the theoretical via pressureless sintering at a low temperature of 1150°C for 6 h. Electrical conductivity of the densified ceramic was measured in air in the range 400-700°C by the DC three-point method, and an activation energy of ~60.92 kJ/mol was derived from the experimental data.

**46)**

*J. Ceram. Soc. Jpn.*, **112**(5), S642-S648 (2004)

**Influence of nano-structural feature on electrolytic properties of Gd doped $CeO_2$ solid electrolytes**

**T. Mori[1], J. Drennan[2], Y. Wang[1], G. Auchterlonie[2] and** J.-G. Li[3]

[1]Ecomaterials Center, National Institute for Materials Science, [2]Centre for Microscopy and Microanalysis, The University of Queensland, [3]Advanced Materials Laboratory, National Institute for Materials Science

Doped ceria ($CeO_2$) compounds are fluorite type oxides which show oxide ionic conductivity higher than yttria stabilized zirconia, in oxidizing atmosphere. As a consequence of this, considerable interest has been shown in application of these materials for 'low (500°-650°C)' or 'intermediate (650°-800°C)' temperature operation of solid oxide fuel cells (SOFCs). In this study, the authors prepared $Gd_xCe_{1-x}O_{2-\delta}$ ($x$=0.1, 0.15, 0.21, and 0.25) and Gd/Sr co-doped $CeO_2$ [$(Gd_{0.8}Sr_{0.2})_{0.175}Ce_{0.825}O_{1.895}$] specimens using carbonate co-precipitation method, in order to examine the influence of nano-structural feature on electrolytic properties in the sintered bodies. And the relationship between the microstructural feature in nano-scale and the conducting property in those electrolytes were examined. A diffuse scatter was observed in the background of selected area electron diffraction pattern recorded from all sintered bodies. In addition, all specimens had extra spots in the selected area electron diffraction patterns recorded from sintered bodies. The diffuse scatter means that coherent micro-domain with ordered structure is in the lattice. Extra spots indicate the growth of micro-domain. From the comparison of calculated electron diffraction patterns between fluorite structure and b-type rare earth structure, it is concluded that the structure of micro-domain is distorted b-type rare earth structure or b-type related structure. From the observation of high-resolution transmission electron microscope (HR-TEM), it is concluded that the conducting property in Gd doped $CeO_2$ and Gd/Sr co-doped systems was strongly influenced by the size of micro-domain with ordered structure. The conductivity in $Gd_{0.21}Ce_{0.79}O_{1.895}$ sintered body with big micro-domain was lower than that in $(Gd_{0.8}Sr_{0.2})_{0.175}Ce_{0.825}O_{1.895}$ sintered body with small micro-domain. Therefore, the author concluded that domain control is a key for development of doped $CeO_2$ electrolytes.

47)

*J. Am. Ceram. Soc.*, **87**(6), 1008-1013 (2004)

**$Sc_2O_3$ nanopowders via hydroxyl precipitation: effects of sulfate ions on powder properties**

**J.-G. Li,[1] T. Ikegami,[1] T. Mori,[2] and Y. Yajima,[1]**

[1]Advanced Materials Laboratory, National Institute for Materials Science, [2]Eco-material Research Center, National Institute for Materials Science

Hydroxyl-type $Sc_2O_3$ precursors have been synthesized via precipitation at 80°C with hexamethylenetetramine as the precipitant. The effects of starting salts (scandium nitrate and sulfate) on powder properties are investigated. Characterizations of the powders are achieved by elemental analysis, X-ray diffractometry (XRD), differential thermal analysis/thermogravimetry (DTA/TG), high-resolution scanning electron microscopy (HRSEM), and Brunauer-Emmett-Teller (BET) analysis. Hard-aggregated precursors ( $\gamma$ -ScOOH·0.6$H_2O$) are formed with scandium nitrate, which convert to $Sc_2O_3$ at temperatures ≥400°C, yielding nanocrystalline oxides of low surface area. The use of sulfate leads to a loosely agglomerated basic sulfate powder having an approximate composition of $Sc(OH)_{2.6}(SO_4)_{0.2}\cdot H_2O$. The powder transforms to $Sc_2O_3$ via dehydroxylization and desulfurization at temperatures up to 1000°C. Well-dispersed $Sc_2O_3$ nanopowders (~64.3 nm) of high purity have been obtained by calcining the basic sulfate at 1000°C for 4 h. The effects of $SO_4^{2-}$on powder properties are discussed.

48)

*J. Am. Ceram. Soc.*, *87*(7), 1358-1361 (2004)

**Monodispersed spherical particles of brookite-type $TiO_2$: synthesis, characterization, and photocatalytic property**

**J.-G. Li, C.-C. Tang, D. Li, H. Haneda and T. Ishigaki**

Advanced Materials Laboratory, National Institute for Materials Science

Phase-pure brookite of high crystallinity, which was classically obtained via hydrothermal treatment, has been synthesized under ambient pressure at 70°C via reacting a mixed solution of urea and titanium (III) chloride (instead of the widely used titanium (IV) compounds). The resultant particles are monodispersed spheres (~154 nm) composed of brookite nanocrystals (~25 nm), which are stable in terms of phase purity and morphology up to ~500°C, above which a direct transition to rutile occurred. The as-made powder has a high specific surface area of ~41.2 $m^2/g$, which rapidly decreased to ~9.7 $m^2/g$ after transforming to rutile at 700°C. The brookite powder shows good catalytic property for the decomposition of acetaldehyde under UV radiation.

49)

*Acta Materialia*, **52**(17), 5143-5150 (2004)

**Brookite → rutile phase transformation of $TiO_2$ studied with monodispersed particles**

**J.-G. Li and T. Ishigaki**

Advanced Materials Laboratory, National Institute for Materials Science

$TiO_2$ is a polymorphic material (anatase, brookite, and rutile) of current interest for a variety of technological applications. Though the anatase → rutile transformation has been studied extensively, the brookite transition has rarely been addressed up to date due to the difficulties encountered in obtaining phase-pure brookite. The brookite → rutile transformation has been studied in this work using monodispersed quasi-spherical particles (~154 nm, composed of phase-pure brookite nanocrystals of ~25 nm) as a starting material. The transition mainly proceeds within the individual particles in the temperature range 500 600 °C, without the positive detection of the anatase polymorph. The transformation kinetics are best expressed by the "contracting spherical interface" model in the studied temperature range, from which an apparent activation energy of 143.4 ± 1.2 kJ/mol was derived. The rate parameter for the phase transition may be expressed as $k=1.28\times 10^4\exp(-17248 \pm 144/T)s^{-1}$.

50)

*Appl. Phys. A* **80**(4), 777–781 (2005)

**Effects of rf bias voltage and $H_2$ flow rate on the growth of cubic boron nitride films by chemical vapor deposition**

**J. Yu, S. Matsumoto and K. Okada**

Advanced Materials Laboratory, National Institute for Materials Science

Cubic boron nitride (cBN) films were deposited by rf bias-assisted dc plasma-jet chemical vapor deposition. Effects of H2 flow rate and bias voltage on the growth of the cBN films were investigated. High phase purity cBN(over 90%) can be obtained in a wide range of H2 flow rates of 5 10 sccm and bias voltages from –50 to –100 V. Nearly phase pure cBN films were deposited at a H2 flow rate of 10 sccm voltages of –60 V and –70 V. The deposited films were characterized by Raman spectroscopy, Fourier-transform infrared spectroscopy, and glancing angle X-ray diffraction. Raman peaks were observed for all the cBN films, which indicate a good crystallinity of the films.

51)

*J. Mater. Res.*, **20**(2), 529-537 (2005)

**Nanocrystalline $TiO_2$ powders synthesized by in-flight oxidation of TiN in thermal plasma: Mechanisms of phase selection and particle morphology evolution**

**S.-M. Oh, J.-G. Li and T. Ishigaki**

Advanced Materials Laboratory, National Institute for Materials Science

Titanium dioxide nanopowders were synthesized by in-flight oxidation of titanium nitride (TiN) in radio-frequency (rf) induction thermal plasma. The powders were characterized by x-ray diffraction, high-resolution transmission electron microscopy, field emission scanning electron microscopy, Raman spectroscopy, and optical microscopy to reveal the mechanisms of phase selection and particle morphology evolution. The reaction began with surface oxidation of TiN particles, leading to the formation of core-shell composites with oxidized shells and TiN cores, followed by gas-phase condensation of $TiO_2$ nanoparticles. Phase selection of the resultant $TiO_2$ powders was found to largely depend on the oxidation potential of the thermal plasma rather than on the heat transfer itself. Anatase content of the products increased steadily with increasing the $O_2$ input, and $TiO_2$ nanoparticles (~50 nm) containing ~90% of anatase were obtained through $O_2$/Ar plasma treatment. Phase-pure rutile nanoparticles (~50 nm, on average) were also synthesized in $H_2$/Ar plasma injected with $O_2$ as the powder carrier gas.

52)

*Sci. Technol. Advan. Mater.*, **6**(2), 111-118, 2005

**Controlling the synthesis of TaC nanopowders by injecting liquid precursor into RF induction plasma**

**T. Ishigaki[1], S.-M. Oh[1,2], J.-G. Li[1] and D.-W. Park[2]**

[1]Advanced Materials Laboratory, National Institute for Materials Science, [2]Department of Chemical Engineering, Inha University

Thermal plasma processing has been used to synthesize nano-size powders through the condensation of reactant species from a vapor phase. Further development of this synthesis method will require the careful selection of an appropriate precursor and precise control of products species and their particle sizes. Direct introduction of liquid mist into thermal plasma gives us a wider choice of precursors than does vapor-phase precursor injection and lets us inject the precursors in larger amounts. In the present work, nano-size tantalum carbide powder was prepared from a liquid precursor, tantalum ethoxide $Ta(OC_2H_5)_5$, by using r.f. thermal plasma. The liquid precursor was atomized to generate micron-sized mist droplets, and the mist was introduced into plasma. This atomized precursor evaporated quickly in the high-temperature plasma flame, and nanoparticles were formed as temperature decreased. The process was controlled by changing the hydrogen addition, process pressure, carrier gas flow rate for mist injection, and quenching condition. Adding

hydrogen improved the powder quality by removing solid carbon, but excess hydrogen suppressed the formation of tantalum carbide. The quenching conditions gave significant effects on the reduction of particles size by two thirds and yielded average particle sizes as small as 8 nm.

**53)**

*Plasma Sources Sci. Technol.* **14**(2), 387-396 (2005)

**Controlled generation of pulse-modulated RF plasmas for materials processing**

**R. Ye[1], T. Ishigaki[1,3] and T. Sakuta[2]**

[1] Advanced Materials Laboratory, National Institute for Materials Science, [2] Department of Electrical and Electronic Engineering, Kanazawa University, [3] Author to whom any correspondence should be addressed.

Pulse-modulated radio frequency (RF) inductively coupled plasmas for materials processing applications were generated using a voltage-control-type power source, and the operating ranges for controlled generation were extended to sufficiently low shimmer power levels. When the plasma was generated at atmospheric pressure and a high power level of 17 kW, the low power level typically went down to about 4 kW for an Ar–$H_2$ plasma and 3 kW for an Ar–$N_2$ plasma, levels too low to sustain the continuous plasmas. The overshoot and undershoot at the beginnings of power change were reduced considerably by using an exponential voltage control signal. Spectroscopic measurements of the radiation intensity of the Ar atomic spectral line (751.5 nm) showed that the plasma temperatures varied with time and that the characteristic times of the plasmas depended on the operating conditions and the position in the plasma generator. The characteristic times in the discharge zone may be largely determined by the competition among ionization, recombination and convection in the pulsed plasmas. The characteristic times estimated using an electron transportation model are reasonably in line with those determined from measured emission intensities. The difference between the plasma properties at the higher and lower power levels was large enough to give rise to the nonequilibrium states at the instances of pulse-on and pulse-off, and to the increase in the concentration of chemically active radical species. This offers a unique physico-chemical condition for materials processing. The ranges of controlled generation were determined for the Ar–$H_2$ and Ar–$N_2$ plasmas at pressures from 27 to 101 kPa.

**54)**

*Chem. Phys. Lett.*, **407**(1-3), 209-212 (2005)

**Strain-induced charge separation in the photocatalytic single crystalline anatase $TiO_2$ film**

**M. Kamei[1], T. Miyagi[2] and T. Ishigaki[1]**

[1]Advanced Materials Laboratory, National Institute for Materials Science, [2]Research Center, Asahi Glass Co. Ltd.

A single crystalline anatase $TiO_2$ film was grown on a $LaAlO_3$ substrate. Photocatalytic reduction of Ag ions resulted in Ag precipitation on the surface of the film. The density and the morphology of the Ag precipitation varied at the twin boundaries of the substrate. The anatase film should suffer from the strain caused by this twinning and the strain distribution should be different in each twin domains. Hence, this twin-domain dependent Ag precipitation is a possible clue for the electron–hole charge separation centers induced by the stress concentration in the anatase film which act as active sites for photocatalytic reaction.

55)

*Mater. Sci. Eng.B*, **121**(1-2), 54-59 (2005)

**Reactive 10 mol% $RE_2O_3$ (RE = Gd and Sm) doped $CeO_2$ nanopowders: Synthesis, characterization, and low-temperature sintering into dense ceramics**

**J.-G. Li[1], Y. Wang[2], T. Ikegami[1], T. Mori[2] and T. Ishigaki[1]**

[1]Advanced Materials Laboratory, National Institute for Materials Science, [2]Eco-materials Research Center, National Institute for Materials Science

Nanoparticles of $CeO_2$ doped with 10 mol% of $RE_2O_3$ (RE = Sm and Gd) have been synthesized by the homogeneous precipitation method, employing nitrates as the starting salts and hexamethylenetetramine as the precipitant. Characterizations of the powders were achieved by elemental analysis, X-ray diffractometry (XRD), differential thermal analysis/thermogravimetry (DTA/TG), field-emission scanning electron microscopy (FE-SEM), and Brunauer–Emmett–Teller (BET). Sinterability of the powders was studied in air via dilatometry and isothermal sintering. Lightly hydrated crystalline solid solutions with the pre-determined stoichiometry were formed directly during precipitation, as were shown by the above characterization techniques and a leaching test with hydrochloric acid. The maximum doping level achieved by this synthetic procedure was found to be ~22 at.% for $Sm^{3+}$ and ~24.4 at.% for $Gd^{3+}$. The best annealing temperature for the powders intended for sintering is 400 °C, at which major dehydration has occurred without significant crystallite growth and hard-aggregates formation. Fully dense ceramics (>99%) with ultrafine microstructures (~117 134 nm) have been fabricated via pressureless sintering for 4 h at a low temperature of 1000 °C.

56)

*J. Appl. Phys.*, **97**(12), 123306 1-9 (2005)

**Modeling of transient nonequilibrium phenomena in an inductively coupled plasma under pulsed power conditions**

**R. Ye and T. Ishigaki**

Advanced Materials Laboratory, National Institute for Materials Science

A time-dependent two-temperature model is developed to simulate the behavior of an argon radio frequency plasma under transient nonequilibrium conditions, with emphasis to shed light on the temporal and spatial evolution of the nonequilibrium phenomena occurring in pulsed power plasmas. The results show that the effects of changes in input power on the thermal nonequilibrium and the ionization nonequilibrium are most noticeable at the early stages of pulse on and off. The observed deviation from thermal equilibrium during pulsation is more pronounced in the fringes of the plasma and near the wall of the torch. In the central region, the influence is less significant and the plasma remains in a quasilocal thermal equilibrium state. The temporal evolution of the ionization nonequilibrium does not keep pace with that of the thermal nonequilibrium, and the relaxation process of the electron number density is slower and smoother. The effects of operating conditions on the transient behavior of the nonequilibrium situations under pulsed power conditions are also examined. It indicates that, for materials processing, a pulse duration between 2 and 10 ms is adequate for rf plasmas operated in pulse-modulated mode

57)

*J. Am. Chem. Soc.*, **127**(31), 10982-10990 (2005)

**Pyrogenic Iron(III)-Doped $TiO_2$ Nanopowders Synthesized in RF Thermal Plasma: Phase Formation, Defect Structure, Band Gap, and Magnetic Properties**

**X. H. Wang[1], J.-G. Li[1], H. Kamiyama[1,2], M. Katada[3], N. Ohashi[1], Y. Moriyoshi[2] and T. Ishigaki[1]**

[1] Advanced Materials Laboratory, National Institute for Materials Science, [2] Department of Materials Chemistry, Hosei University, [3] Graduate School of Science, Tokyo Metropolitan University

Iron(III)-doped $TiO_2$ nanopowders, with controlled iron to titanium atomic ratios ( RFe/Ti) ranging from nominal 0 to 20%, were synthesized using oxidative pyrolysis of liquid-feed metallorganic precursors in a radiation-frequency (RF) thermal plasma. The valence of iron doped in the $TiO_2$,

phase formation, defect structures, band gaps, and magnetic properties of the resultant nanopowders were systematically investigated using Mo¨ssbauer spectroscopy, XRD, Raman spectroscopy, TEM/HRTEM, UV-vis pectroscopy, and measurements of magnetic properties. The iron doped in $TiO_2$ was trivalent (3+) in a high-spin state as determined by the isomer shift and quadrupole splitting from the Mo¨ssbauer spectra. No other phases except anatase and rutile $TiO_2$ were identified in the resultant nanopowders. Interestingly, thermodynamically metastable anatase predominated in the undoped $TiO_2$ nanopowders, which can be explained from a kinetic point of view based on classical homogeneous nucleation theory. With iron doping, the formation of rutile was strongly promoted because rutile is more tolerant than anatase to the defects such as oxygen vacancies resulting from the substitution of $Fe_3$+ for $Ti_4$+ in $TiO_2$. The concentration of oxygen vacancies reached a maximum at RFe/Ti) 2% above which excessive oxygen vacancies tended to concentrate. As a result of this concentration, an extended defect like crystallographic shear (CS) structure was established. With iron doping, red shift of the absorption edges occurred in addition to the d-d electron transition of iron in the visible light region. The as- prepared iron-doped $TiO_2$ nanopowders were paramagnetic in nature at room temperature.

**58)**

*J. Am. Ceram. Soc.*, **88**(7), 1981-1984 (2005)

**Synthesis and Characterization of Nano-Hetero-Structured Dy Doped $CeO_2$ Solid Electrolytes Using a Combination of Spark Plasma Sintering and Conventional Sintering**

**T. Mori[1], T. Kobayashi[1], Y. Wang[1], J. Drennan[2], T. Nishimura[3], J.-G. Li[3] and H. Kobayashi[4]**

[1]Ecomaterials Center, National Institute for Materials Science, [2]Centre for Microscopy and Microanalysis, The University of Queensland, [3]Advanced Materials Laboratory, National Institute for Materials Science, [4]Faculty of Engineering, Saitama University

Doped ceria ($CeO_2$) compounds are fluorite-type oxides that show oxide ionic conductivity higher than yttria-stabilized zirconia in oxidizing atmosphere. As a consequence of this, considerable interest has been shown in application of these materials for "low" (500°–650°C) temperature operation of solid oxide fuel cells (SOFCs). To improve the conductivity in dysprosium (Dy) doped $CeO_2$, nano-size round shape particles were prepared using a coprecipitation method. The dense sintered bodies with small grain sizes (<300 nm) were fabricated using a combined process of spark plasma sintering (SPS) and conventional sintering (CS). Dy-doped $CeO_2$ sintered body with large grains (1.1 μm) had large micro-domains. The conductivity in the sintered body was low (~3.2 S/cm at 500°C). On the other hand, the conductivity in the specimens obtained by the combined process was considerably improved. The micro-domain size in the grain was minimized using the present process. It is concluded that the enhancement of conductivity in dense specimens produced by the combined process (SPS+CS) is attributable to the microstructural changes within the grains.

**59)**

*J. Am. Ceram. Soc.*, **88**(11), 3232-3234 (2005)

**Synthesis of Anatase-Type $TiO_2$ Nanocrystallites Via a Redox Route**

**J.-G. Li and T. Ishigaki**

Advanced Materials Laboratory, National Institute for Materials Science

Anatase nanocrystallites showing high surface area (~62 $m^2/g$) and good photocatalytic property have been obtained by pyrolyzing at 600°C for 4 h an ammonium titanyl double sulfate precursor ($\alpha$-$(NH_4)_2TiO(SO_4)_2$) synthesized via a redox approach, that is, by oxidizing an aqueous solution of titanium trichloride ($TiCl_3$) with ammonium peroxodisulfate ($(NH_4)_2S_2O_8$), followed by reacting with ammonium sulfate ($(NH_4)_2SO_4$).

60)

*J. Euro. Ceram. Soc.* **26** (4-5), 417-422 (2006)

**Synthesis, characterization and sinterablity of 10 mol% $Sm_2O_3$-doped $CeO_2$ nanopowders via carbonate precipitation**

**Y. Wang[1], T. Mori[1], J.-G. Li[2], Y. Yajima[2] and J. Drennan[3]**

[1]Ecomaterials Center, National Institute for Materials Science, [2]Advanced Materials Laboratory, National Institute for Materials Science, [3]Centre for Microscopy and Microanalysis, The University of Qeensland

A carbonate coprecipitation method has been used for the facile synthesis of highly reactive 10 mol% $Sm_2O_3$-doped $CeO_2$ (20SDC) nanopowders, employing nitrates as the starting salts and ammonium hydrogen carbonate (AHC) as the precipitant. The AHC/$RE^{3+}$ (RE = Ce + Sm) molar ratio (R) and the reaction temperature (T) affect significantly the final yield and precursor properties, including chemical composition and particle morphology. Suitable processing conditions are T = 60 °C and R = 5.0 10, under which precipitation is complete and the resultant precursors show ultrafine particle size, spherical particle shape, and good dispersion. Thus, the processed precursors are rare-earth carbonates with an approximate formula of $Ce_{0.8}Sm_{0.2}(CO_3)_{1.5}\cdot 1.8H_2O$, which directly yield oxide solid-solutions upon thermal decomposition at a low temperature of ~440 °C. The 20SDC solid solution powders calcined at 700 °C show excellent reactivity and have been densified to ~99% of the theoretical via pressureless sintering at a very low temperature of 1200 °C for 4 h.

61)

*J. Euro. Ceram. Soc.* **26** (4-5), 423 428 (2006)

**$TiO_2$ nanopowders via radio-frequency thermal plasma oxidation of organic liquid precursors: Synthesis and characterization**

**J.-G. Li[1], H. Kamiyama[1,2], X.-H. Wang[1], Y. Moriyoshi[2] and T. Ishigaki[1]**

[1]Advanced Materials Laboratory, National Institute for Materials Science, [2]Department of Materials Science, Hosei University,

$TiO_2$ nanopowders have been synthesized via Ar/$O_2$ thermal plasma oxidation of titanium butoxide (TBO) solutions stabilized with diethanolamine (DEA). Experiments were conducted by varying the $O_2$ input in the plasma sheath (10 90 L/min) and the DEA/TBO molar ratio (*R*), while keeping the plasma generation power at 25kW and the reactor pressure at 500 Torr. The resultant powders are mixtures of the anatase and rutile polymorphs in the studied range, whose anatase content and crystallite size exhibit weak dependence on the $O_2$ input at a fixed *R*. Increasing *R* decreases the anatase content, signifying the role of CO gas, generated via oxidation of the organic precursor, on the phase structure. FE-SEM and TEM analysis show that the resultant powders contain majority of nanoparticles (<50 nm) and some large spheres (>100 nm), whose size and/or number tends to decrease at a higher $O_2$ input, leading to gradually increased specific surface area. Raman spectroscopy reveals no significant differences in the crystallite size and oxygen-vacancy concentration of the nanocrystals by varying the $O_2$ input.

62)

*J. Phys. Chem. B*, **110**(3), 1121-1127 (2006)

**Phase Structure and Luminescence Properties of $Eu^{3+}$-Doped $TiO_2$ Nanocrystals Synthesized by Ar/O2 Radio Frequency Thermal Plasma Oxidation of Liquid Precursor Mists**

**J.-G. Li, X.-H. Wang, K. Watanabe and T. Ishigaki**

Advanced Materials Laboratory, National Institute for Materials Science

$Eu^{3+}$-doped $TiO_2$ luminescent nanocrystals have been synthesized in this work via Ar/$O_2$ thermal plasma oxidizing mists of liquid precursors containing titanium tetra-n-butoxide and europium(III) nitrate, with varied $O_2$ input in the plasma sheath (10-90 L/min) and $Eu^{3+}$ addition in the precursor solution (Eu/(Ti + Eu) ) 0-5 atom %). The resultant nanopowders are mixtures of the anatase (30-36 nm) and rutile (64-83 nm) polymorphs in the studied range, but the rutile fraction increases steadily at a higher $Eu^{3+}$ addition, as revealed by X-ray diffraction (XRD) and Raman spectroscopy,

because of the creation of oxygen vacancies in the $TiO_2$ gas clusters by substitutional $Eu^{3+}$ doping. The amount of $Eu^{3+}$ that can be doped into a $TiO_2$ lattice was limited up to 0.5 atom %, above which $Eu_2Ti_2O_7$ pyrochlore was formed in the final products. High resolution transmission electron microscopy (HRTEM) observation indicates that the particles are dense and have sizes ranging from several nanometers up to 180 nm. Efficient nonradiative energy transfer from the $TiO_2$ host to $Eu^{3+}$ ions, which was seldom reported in the wet-chemically derived nanoparticles or thin films of the current system, was confirmed by combined studies of excitation, UV-vis (ultraviolet-visible), and PL (photoluminescence) spectroscopy. As a consequence of this, bright red emissions were observed from the plasma-generated nanopowders either by exciting the $TiO_2$ host with UV light shorter than 405 nm or by directly exciting $Eu^{3+}$ at a wavelength beyond the absorption edge (405 nm) of $TiO_2$.

**63)**

*Thin Solid Films*, in press

**RF plasma processing of Er-doped $TiO_2$ luminescent nanoparticles**

**J.-G. Li[1], X.-H. Wang[1], H. Kamiyama[1], T. Ishigaki[1], T. Sekiguchi[2]**

[1]Advanced Materials Laboratory, National Institute for Materials Science, [2]Nanomaterials Laboratory, National Institute for Materials Science

The synthesis of Er-doped $TiO_2$ nanoparticles is made in this work by $Ar/O_2$ thermal plasma oxidation of a liquid precursor containing titanium butoxide and erbium nitrate, with varying $Er^{3+}$ addition and $O_2$ input. Characterizations of the powders are achieved by chemical analysis, XRD, SEM, TEM, and EDS. The results show that the resultant powders are mixtures of anatase and rutile, whose anatase content increases at a higher $O_2$ input or at a lower $Er^{3+}$ addition. The crystallite sizes of both anatase and rutile tend to decrease at a higher $O_2$ input, but anatase is always much finer than rutile. $Er^{3+}$ cations are hardly dissolved in the $TiO_2$ lattice but mainly formed $Er_2Ti_2O_7$ pyrochlore, which tend to coexist with the rutile-rich larger (>60 nm) particles in the powder. The synthesized particles show good cathodoluminescence at ~1530 nm due to $^4I_{13/2} \rightarrow {}^4I_{15/2}$ transition of the electronic structure of $Er^{3+}$.

**64)**

*Thin Solid Films*, in press

**Growth mechanism for carbon nanotubes in a plasma evaporation process**

**T. Watanabe[1], T. Notoya[1], T. Ishigaki[2], H. Kuwano[3], H. Tanaka[3] and Y. Moriyoshi[3]**

[1]Department of Environmental Chemistry and Engineering, Tokyo Institute of Technology, [2]Advanced Materials Laboratory, National Institute for Materials Science, [3]Department of Materials Chemistry, Hosei University

Carbon nanotubes (CNTs) were synthesized through raw-material evaporation and condensation in RF thermal plasmas to investigate co-condensation process of the vapor mixture of carbon and metals. Addition of 10 wt.%-Ni was the most effective for the CNT synthesis, while Co, Fe, Mo, LaB6 had poor activity. These metal combinations presented synergy effect for the CNT formation. The combinations of Ni–Co, Ni–Fe, and Ni–LaB6 provided more effective activity in the CNT synthesis. Furthermore, the CNT growth mechanism from the vapor mixture of carbon and metals was discussed. Heterogeneous condensation model and carbon–metal molten model were selected as the CNT growth model.

65)

*Thin Solid Films*, in press

**Influence of Ar-$H_2$-$SF_6$ thermal plasma treatment of MCMB powders on the anode properties of a lithium-ion rechargeable battery**

**H. Tanaka[1], M. Kurihara[2], J. -Y. Xu[1], N. Ohashi[1], S. Maruyama[2], Y. Moriyoshi[3] and T. Ishigaki[1]**

[1]Advanced Materials Laboratory, National Institute for Materials Science, [2]Device Development Center, TDK Corp., [3]Department of Materials Science, Hosei University

The surface structure and the anode performance of lithium-ion rechargeable batteries, made with MCMB and Ar-$H_2$-$SF_6$ plasma-treated powders, have been studied under comparative conditions. The treatment process, producing surface modification and the introduction of sulfur and fluorine into the particles by the Ar-$H_2$-$SF_6$ plasma, greatly improved the electrochemical properties of the powder. The lithium-ion rechargeable cell with plasma-treated powder anode had a discharge capacity as much as 13% greater than the untreated powder anode cell, while its irreversible capacity loss (ICL) was as much as 14% less. The intended function of the incorporated sulfur and fluorine, and the surface modification, were their contributions to anode properties improvement.

66)

*Thin Solid Films*, in press

**Fe-doped $TiO_2$ nanopowders by oxidative pyrolysis of organometallic precursors in induction thermal plasma: synthesis and structural characterization**

**X. H. Wang[1], J.-G. Li[1], H. Kamiyama[2] and T. Ishigaki[1]**

[1]Advanced Materials Laboratory, National Institute for Materials Science, [2]Department of Materials Science, Hosei University

Undoped and Fe-doped $TiO_2$ ultrafine powders with dopant concentration ranging from 0.05% up to 20% (Fe/Ti atomic ratio), have been readily fabricated by induction thermal plasma processing through the oxidative pyrolysis of organometallic precursors dissolved in ethanol in an attempt to obtain high-performance photocatalyst. Energy dispersive spectroscopy (EDS) investigation indicates that the Fe/Ti atomic ratios can be kept as in the solution precursors. The synthesized powders consist of spherical particles with mean size of about 40 nanometers. No other phases but anatase and rutile, are identified in the synthesized ultrafine powders. Iron doping remarkably prompts the preference of $TiO_2$ phase formation for rutile to anatase, suggesting that iron ions are prone to be doped in rutile structure. Upon iron doping, the absorption edge shifts to visible light region as indicated by diffuse reflectance UV-vis spectra.

67)

*Thin Solid Films*, in press

**Improved UV Emission of Zinc Oxide through Hyrogen Doping in Pulse-Modulated High-Power ICP**

**T. Ishigaki[1], N. Ohashi[1], H. Taguchi[2], R. Ye[1], H. Haneda[1], and S. Ito[2]**

[1]Advanced Materials Laboratory, National Institute for Materials Science, [2]Department of Pure and Applied Chemistry, Tokyo University of Science

Pulse-modulated high-power inductively coupled plasma (PM-ICP) as a radical source of high flux density was utilized to improve the UV emission efficiency of ZnO. The irradiation of argon-hydrogen PM-ICP plasma gave the improvement of the UV emission at 380 nm. The relationship between the treatment condition and the emission properties was examined with respect to hydrogen dissolution. When treated in the tail plasma flame with adequate cooling, the specimen showed the intense UV emission. The control of heat flux by mixing nitrogen gas to the hydrogen containing plasma also had a favorable influence on the UV emission.

68)

*J. Phys. Chem. B*, in press

**Wavelength-Sensitive Photocatalytic Degradation of Methyl Orange in Aqueous Suspension over Iron(III)-Doped $TiO_2$ Nanopowders under UV and Visible Light Irradiation**

**X. H. Wang[1], J.-G. Li[1],H. Kamiyama[2], Y. Moriyoshi[2],and T. Ishigaki[1]**

[1]Advanced Materials Laboratory, National Institute for Materials Science, [2]Department of Materials Chemistry, Hosei University

Well-crystallized iron(III)-doped $TiO_2$ nanopowders with controlled $Fe^{3+}$ doping concentration and uniform dopant distribution, have been synthesized with plasma oxidative pyrolysis. The photocatalytic reactivity of the synthesized $TiO_2$ nanopowders with a mean particle size of 50–70 nm, was quantified in terms of the degradation rates of methyl orange (MO) in aqueous $TiO_2$ suspension under UV (mainly 365 and 316 nm) and visible light irradiation (mainly 405 and 436 nm). The photodecomposition of MO over $TiO_2$ nanopowders followed a distinct two-stage pseudo-first-order kinetics. Interestingly, the photocatalytic reactivity depends not only on the iron doping concentration, but also on the wavelength of the irradiating light. Under UV irradiation, nominally undoped $TiO_2$ had much higher reactivity than $Fe^{3+}$-doped $TiO_2$, suggesting that $Fe^{3+}$ doping (> 0.05 at%) in $TiO_2$ with a mean particle size of approximately 60 nm was detrimental to the photocatalytic decomposition of methyl orange. Whereas, under visible light irradiation, the $Fe^{3+}$-doped $TiO_2$ with an intermediate iron doping concentration of ~1 at% had the highest photocatalytic reactivity due to the narrowing of band gap so that it could effectively absorb the light with longer wavelength. A strategy for improving the photocatalytic reactivity of $Fe^{3+}$-doped $TiO_2$ used in the visible light region is also proposed.

69)

*Diamond Relat. Mater.*, in press

**Synthesis of c-BN films by using a low-pressure inductively coupled $BF_3$–He–$N_2$–$H_2$ plasma**

**H. Yamamoto[1], S. Matsumoto[1] K. Okada[1], J. Yu[1] and K. Hirakuri[2]**

[1]Advanced Materials Laboratory, National Institute for Materials Science, [2]Faculty of Science and Engineering, Tokyo Denki University

Cubic boron nitride (c-BN) films were synthesized by low-pressure inductively coupled radio-frequency plasma (ICP) chemical vapor deposition (CVD) from a gas mixture of borontrifluoride ($BF_3$), nitrogen, hydrogen and helium. BN films containing 50–80% cubic phase were obtained under 100 mTorr and at 750–1050 °C of substrate temperature. Substrate bias voltage required to obtain c-BN decreased down to – 20 V with increasing substrate temperature. The adhesion was also improved at high substrate temperatures as compared with those obtained in the $B_2H_6$–Ar–$N_2$–$H_2$ gas system, probably because of the decrease of bombarding energy and chemical effects of fluorine for selective deposition of c-BN.

70)

*Thin Solid Films*, in press

**Controlled synthesis of alumina nanoparticles using inductively coupled thermal plasma with enhanced quenching**

**R. Ye, J.-G. Li, and T. Ishigaki**

Advanced Materials Laboratory, National Institute for Materials Science

Synthesis of alumina nanoparticles in an Ar–$O_2$ inductively coupled radio frequency (rf) plasma controlled by axial quench gas injection was investigated. The flow and temperature fields for various quench gas flow rates in the plasma reactor, as well as the corresponding quench rates, were predicted using a renormalization group (RNG) k-ε turbulence model. Nanosize alumina particles were synthesized from the vapor phase by oxidation of aluminum in the plasma. The collected products were characterized by means of field emission scanning electron microscopy (FE-SEM), dynamic light scattering (DLS), and BET surface area analysis. The dependences of particle size and

shape on the injection position and the flow rate of the quench gas were discussed.

71)

*Thin Solid Films*, in press

**Crystallized $TiO_2$ film growth on unheated substrates by pulse-powered magnetron sputtering**

**M. Kamei and T. Ishigaki**

Advanced Materials Laboratory, National Institute for Materials Science

Crystallized $TiO_2$ films were successfully grown in-situ without heating by bipolar-pulse sputtering method at high deposition rates (~40nm/min). The optical emission study of the sputtering plasma during growth revealed that the "pulse geometry" had a great influence on the electron/ion temperature of the plasma. It was revealed that the crystallization and the accompanying enhancement in the photocatalytic activity were not caused by the "temperature effect" but caused by the "plasma effect".

72)

*Appl. Phys. Lett.*, in press

**Discovery of the Deep Level related to Hydrogen in Anatase $TiO_2$**

**T. Miyagi[1,2], M. Kamei[1], T. Mitsuhash[1] and A. Yamazaki[1,2]**

[1]Advanced Materials Laboratory), National Institute for Materials Science [2]Department of Resource and Environmental Engineering, School of Science and Engineering, Waseda University

Deep level transient spectroscopy was carried out to investigate the origin of deep level in the band gap of anatase-$TiO_2$. Epitaxial anatase-$TiO_2$ films were grown on $SrTiO_3$(100) substrate by metal-organic chemical vapor deposition (MOCVD) and reactive pulse magnetron sputtering (PMS). The MOCVD-film had two deep levels located at 0.52 and 0.85 eV below the conduction band. On the other hand, this 0.5eV deep level was not observed in the PMS-film. However, by adding the $CH_4$ or $H_2$ to the sputtering gas, this 0.5eV deep level was observed in the PMS-film. Moreover, the peak of this deep level became definite with an increase in the concentration of additional hydrogen, suggesting that the origin of this deep level was hydrogen.

## 9．2　プロシーディング

1) "Anatase Thin Film with Diverse Epitaxial Relationship Grown on Yittrum", 見矢木崇平, 小川智之, 亀井雅之, 和田芳樹, 三橋武文, 山崎淳司, Proceedings of International Symposium on Material Chemistry in Nuclear Environment, 251-256, (2003).

2) "Surface Modification of Ceramic Materials Induced by Irradiation of High Power Pulsed ICP", 石垣隆正, 岡田展宏, 大橋直樹, 羽田肇, Material Chemistry '02, 137-142, (2003).

3) "Passivation of Defects in ZnO by Hydrogen Plasma Irradiation", 大橋直樹, 石垣隆正, 関口隆史, 坂口勲, 羽田肇, Materials Research Society Symposium Proceedings, 744, M5.3.1-M5.3.6, (2003).

4) "Influence of Pulse-Modulation of High-Power ICP on Hydrogen Doping to Improve UV Emission of ZnO", T. Ishigaki, N. Ohashi, H. Taguchi, and H. Haneda, "Symposium Proceedings, 16h International Symposium on Plasma Chemistry", (Edited by R. d'Agostino, P. Favia, F. Fracassi and E. Palumbo), 2003, Po5.17.1-5.

5) "Effects of Surface Modification on Electrochemical Properties of MCMB Powder Treated in Reactive ICP", H. Tanaka, T. Osawa, Y. Moriyoshi, M. Kurihara, S. Maruyama, T. Ishigaki, "Symposium Proceedings, 16h International Symposium on Plasma Chemistry", (Edited by R. d'Agostino, P. Favia, F. Fracassi and E. Palumbo), 2003, Or12.11.1-6.

6) "Plasma Synthesis of Spherical Titanium Dioxide from Titanium Nitride", S.-M. Oh, D.-W. Park, and T. Ishigaki, "Symposium Proceedings, 16h International Symposium on Plasma Chemistry", (Edited by R. d'Agostino, P. Favia, F. Fracassi and E. Palumbo), 2003, Po11.19.1-6.

7) "Fablication of $MoSi_2$-Based Composite Materials Through Thermal Plasma Processing", 石垣隆正, UNITECR 2003 Congress Proceedings, 441-444 (2003).

8) "TEM Observation of AG Refractory, Japan", 守吉祐介, 田中秀樹, 池本忠, 石垣隆正, 池上隆康, UNITECR 2003 Congress Proceedings, 88-90, (2003).

9) "Diagnostics of Broad-Band Frequency Low Pressure Inductively Coupled Plasma with a Langmuir Probe", 岡田勝行, 小松正二郎, 松本精一郎, Proceedings of SPP-20, 20, 1, 245-246, (2003).

10) "Langmuir Probe Measurements in a Broad-Band Frequency Low Pressure Inductively Coupled Plasma Used for Nanostructured Carbon Deposition", 岡田勝行, 小松正二郎, 松本精一郎, Proceedings of ISAM-2003, 10, 1, 81-82, (2003).

11) "Characteristics of Low Pressure Inductively Coupled VHF Plasma Used for Nanostructured Carbon Deposition", 岡田勝行, 小松正二郎, 松本精一郎, Proceedings of The 7th International Symposium on Sputtering & Plasma Processes (ISSP2003), 7, 1, 124-127, (2003).

12) "Characteristics of Broad-Band Frequency Low Pressure Inductively Coupled Plasma Used for Nanostructured Carbon Deposition", 岡田勝行, 小松正二郎, 松本精一郎, Proceedings of ISPC-16, CD-R, (2003).

13) "プラズマパケット支援レーザーアブレーション法による sp3 結合性 5H-BN の 225nm 室温紫外発光", 小松正二郎, 神田久生, 倉嶋敬次, 桑野弘行, 守吉佑介, 岡田勝行, SPP-20 proceedings, 83-84, (2003).

14) "サブサーフェスの観点から見たレーザー・プラズマ複合化プロセスによる BN 非平衡相の気相成長", 小松正二郎, 倉嶋敬次, 桑野弘行, 守吉佑介, 岡田勝行, SPP-20 proceedings, 43-44, (2003).

15) "Characteristics of Low Pressure Inductively Coupled $CH_4/CO/H_2$ Plasma Used for Nanostructured Carbon Deposition", 岡田勝行, 小松正二郎, 松本精一郎, Proceedings of SPP-21, 1, 1, 124-125, (2004).

16) "Plasma Diagnostics of a Low Pressure Inductively Coupled Plasma Used for Nanocrystalline Diamond Deposition", 岡田勝行, 小松正二郎, 松本精一郎, Proceedings of the International Workshop on Plasma Nanotechnology, 1, 1, P-16-P-16, (2004).

17) "Numerical Simulation of Low Pressure Inductively Coupled Plasma Used for Nanocrystalline Diamond Deposition, 岡田勝行, 小松正二郎, 松本精一郎, Proceedings of Inter. COE Forum Plasma Sci. Technol., 1, 1, 159-160, (2004).

18) "Electron Field Emission from Self-Organized Micro-Emitters of sp3-Bonded 5H Boron Nitride with Exceedingly High Current Density and Low Threshold", 小松正二郎, 奥戸昭雄, 風見大介, デミトリゴルバーグ, Yubao Li, 守吉祐介, 白谷正治, 岡田勝行, Proceedings of SPP-21, 30-31, (2004).

19) "Condensation of sp3-Bonded BN through Highly-Nonequilibrium Fluid State", 小松正二郎, 倉嶋敬次, 清水禎樹, 守吉祐介, 岡田勝行, Proceedings of SPP-21, 320-321, (2004).

20) "Influence of Sulfur and Fluorine Containing Thermal Plasma Treatment of Graphite Powders on the Anode Performance of Lithium-Ion", 石垣隆正, 田中秀樹, 栗原雅人, 大橋直樹, 李継光, 丸山哲, 守吉佑介, Symposium Proceedings, 17th Int. Sympo. on Plasma Chemistry, 1-4, (2005).

21) "Numerical Modeling and Spectroscopic Diagnostics of a Pulse-Modulated Inductively Coupled Plasma", RubinYE, 田口広之, Hubert LANGE, 小林法夫, 伊藤滋, 渡辺隆行, 石垣隆正, Symposium Proceedings, 17th Int. Sympo. on Plasma Chemistry, 1-6, (2005).

22) "RF Thermal Plasma Processing of Visible-Light Responsive Iron- and Nitrogen-Doped $TiO_2$ Photocatalytic Nanocrystals", J.-G. Li, X.H. Wang, H. Kamiyama, N. Ohashi, Y. Moriyoshi, and T. Ishigaki, Symposium Proceedings, 17th Int. Sympo. on Plasma Chemistry", Topic 10, 2005.

23) Growth of Nanostructured Diamond in a Low Pressure InductivelyCoupled Plasma and the Plasma Characteristics, 岡田勝行, 小松正二郎, 石垣隆正, Proceedings of PSS-2005/SPP-22, 1, 1, 153-154, (2005).

24) "Numerical Study on Low Pressure Inductively Coupled Plasma Sources for Nanocrystalline Diamond Deposition", 岡田勝行, 小松正二郎, 石垣隆正, Proceedings of ISSP2005, 1, 1, 137-140, (2005).

25) "Numerical Simulation of Low Pressure Inductively Coupled Plasma Sources for Nanocrystalline Diamond Deposition", 岡田勝行, 小松正二郎, 石垣隆正, Proceedings of ISPC-17, CD-R, 1, 1-5, (2005).

26) "sp3- 結合性 5H-BN 薄膜・自己造形性エミッターによる大気圧ー電界電子放出 ", 小松正二郎, 風見大介, 奥戸昭雄, 田中洋則, 守吉佑介, 知京豊裕, 岡田勝行, Proceedings of PSS-2005/SPP-22, 1, 1, 657-658, (2005).

27) " パルスレーザー支援プラズマ CVD 法による sp3- 結合性 5H-BN 薄膜における電界電子放出エミッターのフラクタル分布 ", 小松正二郎, 風見大介, 奥戸昭雄, 田中洋則, 守吉佑介, 岡田勝行, Proceedings of PSS-2005/SPP-22, 1, 1, 589-590, (2005).

## 9．3　総説、著書

1) "Plasma chemical vapor deposition of nanocrystalline diamond", 岡田勝行, Encyclopedia of Nanoscience and Nanotechnology, **10**(1), 1-12 (2003).

2) " パルス変調高周波誘導プラズマの発生と材料プロセスへの応用 ", 石垣隆正, 大橋直樹, 羽田肇, 作田忠裕, 材料の科学と工学, **40**(2), 2-6 (2003).

3) " 高周波熱プラズマ処理により表面修飾した炭素粒子の電気化学特性 ", 栗原雅人, 丸山哲, 大江一英, 石垣隆正, 電池技術, **15**, 2-10 (2003).

4) " 反応性熱プラズマプロセスによるセラミックス材料の創製 ", 石垣隆正, 大橋直樹, 反応場制御による新しい材料プロセッシング, 北澤宏一監修, 3-33, アイピーシー (2004).

5) " 協奏増幅という切り口 ", 石垣隆正, 目義雄, 伊ヶ崎文和, 反応場制御による新しい材料プロセッシング, 北澤宏一監修, 1-11, アイピーシー (2004).

6) " 低圧高密度プラズマプロセスによるナノクリスタルダイヤモンドコーティング ", 岡田勝行, 石垣隆正, 金属, **75** (3), 201-205 (2005).

7) " プラズマＣＶＤの基礎と応用 ", 岡田勝行, 第 12 回プラズマエレクトロニクスサマースクールテキスト, 1, 1, 92-104, (2005).

8) " 熱プラズマ化学反応場制御によるセラミックス合成 ", 石垣隆正, 表面技術, **57**(1), 18-24 (2006).

## 9．4　特許

登録特許

1) “光触媒効果を利用したリフトオフ法によるパターン形成方法”, 亀井雅之, 三橋武文, 特許 3463246 (2003 年 8 月 22 日 ).

2) “親水化した酸化物固体表面の高速疎水化方法”, 亀井雅之, 三橋武文, 特許 3548794（2004 年 4 月 30 日）

3) “球状酸化チタン粉末の製造法”, 石垣隆正, 渡邊賢司, 李亜利, 片岡英二, 特許 3550660（2004 年 5 月 14 日）

4) “ナノセリア粉末の製造方法”, 池上隆康, 李継光, 森利之, 特許 3586711（2004 年 8 月 20 日）

5) “一般式；ＢＮで示され、六方晶系５Ｈ型ないしは６Ｈ型多形構造を有し、紫外域で発光するｓｐ３結合型窒化ホウ素とその製造方法、及びこれを利用した機能性材料”, 小松正二郎, 岡田勝行, 守吉佑介, 特許 3598381（2004 年 9 月 24 日）

6) “ナノサイズドメイン含有高性能セリア系固体電解質”, 森利之, 王雅蓉, 李継光, 池上隆康, 西村睦, 特許 3619875（2004 年 11 月 26 日）

7) “カラーホイールの形成方法”（台湾）, 亀井雅之, 水橋衛, 三橋武文, 特許 3742366（2005 年 5 月 11 日）

8) “酸化亜鉛紫外発光体の製造方法”, 石垣隆正, 大橋直樹, 羽田　肇, 坂口勲, 関口隆史, 岡田展宏, 特許 3721399（2005 年 9 月 22 日）

9) “カラーホイールの形成方法”, 亀井雅之, 水橋衛, 三橋武文, 特許 3742366（2005 年 11 月 18 日）

特許出願　　38 件

## 9．5　プレス発表等

1) “プラズマ処理によりリチウムイオン電池の充放電効率がアップ　－ 電気化学デバイスの開発に新手法登場 －”（平成 15 年 4 月 22 日）　日刊工業新聞等

2) “二酸化チタン光触媒薄膜を無加熱で作製することに成功 －セルフクリーニング機能を持つ窓ガラス・プラスチックの実現へ向けて－”（平成 16 年 9 月 29 日）　読売新聞等

3) “反応性熱プラズマを利用した表面処理により炭素粉末のリチウムイオン二次電池の性能向上”（平成 18 年 2 月 16 日）　化学工業日報

発　行　日　　平成18年3月31日
独立行政法人物質・材料研究機構

物質研究所研究報告書第12号

「プラズマプロセス酸化物微粒子合成」に関する研究

編集・発行　独立行政法人物質・材料研究機構物質研究所
〒305-0044　　茨城県つくば市並木1-1
電　話　　029-860-4659
ＦＡＸ　　029-860-4701